Integrated Damage Sensing in Fiber-Reinforced Polymer Matrix Composites Using Nano- and Micro-Scale Materials

by

LoriAnne Groo

A dissertation submitted in partial fulfillment
of the requirements for the degree of
Doctor of Philosophy
(Aerospace Engineering)
in the University of Michigan
2021

Doctoral Committee:

Professor Daniel J. Inman, Co-Chair
Professor Henry A. Sodano, Co-Chair
Professor Veera Sundararaghavan
Professor Kon-Well Wang

LoriAnne Groo

lgroo@umich.edu

ORCID iD: 0000-0001-5296-1354

DEDICATION

This dissertation is dedicated to my parents, without whom this would not have been possible.

ACKNOWLEDGEMENTS

I would like to first acknowledge both of my advisors, Professor Dan Inman and Professor Henry Sodano. Their expertise, genuine scientific curiosity, and passion for research have inspired me and strengthened my motivation throughout my doctoral research. I am grateful for their combined efforts which allowed me to pursue my own interests and encouraged me to develop as an independent researcher, while also providing support and advice along the way. Their mentorship, support, and understanding were key in my growth as an engineer. I have been impressed by their continued learning in a variety of disciplines as they push the boundaries of the state-of-the-art. They represent the type of researcher I strive to be. I would also like to thank Professor Veera Sundararaghavan and Professor Kon-Well Wang for their willingness to serve on my committee as well as their generous support and feedback. In addition, I would like to gratefully acknowledge Dr. Mike Philen who took a chance on me at Virginia Tech and helped me find my passion for research.

I would also like to wholeheartedly thank each of my labmates from both Professor Inman and Professor Sodano's research groups. Their friendship and support helped me to maintain perspective and continue having fun throughout my research. In particular, I would like to thank my co-author, Jalal Nasser, whose work ethic, patience, expertise, and friendship played an important role in several experiments and publications. Additionally, I would like to thank my other co-authors, Kelsey Steinke and Lisha Zhang, for their friendship and contributions. I am also grateful for each of the students and postdocs who provided advice and mentorship throughout my PhD. In particular, I would like to acknowledge Dr. Lawren Gamble who was always available to answer questions and give advice with seemingly never-ending patience and a positive attitude. I would also like to acknowledge all of my friends in Michigan for the fun we shared and their constant encouragement.

I do not have the words to express how thankful I am to my parents for their support and unconditional love. They have always helped me to believe in myself and my abilities, and this work truly would not have been possible without them. I would also like to thank my siblings for their encouragement and positivity throughout the duration of my academic pursuits.

Finally, I would like to acknowledge the National Aeronautics and Space Administration (NASA) Space Technology Research Fellowship Program (NSTRF) and the National Science Foundation (NSF) Graduate Research Fellowship Program (GRFP) which provided the primary funding for this research.

TABLE OF CONTENTS

Chapter 3. In-Situ Strain and Damage Sensing Using Piezoresistive Laser Induced Graphene ……………………………………………………………………………………... 56

LIST OF FIGURES

LIST OF TABLES

ABSTRACT

Composite materials have significantly contributed to advances in state-of-the-art aircraft and spacecraft design, resulting in lighter and more flexible structures which have pushed the boundaries of performance and efficiency while maintaining a high standard of safety. However, in-situ sensing of the state of the composite structure (i.e. damage and strain) while in service typically relies on externally bonded sensors and actuators which are limited by size, space, and aerodynamic requirements. To circumvent these issues, more recent attention has turned to embedding sensing components within composite structures during fabrication. However, this increases the probability of failure due to the addition of separate materials within the already damage-susceptible interlaminar region. Consequently, multifunctional composite materials which are capable of efficiently performing the tasks of multiple subsystem components without adding mass or bulk or affecting the structural integrity of the material are needed for high performing engineering structures. Although some progress has been made in the field of multifunctional composite materials, current techniques are either limited to conductive fiber reinforcement or dependent on complex processes that require extreme temperature or chemical environments. Therefore, the use of simple and scalable methods for the development of alternative multifunctional materials with integrated structural health monitoring capabilities for a wider class of fiber reinforcement would overcome multiple barriers facing the field of advanced composite materials.

This work investigates the use of scalable and automatable processes to fabricate self-sensing fiber-reinforced composite materials. The first set of composites investigated are designed such that the structural components possess similar functionality to piezoelectric sensors, thus forming a sensing structural composite. To accomplish this, piezoelectric zinc oxide (ZnO) nanowires are grown directly onto electrically insulating fabric which is then sandwiched between layers of conductive carbon fiber that act as electrodes; thus allowing for electrical measurements to be taken directly from the outer surfaces of the composite. By passively measuring the voltage across the composite, multiple damage modes are detected through voltage emissions which occur as a result of the direct piezoelectric effect. This methodology is further validated using a piezoelectric prepreg formed using dehydrofluorinated polyvinylidene fluoride (DHF PVDF) infused in woven fiberglass which is again sandwiched between conductive carbon fiber layers, thus demonstrating that the investigated principles can be extended to alternative composites containing integrated piezoelectric components.

In addition to piezoelectric materials, this work also considers the integration of piezoresistive functionality within electrically insulating structural composites through the use of laser induced graphene (LIG). The LIG is first directly printed onto woven aramid fabric plies which are then combined to form a piezoresistive composite capable of self-sensing both strain and damage in-situ. Furthermore, a transfer-printing process is developed to integrate LIG within commercial fiberglass prepregs. The resultant fiberglass composites are shown to be capable of detecting both tensile and flexural strain and damage in addition to being able to localize damage both through the thickness as well as in the two-dimensional plane of the composite. Further investigation of the fiberglass composites containing LIG also establishes the ability of electrical resistance measurements to track fatigue damage in the composites. Trends in the resistance measurements are also used to estimate the fatigue life of the samples for the first time in piezoresistive fiberglass-reinforced composites. The result of this work is thus two groups of self-sensing multifunctional composites that are fabricated using simple, scalable processes.

CHAPTER 1

Introduction

1.1. Motivation

Modern engineering structures such as aircraft, spacecraft, automobiles, marine craft, and sporting goods are facing increasingly demanding design requirements for improved efficiency and performance. Frequently these improvements can be achieved by optimizing material and structural design aspects, which has led to the rapidly growing use of composite materials. Typically, composite materials consist of two or more constituents falling within the classes of metals, ceramics, or polymers, and are capable of mechanical performance that exceeds that of homogeneous materials. Specifically, fiber-reinforced composites are most commonly selected for various structural applications due to their high strength-to-weight ratio, effective load transfer capacity, flexibility, corrosion resistance, and tailorability [1]. In particular, the mechanical properties of these composites can be tailored to satisfy particular design or application requirements through the selection of composite constituents, fiber weave, or fiber orientation. While composite materials can vary by choice of fiber length, fiber type, or matrix type, this work primarily focuses on continuous fiber-reinforced polymer matrix composites consisting of continuous glass, carbon, or aramid reinforcing fibers held together using a thermoset polymer matrix. These composites were selected as a result of their extensive current applications and increasing projected use in the aerospace, automotive, and marine industries [2-4].

As a result of the multiphase nature of composite materials, damage in the form of matrix cracking, fiber failure, fiber-matrix debonding, and interlaminar delamination can drastically affect the overall load bearing capacity of the material and lead to catastrophic failure (Figure 1.1). Matrix cracking is typically the first type of damage to occur, as the matrix is comprised of the weaker polymer, the primary role of which is to bind the reinforcing fibers together. This is commonly followed by intralaminar failure in the form of fiber-matrix debonding or interlaminar failure in the form of delamination. As the names imply, fiber-matrix debonding describes the separation between the fiber reinforcement and the binding matrix, while delamination describes the separation between adjacent plies within the composite. Further damage in the form of fiber failure can also result in significant changes to the structural performance of fiber-reinforced composites, as fibers serve as primary reinforcement and support the majority of the in-plane loads.

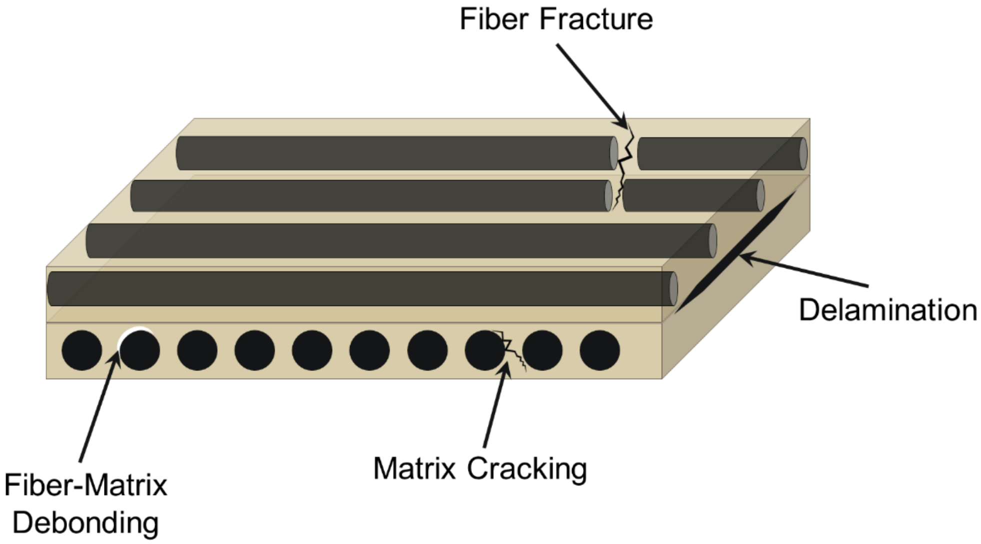

Figure 1.1. Schematic of matrix cracking, fiber-matrix debonding, interply delamination, and fiber fracture occurring in a composite laminate.

Due to the potential for these types of damage to propagate and lead to catastrophic failure, it is critical to detect each form of damage during its early stages in order to preserve the overall safety, integrity, reliability, and performance of the composite structure. To this end, substantial research efforts have been made in the fields of non-destructive evaluation (NDE) and structural health monitoring (SHM) which aim to detect damage or change in structural state (e.g. deformation, temperature, etc.) within fiber-reinforced composites. While NDE typically requires that a structure be temporarily removed from service in order to provide off-line measurements that can be used to deduce information regarding the damage state, SHM differs in that fixed sensors are externally attached to the surface or embedded within the structure in order to provide online information regarding the current condition of the structure by means of active or passive measurements [5, 6].

This chapter summarizes the background of current SHM methods used for the detection of damage in fiber-reinforced composites. Each method can be classified as in-situ, meaning in-place, or ex-situ, which refers to measurements taken retroactively off-site or away from the in-service location. Although a variety of methodologies are reviewed in this section, particular focus is given to in-situ testing methods due to the advantage they offer in being able to detect damage to a structure as it occurs without requiring it to be removed from service. Additional focus is also allocated to the use of embedded sensors and multifunctional materials as alternatives to the more common externally bonded sensors currently used for in-situ monitoring. The following discussion indicates that although significant progress has been made in these areas, the use of externally bonded sensors or the need for complex or expensive fabrication processes for embedded sensing has resulted in a bottleneck between the research detailed in the literature and the application of SHM methods in practice. In this dissertation, damage sensing components are fully integrated within fiber-reinforced composites using scalable and cost-effective processes in an effort to overcome barriers limiting the widespread use of SHM techniques. The resultant multifunctional composites are then subjected to multiple loading configurations, and the damage detection capabilities are compared against commonly used benchmark sensors. These contributions are discussed in further detail at the end of this chapter with particular emphasis on the advancement of the current state-of-the-art in multifunctional composites for in-situ damage detection.

1.2. Overview of Structural Health Monitoring for Composites

Extensive research attention has been given to SHM over multiple decades due to the potential for simultaneously decreasing maintenance costs and increasing structural safety and reliability [7, 8]. Ideally, it is desirable that SHM processes are highly automated and require minimal human intervention or judgement during operation, thus removing subjectivity and human error from damage detection processes. As a result, the need to periodically remove a structure from service and perform a manual inspection is minimized or eliminated, and is instead replaced by an online monitoring system and procedure which outputs objective statistics related to the damage state of the structure under inspection [7]. The most common SHM methods for fiber-reinforced composites typically use externally bonded piezoelectric sensors and transducers for the in-situ monitoring of structural components [8-11]. By definition, piezoelectric materials possess electromechanical coupling which allows them to generate an electric charge when mechanically strained (direct piezoelectric effect), and to deform when an electric charge is applied to them (converse piezoelectric effect) [12, 13]. These two phenomena are illustrated in Figure 1.2a and b, respectively. Using the converse piezoelectric effect, transducers are used to actuate the structure, whereas sensors rely on the direct piezoelectric effect to detect the responding vibrations and provide on-demand information regarding the functioning state of the structure without requiring it to be taken out of service [9-11, 14].

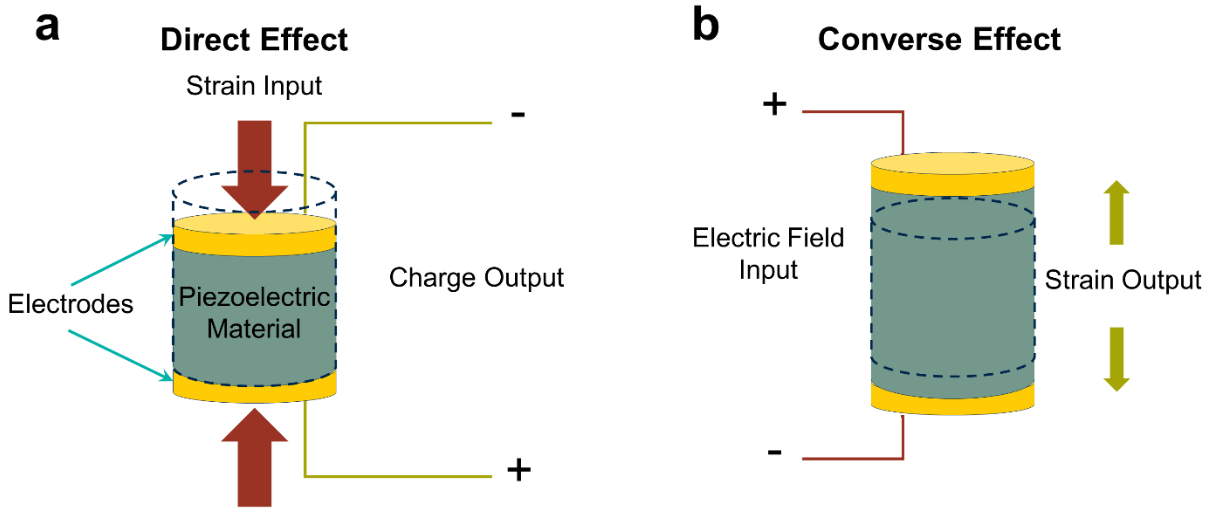

Figure 1.2. (a) Schematic of direct piezoelectric effect. (b) Schematic of converse piezoelectric effect.

Among vibration-based SHM techniques which use active interrogation of the structure, electromechanical impedance-based SHM is a method which has been extensively researched and has been shown to be capable of detecting low-level damage in multiple types of materials [15]. This method uses piezoelectric transducers to apply a high frequency excitation (typically greater than 50 kHz) to the structure and then analyzes the structural response in order to calculate the mechanical impedance. The approach thus relies on the relationship between the electrical and mechanical impedance of a structure, as changes to the mechanical properties of the structure, such as damage, can be correlated to changes in electrical impedance measured using a piezoelectric sensor. However, due to the high frequency of the excitation, the sensing area is limited [15], thus requiring extensive systems of sensors for large or complex structures. While progress in both wireless technology [16, 17] and low-cost, lightweight impedance analysis equipment [18] have enabled some progress to overcome this restriction and improve the feasibility of impedance-based monitoring, the need for large sensor systems is still a major factor limiting the widespread application of this technology for fiber-reinforced composites.

As an alternative method using active interrogation of composite structures, guided Lamb-wave SHM exploits the sensing and actuating potential of piezoelectric sensors to both excite the structure under investigation and sense the resulting elastic waves propagating through the material [9, 19, 20]. Damage is then identified by changes to the wave characteristics such as wave reflection, phase, and transmission velocity which occur as a result of the structural discontinuity caused by the damage [9, 19, 20]. Although this method has improved scalability relative to impedance-based SHM due to the increased distance traveled by Lamb-waves in comparison to the high-frequency waves used for impedance monitoring, the persisting need for large numbers of externally bonded sensors continues to limit widespread application since externally bonded sensors are impractical for high-performing aerodynamic structures due to the potential aerodynamic effects, environmental exposure, and limitations placed on surface complexity (curvature, size, accessibility). Additionally, to detect and localize damage on industrial-scale structures, large, complex systems of sensors along with extensive processing techniques are required in order to separate the changes to the wave characteristics resulting from damage from those that occur as a result of the design of the structure (e.g. discontinuities caused by sharp curvature, edges, or seams). Thus, guided wave SHM requires complicated analysis especially in the case of fiber-reinforced composites with anisotropic properties, and further complications are added in practice as the measurements are subject to environmental noise and operation conditions [20].

Alternatively, acoustic emission testing (AET) has been well-established as an effective damage evaluation method using passive measurements from externally bonded piezoelectric and ultrasonic transducers rather than active interrogation [21-23]. AET is based on the principle that damage to the composite material in the form of debonding, crack initiation, or crack propagation results in a sudden release of energy which leads to propagating elastic stress waves. Commercially available sensors then detect the propagating stress waves at the surface of the material through the direct piezoelectric effect and send an electronic signal to the AET system and software for processing. With pre-determined sensor location or placement, a system or combination of AET measurements can be used to localize the damage by comparing the time of arrival of the propagating wave at different sensors. Although this methodology is relatively accurate and effective for homogeneous materials, this approach requires a knowledge of the wave propagation velocity and attenuation to perform the necessary calculations [24]. In the case of fiber-reinforced composites, the anisotropic nature of the material increases the complexity of this localization method, and thus limits the accuracy of damage location prediction in these materials when adopting the time-of-arrival approach [25-27]. Additionally, for wave attenuation and wave time-of-arrival comparisons, the described sensors require a certain orientation or proximity relative to the damage source [24, 28]. Furthermore, localization is achieved using complex networks of sensors that are externally bonded, which again results in limited applications for reasons already discussed. It should also be noted that traditional AET sensors typically use lead zirconate titanate (PZT) as the piezoelectric sensing element, however PZT wafers are inherently stiff and brittle due to the ceramic nature of the material which inhibits effective bonding of PZT wafers to curved or flexible structures. To overcome some of these challenges and aid the realization of AET for in-service composite structures, a variety of research has focused on alternative sensors to traditional ceramic wafers for AET with particular application in fiber-reinforced composites. For example, several groups have demonstrated the effectiveness of surface-bonded polyvinyledene fluoride (PVDF) sensors [29, 30] and active fiber composites (AFCs) [31, 32] in AET. These alternative sensors were shown to be capable of detecting the same damage as commercially available PZT piezoelectric sensors without the same rigidity and brittleness, however the sensors still required external bonding to the structure under inspection.

Although current SHM methods which employ externally bonded sensors can be useful in detecting and localizing damage in certain materials and structural applications, as previously stated, the practical application of such methods is inherently limited by the need to permanently attach the sensors to the outer surface of the structure. Thus, in an effort to more fully overcome limitations placed by external bonding, embedded sensors have been utilized in multiple SHM applications. The sensors used include, but are not limited to, PZT wafers, AFCs or macro-fiber composites (MFCs), optical fibers, and PVDF film sensors [30, 33-38]. Among these embedded sensors, fiber optic sensors have been widely studied since they can be embedded directly into the fiber-reinforced composite material during fabrication, and can sense strain as well as damage [39-42]. The fiber sensors are able to correlate changes in optical properties, such as intensity, wavelength, or phase to damage or change in structural state [39]. In addition, fiber Bragg grating (FBG) sensors can also be used for ultrasonic AET [33, 43-45]; however, embedding optical fibers within the fiber-reinforced composite has been shown to negatively affect the structural integrity of the composite material, as it introduces defects due to the difference in fiber diameter between the optical fiber and the structurally reinforcing fiber [46, 47].

Due to its flexibility and conformability when attached to the surface of materials and its less invasive presence when embedded within materials, PVDF in the form of film sensors has also received considerable interest for AET sensing [30, 34, 35]. Notably, the fully embedded PVDF sensors in the referenced works were each able to detect damage with capabilities similar to their externally bonded counterparts, however, the nature of these sensors required predetermined positioning and discrete placement in the structure during the manufacturing process. This adds a degree of complexity to the manufacturing process of the composite materials and limits the sensing area by requiring discrete and fixed placement of the sensors. Additionally, similar to external sensors, large systems of sensors or sensor networks are needed to monitor large, complex structures such as aircraft components. The embedded sensors also provided no inherent structural benefit to the composite material, and instead potentially increased the risk of debonding and delamination due to the interruption in the interlaminar region of the composite resulting from the inclusion of fluorinated films which exhibit low surface energy for bonding. Thus, SHM research using externally bonded or discretely embedded sensors up to this point has not yet led to an economical, fully-distributed sensing approach with inherent structural advantages.

1.3. Multifunctional Materials

To meet the demands for lighter, more aerodynamic structures and overcome the previously discussed limitations of external or discretely embedded sensors, recent research has investigated the use of multifunctional materials which perform the functions of multiple systems (i.e. damage sensing, energy harvesting, energy storage) using a structural material. The most common application of multifunctional materials for damage detection purposes is the use of electrical resistance measurements for strain and damage sensing in carbon fiber-based composites [48, 49]. Initially, resistance-based damage and strain sensing was employed exclusively with conductive carbon fiber reinforcement, as it was intended to take advantage of the inherent piezoresistivity of the fibers. Piezoresistivity is a material property that is manifested by a change in electrical resistance with respect to the strain; it should be noted that this is distinctly different from the piezoelectric effect which exhibits a change in electric potential. The piezoresistivity of carbon fiber enables their respective composites to show a change in electrical resistance corresponding to a change in strain, which can be tracked through a simple in-situ resistance measurements [48, 49]. Using the common four-probe measurement technique, current is applied through the composite material subjected to loading, and the corresponding voltage is measured which allows for the calculation of the electrical resistance using Ohm’s law. Initially, as the sample is strained, the measured electrical resistance increases approximately linearly (Figure 1.2b). Then, as damage occurs, such as in the form of fiber fracture, sudden increases in the electrical resistance of the composite samples can be observed due to the sudden breaking of conductive pathways (Figure 1.2c).

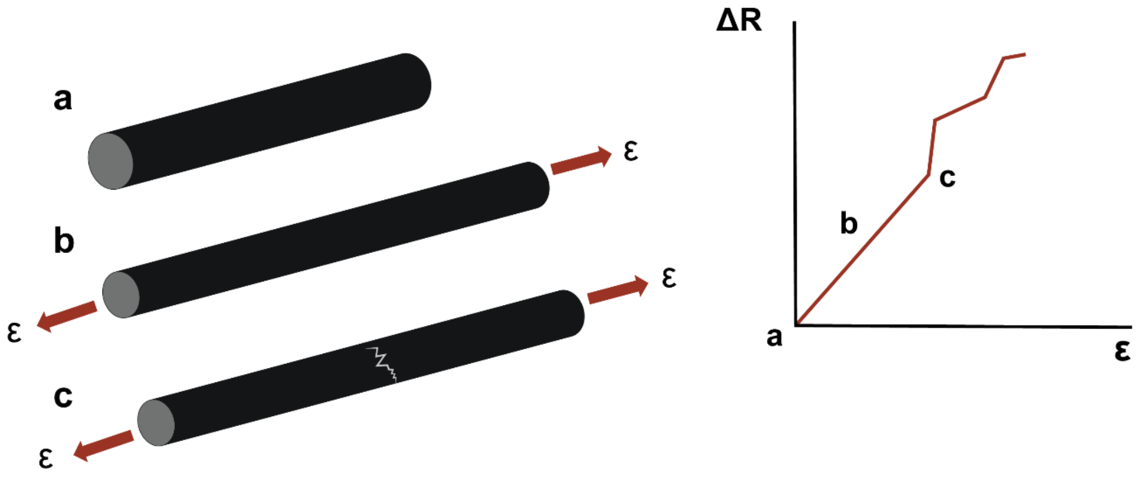

Figure 1.3. Schematic of resistance-based monitoring using carbon fiber. (a) Original position of a single carbon fiber and corresponding resistance. (b) Linearly increasing resistance with increasing strain. (c) Sudden increases in resistance corresponding to fiber fracture.

This methodology has been utilized to detect various forms of strain and damage in carbon fiber-reinforced composites including fiber fracture during tensile loading, tensile strain, impact damage, and flexural strain and damage [48-54]. Resistance-based SHM has also been expanded to provide additional information regarding the damage state of the structure. For example, by taking multiple measurements at various locations on the composite, relative changes in conductivity can be used to locate the damage [55-57]. Additionally, further work has also utilized trends in in-situ resistance measurements from carbon fiber composites during fatigue loading to enable progressive damage tracking and fatigue life prediction [58]. However, the methods used in each of these works are limited to conductive fiber reinforcement; therefore, alternative solutions have been developed to extend the application of resistance-based damage and strain sensing to insulating fiber reinforcement by adding conductive fillers [59-61]. Rather than relying on the piezoresistance of the reinforcing fibers, these methods aim to detect damage to traditionally electrically insulating composites by monitoring changes to the conductive pathways between conductive fillers due to separation during matrix cracking, debonding, delamination, or fiber cracking, thus leading to changes in the overall electrical resistance of the composite.

1.3.1. Carbon Nanotubes

Among conductive fillers used for resistance measurements, carbon nanotubes (CNTs) (Figure 1.4) are of particular interest for several reasons; the introduction of CNTs onto the surface of reinforcing fibers or dispersed in the supporting matrix have been shown to increase the mechanical properties of host composites, such as damping coefficient and interfacial shear strength, and the conductive CNTs add piezoresistivity to composites with traditionally insulating fibers (i.e. glass and aramid fibers) [62-66]. For example, Gao et al. demonstrated the utility of the piezoresistivity by dispersing CNTs throughout the epoxy matrix and making in-situ measurements while the composites were subject to impact damage [67]. In addition, multiple other efforts have also studied the effectiveness of dispersing CNTs in the matrix of fiberglass composites in order to track fatigue loading via electrical resistance measurements [68, 69]. In an alternative effort to avoid dispersing CNTs in the matrix, Alexopoulos et al. demonstrated the usefulness of CNTs in the form of a fiber for tracking both tensile and flexural loading and damage in fiberglass composites [60]. The CNT fiber was embedded in the composite during the fabrication process, but the sensing area was limited to the physical location of the fiber as the sensing material was not fully distributed throughout the composite. Further research has also established that relative changes in conductivity can be used to locate the damage in composites containing piezoresistive CNTs by taking multiple measurements at various locations on the composite and using either the electrical potential method or electrical impedance tomography (EIT) [55-57, 70, 71]. The electrical potential method relies on local changes in electrical resistance while EIT is more complex in execution and is used to reconstruct the local conductivity of the specimen under investigation and more precisely locate the points of conductivity change [72]. For example, Gallo et al. used both the normalized resistance change approach and EIT to locate damage in two-dimensions in a fiberglass plate with embedded CNTs and provides a comparison between the two methods [70].

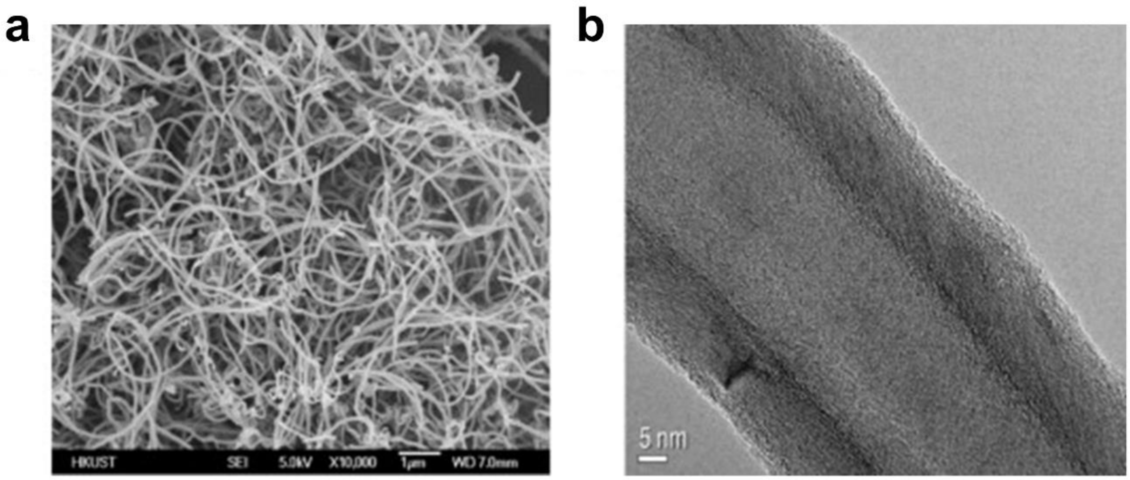

Figure 1.4. (a) Scanning electron microscope (SEM) and (b) transmission electron microscope (TEM) images of multiwall CNTs [62].

However, the improvement in mechanical properties as well as accurate and reliable in-situ damage detection and localization in fiber-reinforced composites containing CNTs is heavily dependent on the distribution of the nanotubes and the formation of percolating networks, with the suggested distance between nanotubes being less than approximately one nanometer for damage detection [61, 73, 74]. It follows that in order to achieve the required minimum separation, careful synthesis and manufacturing techniques are necessary to prevent entangling or aggregation of the nanotubes. This is a challenging task given that CNTs cause a considerable increase in the uncured resin viscosity due to their tendency to form agglomerations as a result of van der Waals forces [75-77]. In contrast, methods used to deposit CNTs directly onto the surface of the reinforcing fibers also face limitations such as the high temperatures and harsh chemical environments necessary for chemical vapor deposition (CVD), whereas other benign methods such as electrophoretic deposition (EPD) require electrically conductive fibers [78-80]. Thus, the complexity of fabrication techniques necessary to introduce CNTs lead to concerns regarding the scalability and widespread application of these methods and techniques [61, 81, 82]. Thus, a scalable, low-cost, and automatable alternative is desired for increased use of piezoresistive multifunctional materials for SHM and damage localization in fiber-reinforced composites, particularly for large-scale industrial components.

1.3.2. Zinc Oxide Nanowires

Among multifunctional materials, zinc oxide (ZnO) nanowires have recently gained attention due to their inherent piezoelectric and semiconducting properties as well as their contributions to the mechanical properties of the host composite [83]. To integrate ZnO nanowires within fiber-reinforced composites, they can simply be grown directly onto woven or unidirectional fabric which is then used as a preform for composite fabrication using conventional manufacturing techniques. When included in this way, the nanowires form a functional interphase between the fiber and matrix. Multiple researchers have shown this tailorable fiber-matrix interphase results in increased tensile strength and modulus, increased interlaminar shear strength, and improved damping characteristics beyond those achieved using dispersed carbon nanotubes [84-87]. In addition to their appealing structural benefits, the piezoelectric and semiconducting properties of ZnO nanowires also enable the embedding of actuation and sensing functionalities in composite materials. Prior work has utilized the piezoelectric coupling of the nanowires in energy harvesting by scavenging small amounts of power from ambient structural vibrations using either flexible nanogenerators or fiber-reinforced composites containing arrays of ZnO nanowires as shown in Figure 1.5 [88-91]. Additional work has also studied their use in a variety of sensing applications including humidity sensing [92], chemical sensing [93, 94], and mechanical stress sensing [95]. However, although prior work has successfully implemented structural and non-structural functionalities of multifunctional composites containing ZnO, the potential of the functional nanowire interphase for integrated in-situ damage detection in fiber-reinforced composites remains unexplored.

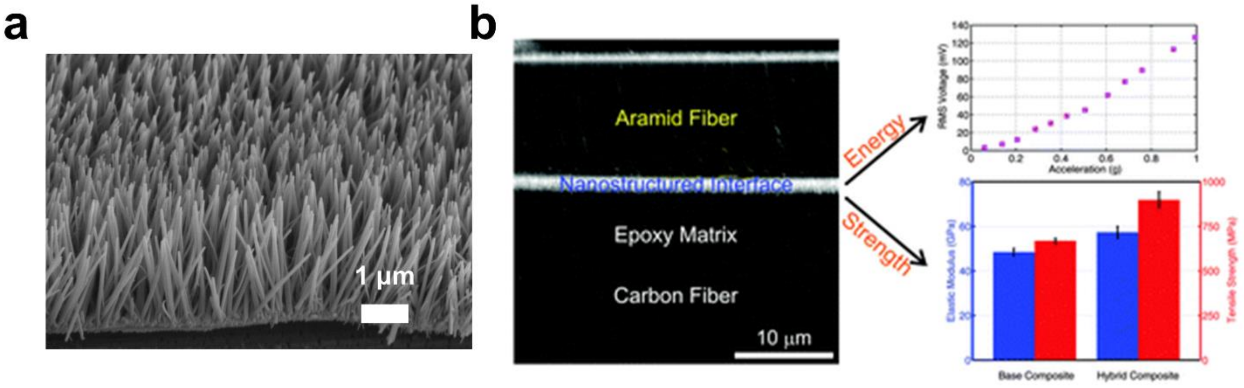

Figure 1.5. (a) SEM image of ZnO nanowires on Spectra. (b)Use of ZnO nanowires for energy harvesting and strength improvement in hybrid aramid and carbon fiber composites [88].

1.3.3. Polyvinylidene Fluoride

PVDF is an appealing piezoelectric material as it possesses the flexibility of a polymer in addition to strong piezoelectric coupling, and, as such, is easily conformable for various sensing and actuating applications [96-100]. PVDF crystallizes in three different phases, the amorphous α-phase, the partial polarity γ-phase, and the polar β-phase [101-103]. For piezoelectric applications, the β-phase is the most desirable phase as it results in the highest piezoelectric, ferroelectric, and pyroelectric properties [102-104]. For this reason, increasing the fraction of β-phase in PVDF has been a topic of interest over many years. Among the methods investigated, uniaxial drawing is the most commonly used to mechanically align the polymer chains in a parallel orientation and form planar conformation, or β-phase [105-107]. However, since drawn PVDF relies on the physical shape of the polymer, thermal relaxation occurs at elevated temperatures above the Curie temperature of the PVDF, resulting in a return to the energy-preferential amorphous α-phase, thus reducing or eliminating the piezoelectric response [108, 109]. In contrast to mechanically drawn PVDF, dehydrofluorinated (DHF) PVDF produces the energy-preferential formation of a thermally stable β-phase [110]. The dehydrofluorination process is referred to as the chemical reaction that takes place when PVDF is exposed to a basic environment, resulting in a loss of the hydrogen fluoride (HF) molecule, and leading to carbon-carbon double bonds in the backbone of the PVDF. The extent of dehydrofluorination can thus be controlled by adjusting the basicity of the environment and the exposure duration in order to achieve preferential levels of β-phase. Since the induced β-phase is the product of a chemical adjustment to traditional PVDF, it exhibits thermal stability up to ~200 °C which is notably superior to drawn PVDF [110]. The dehydrofluorination process thus enables integration of the DHF PVDF polymer within structural composites during the fabrication process since the β-phase exhibits thermal stability. As a result, the need for discrete embedded or externally attached sensors can be eliminated and replaced with a fully distributed piezoelectric matrix within the composite, however, this capability is yet to be explored and has not been applied to damage detection in fiber-reinforced composites.

1.3.4. Laser Induced Graphene

Recently, Lin et al. reported the development of a new class of carbon-based nanomaterials that can be directly generated from the surface of commercial polymer materials using a CO_2 infrared laser [111]. Termed as laser induced graphene (LIG), this porous graphitic nanomaterial is a promising alternative to the more commonly used CNT-based strain sensors due to the simplicity of the methodology, the lack of necessary chemical modifications and pre-processing, and the design flexibility [111]. The simple LIG fabrication process relies on a CO_2 infrared laser operating in raster mode in ambient environmental conditions to carbonize polymer substrates by converting sp^3-carbon atoms to sp^2-carbon atoms, thus generating a porous graphitic surface with piezoresistive properties. Typically, polyimide is used as the precursor for the graphitic surface, and no external graphene source is required, resulting in a simple, scalable, and automatable process. Since its initial discovery, the piezoresistive behavior of LIG has been investigated for several applications including biomedical applications [112, 113], composite strain sensing [114, 115], and flexible strain sensors [116, 117]. For example, Luo et al. fabricated LIG strain gauges on polyimide films which were then glued to the surface of fiberglass-reinforced composites and used to sense deformation of the host composite [115]. Additionally, Rahimi et al. studied the use of highly flexible LIG-based strain sensors for sensing active motion of human subjects [116]. The LIG surfaces were transferred to polydimethylsiloxane (PDMS) which was then attached to a glove and shown to be capable of tracking strain effectively enough to determine the hand and finger position of the wearer (Figure 1.5) [116].

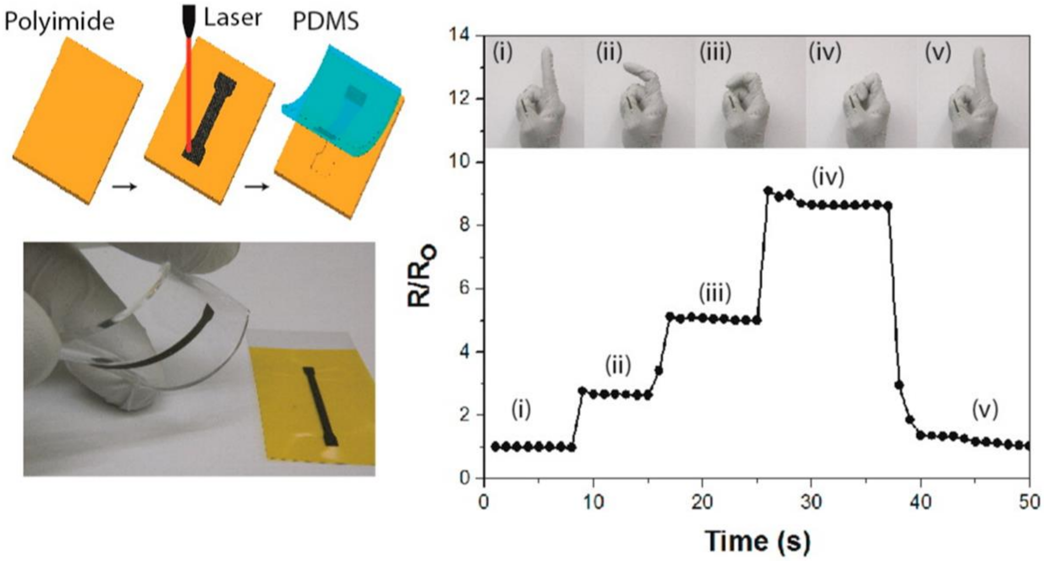

Figure 1.6. LIG embedded in PDMS and used to track the motion of a human finger [116].

Although the LIG was shown to be sensitive to mechanical strain in these and other applications, the LIG-based sensors still require external bonding to the structure of interest. This remains an issue due to the strict requirements it places on the state of the surface such as its roughness, curvature, and compatibility with adhesive materials. In addition, these externally bonded sensors suffer limitations resulting from environmental exposure and parasitic aerodynamic effects. As an alternative method, Wang et al. generated a free-standing LIG-based buckypaper which was then embedded between fiberglass prepreg layers and used to monitor composite cure and strain [114]. However, the mechanical properties of the buckypaper-prepreg composite were not investigated, and the gauge factor of the resultant composite was not reported. Therefore, an alternative method which removes the need for external bonding and allows for tailorable placement, size, and sensing capabilities all while maintaining the properties of the composite material is still needed. Furthermore, although it has been demonstrated that LIG can be added to the surface of aramid [118, 119], no research reported in the literature to this point has evaluated the use of directly-printed piezoresistive LIG for the self-sensing of strain in aramid fiber-reinforced composites.

1.4. Overview of Contributions

The work presented in this dissertation focuses on advancing the state-of-the-art in multifunctional fiber-reinforced composite materials for the in-situ self-sensing of damage using fully integrated sensing materials. Additional emphasis is also placed on investigating scalable processes with potential for large-scale industrial application. It should be noted that the primary motive is to investigate the sensing and damage detection potential of the composites rather than their structural characteristics; however, in the cases where novel processes or materials yielded new composite materials whose properties have not previously been characterized, some structural testing was completed to ensure the mechanical properties of the composites were largely maintained. A description of the contributions from each chapter are detailed below.

1.4.1. Use of Self-Sensing Piezoelectric Composites for Damage Detection

The work discussed in Chapter 2 utilizes functional structural composites for self-sensing damage in-situ using multiple materials, the first of which is a ZnO nanowire interphase similar to that discussed in Section 1.3.2. To accomplish this, the nanowires are integrated into fiber-reinforced composites by directly growing them onto an electrically insulating fabric which also serves as a reinforcing layer. The insulating fabric with ZnO nanowires is then sandwiched between conductive carbon fabric layers which function as distributed electrodes as well as additional reinforcing layers. The resulting hybrid composites thus possess structural components that mimic the functionalities of the constituents of a traditional piezoelectric sensor. The final composites are then subjected to mechanical testing during which the voltage across the composite is passively measured for emissions corresponding to damage. Once damage occurs, the piezoelectric ZnO nanowire interphase undergoes a rapid change in strain resulting in a charge separation, as a result of the direct piezoelectric effect, that is measured as a sudden voltage emission across the composite.

This methodology is further validated by fabricating composites using a piezoelectric prepreg comprised of woven fiberglass with a DHF PVDF matrix. The insulating piezoelectric prepreg is then once again sandwiched between conductive electrodes of woven carbon fabric. As before, the resultant hybrid composite possesses a similar functional make-up to a piezoelectric sensor, and is shown to again be capable of detecting damage in-situ via voltage emissions. Additionally, further analysis of the voltage emission signals measured from both sets of samples, ZnO and PVDF, results in statistical damage metrics which can be used to track the damage progression and predict the onset of catastrophic failure. In comparison to alternative in-situ damage detection techniques such as AET or electrical resistance measurements, this method carries the added benefit of a completely distributed sensing material and conductive electrodes covering the entirety of the composite sample, as well as the elimination of any reliance on initial measurements or input current. The resulting functional composites are thus ideally suited for self-sensing minor damage over a large area or in complicated structural components without requiring external sensors or large networks of discrete sensors.

1.4.2. In-Situ Strain and Damage Sensing Using Integrated Laser Induced Graphene

The work presented in Chapter 3 applies the resistance-based SHM methodology discussed in Section 1.3 using piezoresistive LIG integrated within aramid- and fiberglass-reinforced composites. Multiple configurations are investigated for both strain and damage sensing including: continuous LIG interlayers in aramid-based composites, continuous LIG interlayers in fiberglass-reinforced composites, and tailorable LIG-based serpentine strain gauges in fiberglass-reinforced composites. While the LIG is directly written onto aramid fabrics, a transfer printing process is utilized for embedding LIG within fiberglass prepreg composites. In each case, the sensing component is entirely integrated within the final composite material, therefore reducing weight and eliminating the limitations due to external bonding or complex fabrication techniques. Additionally, the simple printing process used here also allows for the customization of the size and sensing requirements for various applications. In this chapter, the LIG is shown to be capable of tracking monotonic cyclic strain as well as dynamic motion, and is also proven to be capable of detecting damage under tensile and flexural loading conditions in both aramid and fiberglass composites. Thus, a simple, scalable, and effective methodology is used to introduce piezoresistive properties to traditionally electrically insulating composites.

1.4.3. Damage Localization in Composites Using Integrated Laser Induced Graphene

In Chapter 4, LIG is again transfer printed onto commercial fiberglass prepreg to fully integrate self-sensing functionality into fiberglass-reinforced composites. The piezoresistive response is then subsequently used to localize damage in the two-dimensional plane and through the thickness of the resultant composites using multiple local resistance measurements. A combination of in-situ and ex-situ measurements are used to accomplish this objective: First, in-situ resistance measurements are used to determine the relative location of damage in one-dimension under tensile loading. Subsequently, separate in-situ measurements are used to locate damage through the thickness of the composite under flexural loading. Finally, ex-situ methods are used to calculate the two-dimensional location of a hole in a plate. Therefore, the work in this chapter presents a self-sensing structural composite material with potential for three-dimensional damage localization capability using widely available materials and technology.

1.4.4. Fatigue Life Prediction of Composites with Integrated Laser Induced Graphene

In Chapter 5, the fiberglass composites containing continuous LIG interlayers are subjected to tension-tension fatigue loading while monitoring changes in the electrical resistance of the composite. In addition to tracking damage progression throughout mechanical loading, the characteristics of the resistance measurements including the peak-to-peak resistance measurements and the first derivative of the percent change in resistance with respect to the number of cycles are also used in a predictive model to anticipate the fatigue life of the composites. By analyzing the percent change in the peak-to-peak value of the resistance measurements during the first 20 – 50% of the fatigue life, the rate of increase in the peak-to-peak value is found to correlate to the number of fatigue cycles. As the test progresses beyond ~70%, the first derivative of the percent change in resistance is then used to more accurately predict failure using an exponential model. Good correlation between the estimated fatigue life and the actual fatigue life is seen across each sample regardless of initial resistance, applied stress, or fatigue life indicating that the LIG is capable of life cycle prediction in composite structures subjected to unpredictable dynamic loading environments.

1.4.5. Conclusions and Future Work

The final chapter of this dissertation will summarize the key findings and contributions of this work to the field of self-sensing multifunctional fiber-reinforced composite materials. Particular emphasis is given to the results using fully distributed and fully integrated sensing materials that do not detrimentally affect the structural properties of the composite. Additionally, some suggestions for future research areas building on the findings from this dissertation are presented to further expand the principles discussed and increase the probability for widespread application of multifunctional materials for SHM purposes.

CHAPTER 2

In-Situ Damage Detection Using Integrated Piezoelectric Materials

2.1. Chapter Introduction

This chapter presents two fully integrated piezoelectric materials for the self-sensing of damage in fiber-reinforced composites where the structural material itself acts as a structural health monitoring system. Current in-situ damage detection of fiber-reinforced composites typically uses methods which require external sensors, precise initial measurements for each component under evaluation, or electric current input to the structure. To overcome these limitations, this work utilizes a multifunctional interphase of piezoelectric zinc oxide (ZnO) nanowires which are integrated and a piezoelectric prepreg fabricated using dehydrofluorinated (DHF) polyvinylidene fluoride (PVDF), both of which are integrated into fiber-reinforced composites to provide the ability to sense damage in-situ. The fully distributed sensing materials prove capable of detecting multiple damage modes using passive voltage measurements as demonstrated during various loading configurations. The voltage emissions corresponding to damage are also analyzed to provide signal characteristics corresponding to the damage state of the specimen to indicate damage progression and the approach of catastrophic failure. The result of this work is thus the creation of two multifunctional structural materials with damage detection capabilities. It can be noted that the principles investigated in this work can also be extended to alternative structural composites containing integrated piezoelectric materials in the form of nanoparticles, nanowires, or films.

2.2. Sample Preparation and Composite Layup

Both composite sets evaluated in this chapter are fabricated such that the structural components mimic the functional structures of a piezoelectric sensor, specifically, an electrically insulating piezoelectric material sandwiched between two conductive electrodes. The fabrication process for each composite set, both that containing ZnO nanowires and that with DHF PVDF, is described in detail in the following section.

2.2.1. Zinc Oxide Nanowire Fabrication

2.2.1.1. Aramid Fabric Preparation

Plain weave aramid fabric (Kevlar® KM2+, style 790, CS-800, 4.3 oz/yd^2, received from BGF Industries) was selected as the ZnO nanowire growth substrate as well as the insulating layer in the first hybrid composite to be discussed. The fabric was initially prepared using cleaning and functionalization processes initially outlined by Ehlert and Sodano to improve the nanowire adhesion to the fabric [120]. First, the fabric was cleaned using subsequent washes of boiling acetone and boiling ethanol, after which it was dried under vacuum at 100 °C for one hour. The cleaning process simply acted to remove any organic contaminants on the surface of the fabric. Following cleaning, the fabric was functionalized using a 10 wt% aqueous solution of sodium hydroxide (Fisher Chemical, Certified ACS Pellets) at room temperature. The fabric was soaked in the solution for 20 minutes after which it was rinsed thoroughly with deionized (DI) water and dried under vacuum at 100 °C for one hour. The functionalization was then followed by an ion exchange using 33 vol% hydrochloric acid (HCl) (Fisher Chemical, Certified ACS) where the fabric was briefly dipped in the acid after which it was again thoroughly rinsed with DI water and dried following the same procedure.

2.2.1.2. Zinc Oxide Growth

A colloidal suspension method first outlined by Wong et al. [121] was used to deposit an initial seeding layer of ZnO nanoparticles onto the surface of the aramid fabric. To prepare the nanoparticle solution, 0.0125 M concentrate of zinc acetate dihydrate (Sigma-Aldrich, > 99%) and 0.02 M concentrate of sodium hydroxide were dissolved separately in ethanol at 50 °C and 60 °C respectively under vigorous stirring. Once the powders had been fully dissolved, 32 mL of the zinc acetate mixture was diluted with 256 mL ethanol, and 32 mL of the sodium hydroxide mixture was diluted with 80 mL of ethanol. Each solution was then heated separately to 55 °C, after which the sodium hydroxide/ethanol solution was added dropwise to the zinc acetate dihydrate/ethanol solution. The combined solution was allowed to mix at 55 °C for 45 minutes, after which the nanoparticle growth was quenched using an ice bath.

Prior to the nanowire growth, the previously prepared aramid fabric was dipped in the nanoparticle solution to deposit a seeding layer onto the surface of the fabric. After dipping in the colloidal suspension of nanoparticles, the seeding layer was annealed at 150 °C for 10 minutes and subsequently cooled for 10 minutes. This seeding, annealing, cooling procedure was completed three times to ensure a uniform layer of nanoparticles fully covered the surface of the fabric. The fabric with ZnO nanoparticles was then submerged in a solution containing 0.075 M zinc nitrate hexahydrate (Sigma-Aldrich, > 99%) and 0.075 M hexamethylenetetramine (Sigma-Aldrich, > 99%) in DI water and the fabric and solution were placed in a convection oven at 80 °C for eight hours for nanowire growth. Following the growth, the fabric was rinsed thoroughly in DI water and dried in the same convection oven for one hour. The resulting nanowire array conformally covered the entire surface of the aramid fabric as can be seen in the scanning electron microscope (SEM) images in Figure 2.1a which were taken using a JEOL JSM-7800FLV field-emission SEM.

2.2.1.3. Composite Layup and Sample Preparation

Functional hybrid composites were fabricated using the aramid fabric with ZnO nanowires combined with plain weave carbon fabric (Hexcel® HexForce™ Style SGP196-P, 5.80 oz/yd2) which acted as both structural reinforcement as well as electrodes. In the case of the three-point bend composites, two inner layers of aramid fabric were used with one carbon fabric layer on both top and bottom, however, the tensile specimens contained only one layer of aramid fabric between the carbon fabric layers. This was done to increase the thickness of the flexure samples for practicality of testing. For reference, a schematic of the stacking sequence is shown in Figure 2.1b. The inner surfaces of the carbon fabric layers in contact with the ZnO nanowire interface were sputtered with gold to form a metal-semiconductor junction in order to create a Schottky barrier for improved sensing and actuation performance of the ZnO nanowire arrays [88, 122]. A commercially available epoxy comprised of Epon 862 resin combined with curing agent Epikure 3230 (both received from Hexion) at a weight ratio of 100:35 was used as the composite matrix. The epoxy was distributed throughout each fabric layer using the vacuum assisted resin transfer molding (VARTM) method and cured following a curing cycle of 10 hours at room temperature, followed by two hours at 80 °C, and a 125 °C post-cure for three hours all under 100 psi (689.5 kPa) compression. Individual three-point bend samples were cut from the completed composite to meet ASTM D7264 standard sizes for composite testing, however, additional length was added to the specimens than is recommended for traditional three-point bend testing. This was done to ensure adequate space for the attachment of wire leads for voltage measurements. The completed three-point bend test specimens were 0.8 mm in thickness, 13 mm wide, and approximately 100 mm long and were tested at a span ratio of 40:1. The tensile specimens were cut to dimensions of 100 mm in length and 10 mm in width per ASTM D3039 standards. After the samples were cut, the edges of both the tensile and three-point bend samples were polished to expose the insulating layer of aramid fabric and eliminate electrical shorting between the top and bottom carbon fiber electrodes. A schematic of the cut and polished composite sample is shown in Figure 2.1c. Fiberglass tabs prepared using the same commercial epoxy matrix and VARTM technique were attached to the tensile samples using Loctite EA 9430 two-part adhesive and in coordination with ASTM D3039 standards. The outermost insulating epoxy layer was then removed from a portion of each three-point bend and tensile sample to expose the carbon fabric in a small area of both the top and bottom surfaces, after which 33-gauge copper wires were then attached to the exposed area using a combination of epoxy and silver paint for voltage measurements during testing. Baseline samples were prepared following the same methodology, however untreated aramid fabric without ZnO was used as the insulating layer.

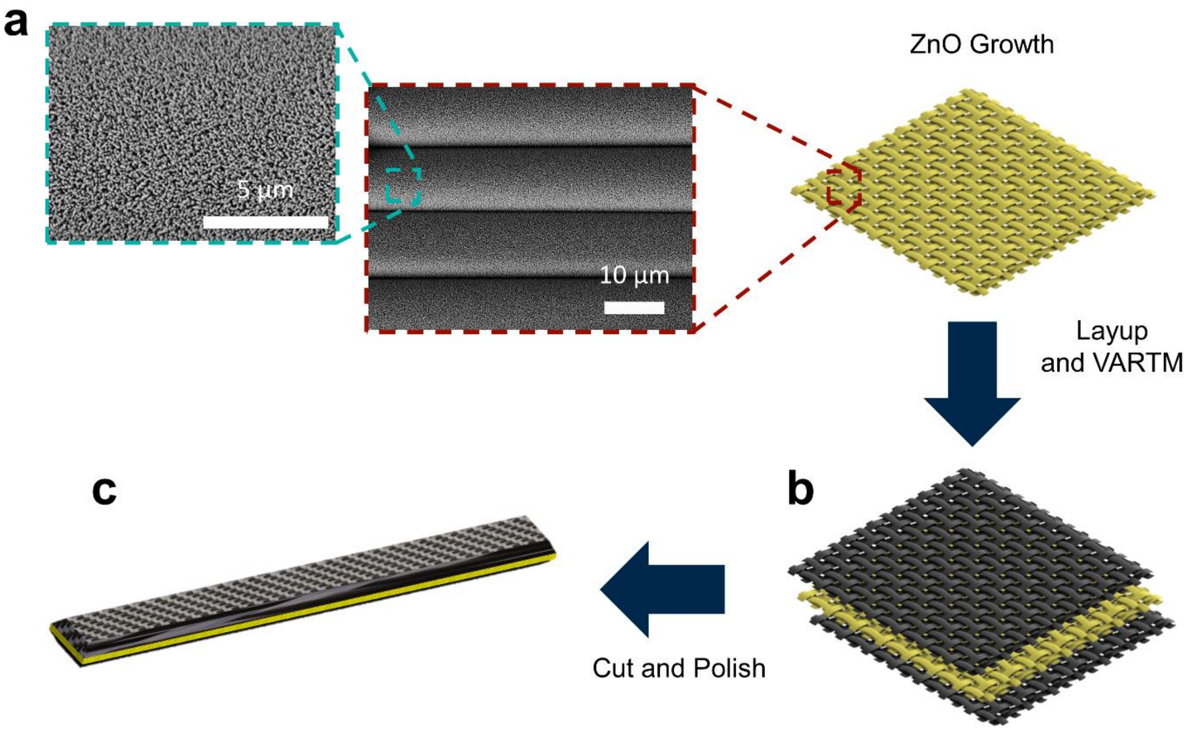

Figure 2.1. (a) SEM images of ZnO nanowires on aramid fabric. (b) Schematic of stacking sequence. (c) Schematic of final composite specimen.

2.2.2. Dehydrofluorinated Polyvinylidene Fluoride Prepreg Fabrication

2.2.2.1. Dehydrofluorination Process

The DHF PVDF used here was fabricated using concepts first explored by Lin et al. [110]. When subjected to basic or high temperature environments, PVDF loses hydrogen fluoride (HF) in a process referred to as dehydrofluorination which results in thermally stable electroactive properties. In this case, 1,8-diazabicyclo(5.4.0)undec-7-ene (DBU) (98+%, Acros Organics^{TM}) was selected as the preferred base due to the relatively moderate rate and controllability of the reaction. Specifically, 0.1 wt% DBU was added to 7 wt% PVDF (Kynar 301F) powder dissolved into N,N-dimethylformamide (DMF) (Certified ACS, Fisher Chemical) and thoroughly mixed. The mixture was then left for one hour, as the dehydrofluorination reaction progressed. The resulting PVDF mixture was then slowly poured over DI water mixed with 1 vol% HCl (Certified ACS Plus, Fisher Chemical) to terminate the reaction. The precipitated DHF PVDF, which forms as a consequence of the hydrophobicity of PVDF, was simultaneously collected from the fluid surface during the pouring process. The collected DHF PVDF film was then rinsed with additional DI water and HCl at the same concentration used previously, after which it was sonicated in DI water and HCl for ten minutes. Following the sonication, the film was thoroughly rinsed with pure DI water and sonicated again in DI water for ten minutes. The rinsing and washing process was then repeated three times with ethanol to ensure no DMF or DBU remained trapped in the collected DHF PVDF product. Following the completion of the full cleaning process, the DHF PVDF was thoroughly dried in a convection oven at 55 °C for several hours.

2.2.2.2. Fiber-Reinforced Prepreg Preparation

Once the DHF process was completed, 10 – 15 wt% dried DHF PVDF product was thoroughly dissolved in DMF using shear mixing (Flackteck speedmixer DAC 150.1 FVZ). The DHF PVDF solution was then poured over two stacked layers of S-glass, plain weave fabric (US Composites Style 6533) and subsequently dried at 80 °C under vacuum for 5 – 10 hours to form a prepreg. Once the DMF was fully evaporated, an additional thin layer of the DHF PVDF solution was added to the prepreg and fully dried under vacuum. This process was repeated several times until the combined DHF PVDF polymer layers reached the same thickness as the woven fiberglass. Following the evaporation of the DMF in the final layer of the matrix, the fiberglass/DHF PVDF prepreg was pressed for one hour in a hot press at 177 °C, which is the melting temperature of PVDF, and 100 psi (689.5 kPa) compression in order to fully and evenly infuse the PVDF matrix through the woven fabric and remove any air pockets. Following pressing of the PVDF into the plain weave fiberglass fabric, the prepreg was annealed at 180 °C for 20 minutes in an oven to encourage crystal growth for the formation of the electroactive γ- and β-phases, after which the prepreg was allowed to cool slowly at a rate of ~0.5 °C/min.

2.2.2.3. Characterization of Dehydrofluorinated Polyvinylidene Fluoride

The merit of the dehydrofluorination process lies in the concept that the formation of C=C bonds in the polymer backbone lead to rotational stiffness which induces formation of the β-phase rather than the normally thermodynamically stable α-phase [110]. This significant adjustment to the structure of the PVDF affects the preferred phase and results in increased crystallinity, primarily in the form of β-phase. To investigate the phase composition of the DHF PVDF at each stage of the fabrication process in this work and ensure the ferroelectric properties, Fourier-transform infrared spectroscopy (FTIR) was performed following the initial infusion, pressing, and annealing steps. It can be noted that the chemical composition and piezoelectric response of DHF PVDF are fully reported in the reference literature [110], thus FTIR was considered to be sufficient for the purposes of this work when investigating the phase composition of the DHF PVDF prepreg. The resulting spectra taken after each step can be seen in Figure 2.2 where the baseline refers to the initial DHF PVDF prepreg. It is clear from the figure that the initial combination of the PVDF with the fiberglass fabrics results in the formation of primarily electroactive (β+γ) phase PVDF as this is the preferred configuration. However, following the hot press treatment which fully infuses the PVDF through the woven fiberglass, the PVDF is found to be comprised of primarily α-phase. Since DHF PVDF has previously been shown to maintain β-phase in temperatures up to ~210 °C which is well above the temperature of the hot press step [110], it is assumed that this transition to α-phase under heat and pressure is a result of the fibers, which comprise the woven fabrics, physically limiting the crystal growth of the PVDF that is required to form γ-phase or β-phase. To encourage crystal growth and thus reintroduce additional electroactive potential, the pressed prepreg was annealed at 180 °C in an oven for 20 minutes and cooled slowly in the same oven to allow crystal growth. As seen in Figure 2.2, the resulting annealed surface shows an increase in the peaks corresponding to both γ-phase (811 cm^{-1} and 1234 cm^{-1} wavenumbers) and β-phase (1275 cm^{-1} wavenumber) or a combination (837 cm^{-1} and 1430 cm^{-1} wavenumbers) [123]. For the purpose of this work, the combination of both γ-phase and β-phase was considered to be preferential as both phases result in some piezoelectric coupling.

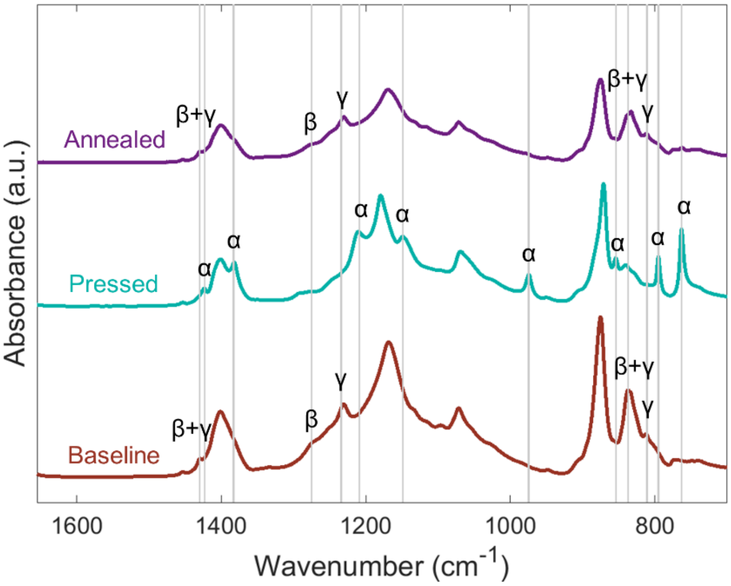

Figure 2.2. FTIR spectra of neat DHF PVDF infused in fiberglass (bottom), pressed DHF PVDF prepreg (middle), and pressed DHF PVDF prepreg following the annealing process (top).

2.2.2.4. Composite Layup and Sample Preparation

The resulting fiberglass/DHF PVDF prepreg was then combined with three total plies of plain weave carbon fiber (Hexcel® Style 282, received from Pacific Coast Composites) and infused with epoxy resin consisting of Epon 862 resin and curing agent Epikure 3230 (both received from Hexion) at a weight ratio of 100:35. A hand layup process was used in order to ensure even epoxy distribution on both sides of the DHF PVDF prepreg, after which the composite layup was cured at 80 °C under vacuum at 100 psi (689.5 kPa) for six hours. The final stacking sequence for both the three-point bend and tensile testing samples was two layers of carbon fiber, fiberglass and DHF PVDF prepreg, and one layer of carbon fiber. The described configuration allows for the sandwiching of the piezoelectric prepreg between conductive plies of carbon fiber, which act as electrodes in addition to their structural functionality, and the asymmetric layup increases the strain in the piezoelectric prepreg to improve the response. As a basis for comparison, baseline samples fabricated using neat fiberglass and carbon fiber with no DHF PVDF were also fabricated using the same layup methods and stacking sequence. In addition, to evaluate the effect of the DHF PVDF on the structural integrity of the interlaminar region, short beam shear (SBS) samples were fabricated by sandwiching the DHF PVDF prepreg between two stacks of seven plain weave carbon fiber plies. For comparison, a composite laminate with two layers of neat fiberglass sandwiched between seven layers of plain weave carbon fiber on each side (14 total carbon fiber plies) was also fabricated and infused with epoxy. Following the fabrication of the layups, the short beam, three-point bend, and tensile specimens were cut to the dimensions recommended by their respective ASTM standards. In the case of both the flexural and tensile specimens, this resulted in composite test specimens which were approximately 13 mm in width and 100 mm in length. It can be noted that additional length was added to the three-point bend samples beyond that recommended in ASTM D7264 to provide adequate space to attach wire leads to the samples. The cut flexural and tensile specimens were then polished to remove some carbon fiber at the edges of the sample and eliminate conductive pathways between the top and bottom carbon fiber plies, thus avoiding any conductivity through the thickness. As is recommended in ASTM standard D3039, fiberglass tabs were added to the ends of the tensile specimens using high shear strength epoxy (Loctite® EA 9430™ Hysol®). Additionally, a small section of the outer matrix layer was removed from the flexure and tensile samples, and wire leads (33-gauge copper wire) were attached close to the end of the test specimens using a combination of silver paint and quick-cure epoxy, enabling voltage measurements across the thickness of the sample without mechanically interfering with the testing. Finally, the three-point bend and tensile samples containing DHF PVDF were directly poled in oil at 1.2 MV/m and 150 °C for one hour. It can be noted that the electric field used for poling was lower than that which is typically seen for piezoelectric polymers. This is due to the increased risk of shorting due to the fibrous nature of the carbon fiber layers used as electrodes. However, the samples exhibited a sufficient piezoelectric response at this lower electric field. A schematic of the fabrication progress is depicted in Figure 2.3.

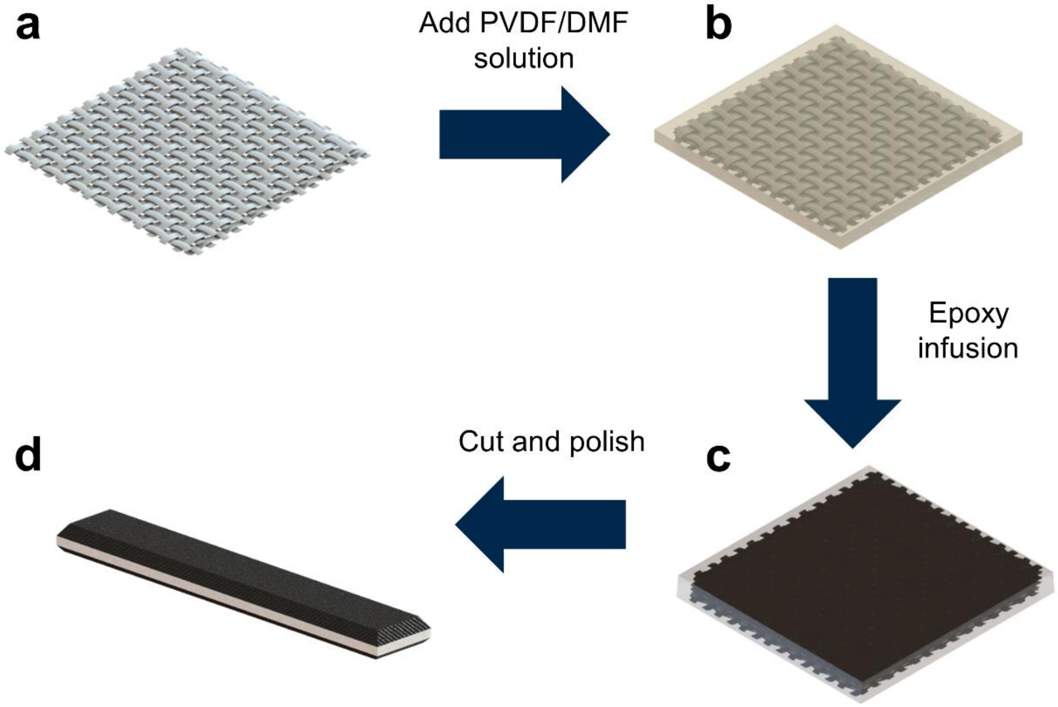

Figure 2.3. Schematic of (a) two plies of neat plain weave fiberglass, (b) fiberglass infused with PVDF, (c) final composite comprised of two layers of carbon fiber, fiberglass with PVDF, and one layer of carbon fiber with an epoxy matrix, and (d) final cut and polished sample.

2.2.2.5. Structural Analysis of Dehydrofluorinated Polyvinylidene Fluoride Composites

The composites containing DHF PVDF were investigated using SBS testing to confirm that no significant detriment occurred as a result of the DHF PVDF matrix. To accomplish this, the fabricated neat SBS samples were cut to dimensions of ~5.2 mm in width by ~15.6 mm in length for a thickness of ~2.6 mm as is outlined in ASTM standard D2344. The samples containing the DHF PVDF prepreg were slightly thicker at ~2.75 mm in thickness due to the added DHF PVDF and were cut to dimensions of ~5.5 mm in width and ~16.5 mm in length. The samples were then tested with the Instron Model 5982 load frame with a 100 kN load cell under three-point bend with a span of 4:1 per the same ASTM standard. Since interlaminar shear is the primary failure mode during short beam testing, short beam strength measurements allow for effective comparison of the interply strength of the composite containing DHF PVDF versus neat samples whose matrix is solely compromised of epoxy.

The resultant SBS strength of the neat composite in comparison to that containing the DHF PVDF prepreg is shown in Table 2.1. According to these results, the SBS strength of the composite containing DHF PVDF is found to be < 8% less than that of neat composites. This gives some indication that the interlaminar bonding between the DHF PVDF matrix and the epoxy is not equivalent to that between epoxy and itself. However, previous works have also indicated that the SBS strength of both carbon fiber and fiberglass composites are shown to decrease with increasing thickness and size [124, 125]. Therefore, a portion of the observed decrease in the SBS strength of the DHF PVDF composites may be attributed to the increased thickness of the composites containing the DHF PVDF prepreg (2.75 mm thick) over that of the baseline composite (2.6 mm thick). Although the interlaminar region of the composite is affected, added functionalities of both self-sensing and potential energy harvesting were gained due to the ferroelectricity from the addition of the DHF PVDF prepreg. Additionally, the plies used for the short beam samples fabricated in this work were stacked such that the weaker DHF PVDF layers were at the center of the composite layup where the highest shear stress is experienced, thus producing the maximum decrease in SBS strength. In practice, the DHF PVDF prepreg can be placed at any position in the thickness, provided conductive carbon fiber plies are located on either side of the piezoelectric material to produce a layup replicating the makeup of a traditional piezoelectric sensor. Thus the < 8% decrease in SBS strength can be further minimized by more strategic placement of the functional layers within the composite laminate.

Table 2.1. Short beam strength and sample thickness for neat composite samples and those with DHF PVDF.

	Short Beam Shear Strength	**Thickness**
Neat	45.4 ± 1.7 MPa	2.6 mm
DHF PVDF	41.8 ± 1.1 MPa	2.75 mm

2.3. Three-Point Bend Testing

2.3.1. Experimental Setup

The completed ZnO, DHF PVDF, and neat composite sample sets were first tested under flexural loading using an Instron 5982 load frame with a crosshead speed of 1 mm/min. The load frame was used to directly measure the applied load and the sample extension during testing, while a high-frequency microphone (PCB 426A05) and signal conditioner (PCB 482A16) were used to detect damage using acoustic emissions throughout each test. Airborne acoustics have also independently been demonstrated to be an effective method for damage detection in previous works [126]. The microphone was attached to the testing frame as close as possible to the test specimen without interfering with the testing mechanisms. The voltage across the thickness of each sample, baseline, ZnO, or DHF PVDF, was also measured during testing using the previously attached wire leads. For reference, an image of the test setup is shown in Figure 2.4. For the ZnO and neat composites fabricated with Kevlar, the voltage measurements were taken through a Keysight B2985A electrometer and collected using a National Instruments USB-4431 data acquisition (DAQ) system, however the DHF PVDF and neat composites fabricated with fiberglass were measured directly by the DAQ to reduce charging of the composite. It can be noted that this was necessary as the ZnO nanowires are semiconductors while the DHF PVDF is entirely electrically insulating and more prone to charging, thus the lower impedance of the DAQ resulted in a more accurate measurement. The acoustic emission measurements from the microphone were also collected through the duration of each test using the same DAQ, and a high-pass filter was applied to reduce the amount of external noise. It should be noted that nonconductive polyimide tape was placed on the load frame at the contact points to eliminate any electrical interference during the tests, and the voltage measurements did not receive any additional processing or pre-amplification.

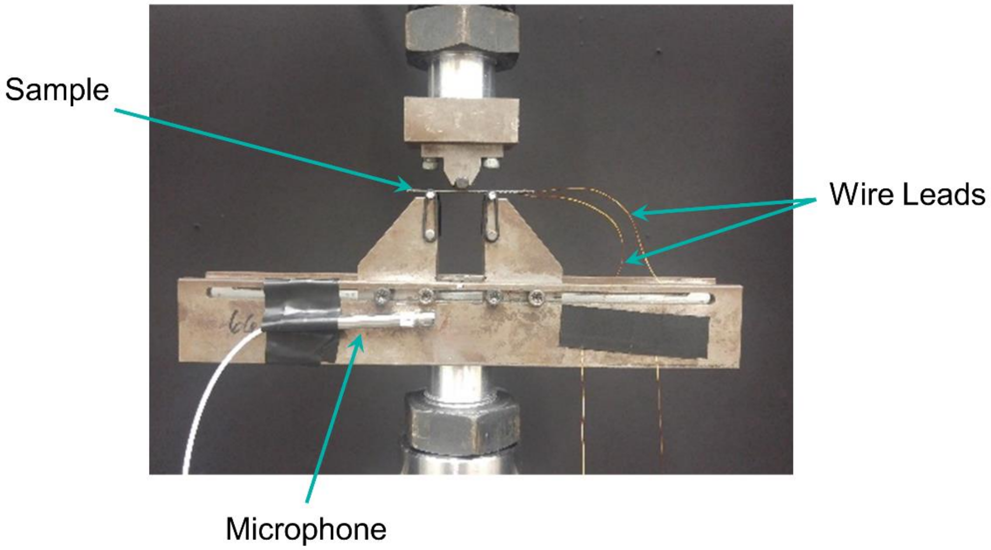

Figure 2.4. Image of the three-point bend test setup.

2.3.2. Zinc Oxide Composite Results

The purpose of the three-point bend test was to evaluate the ability of the completed composites to self-sense the progression of matrix cracking, interfacial debonding, and potential fiber breakage occurring under flexural loading. The resultant load, specimen voltage, and microphone reading all versus time for one representative functional composite containing piezoelectric ZnO nanowires are shown in Figure 2.5a through Figure 2.5c respectively. The figure clearly shows the progression of the test leading to the point of damage. Throughout the majority of the test, the applied load increases approximately linearly and the microphone pressure reading as well as the voltage across the sample remain relatively constant around zero until the point where initial damage, expected to occur in the form of matrix cracking, is evident in all three measurements. This evidence of damage occurrence is manifest by the sudden changes in the slope of the load curve, visually shown as drops in the applied load, which correspond to bursts in the acoustic reading from the microphone and sudden increases in the voltage measurements.

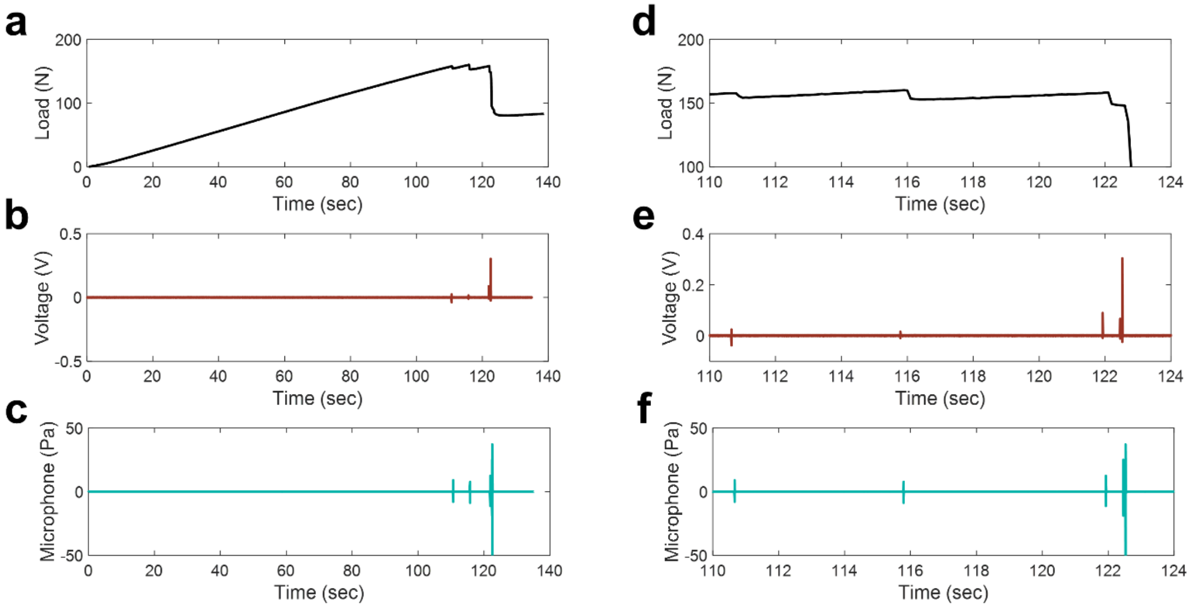

Figure 2.5. (a) Applied load, (b) measured voltage across sample, and (c) microphone reading for a sample containing ZnO during three-point bend test. Magnified section of (d) applied load, (e) measured voltage across sample, and (f) microphone reading during the same three-point bend test.

The final portion of the test duration during which measurable damage occurs is shown in Figure 2.5d through Figure 2.5f at a larger scale for further evaluation. As matrix cracking and debonding in the composite occur, a corresponding change in the measured load, sample voltage, and microphone reading can be observed. The detected emissions from both the microphone and the voltage reading show excellent coherence in both time of damage occurrence as well as the relative amplitude of the detected emissions, thus validating the ability of the voltage resulting from the ZnO to detect damage in-situ during the test. Several works have conclusively established the use of acoustic emission testing (AET) sensors similar to the high frequency microphone used in this work for detecting matrix cracking, interfacial debonding, and in some cases fiber breakage occurring during flexural loading, however the classification of such damage using AET signal features such as amplitude distribution is complicated [29, 127]. There is, however, a general agreement in the correlation between increasing amplitude and damage severity indicating the early damage detected by both the microphone and voltage measurements likely corresponds to matrix cracking while higher amplitude signals occurring later during testing are expected to correspond to interfacial debonding or fiber breakage. It is important to note that while the microphone is capable of detecting the same damage to the composite, the voltage measurement has the significant advantage of complete integration within the structure and omnipresent distribution throughout the entirety of the sample. Additionally, the spontaneous charge separation resulting from damage due to the direct piezoelectric effect results in the same measurable voltage over the entire area of the test specimen. Thus, the high conductivity of the distributed carbon fiber electrodes ensures the voltage measurement can be made at any point over the specimen surface area, not just at the point of matrix or fiber failure, which is promising for the scalability of the method to larger or more complicated structures.

2.3.3. Dehydrofluorinated Polyvinylidene Fluoride Composite Results

In addition, the applied load, microphone reading, and voltage across the thickness of a sample containing DHF PVDF are shown in Figure 2.6a through Figure 2.6c, respectively. As before, the occurrence of damage is observed by changes in the slope of the applied load corresponding to acoustic emission burst measurements from the high frequency microphone, and the voltage measurement across the composite samples containing DHF PVDF shows a response correlating to the same damage. Figure 2.6d through Figure 2.6f show the load, microphone pressure reading and voltage across the sample, respectively, during the latter portion of the test when the damage is observed to occur (final ~25%). From Figure 2.6e, the sample containing DHF PVDF exhibits a voltage emission as a result of the piezoelectric coupling of the DHF PVDF. As the sample is damaged in the form of matrix cracking or delamination during flexural loading, the

DHF PVDF is perturbed resulting in a separation of charge. Thus, the voltage across the two electrodes surrounding the dielectric is observed to increase as a result. It is also worthwhile to note that similar to the results observed from the ZnO sample, the amplitude of the voltage emission is shown to correlate to the amplitude of the acoustic emission readings from the microphone, indicating that the damage severity, which has been shown previously to correlate to AET amplitude [29, 127, 128], is equally detectable by the multifunctional composite itself. Thus, the need for an external structural health monitoring device or a system of discrete embedded sensors is eliminated by introducing an omnipresent ferroelectric sensing component fully integrated within the composite structure.

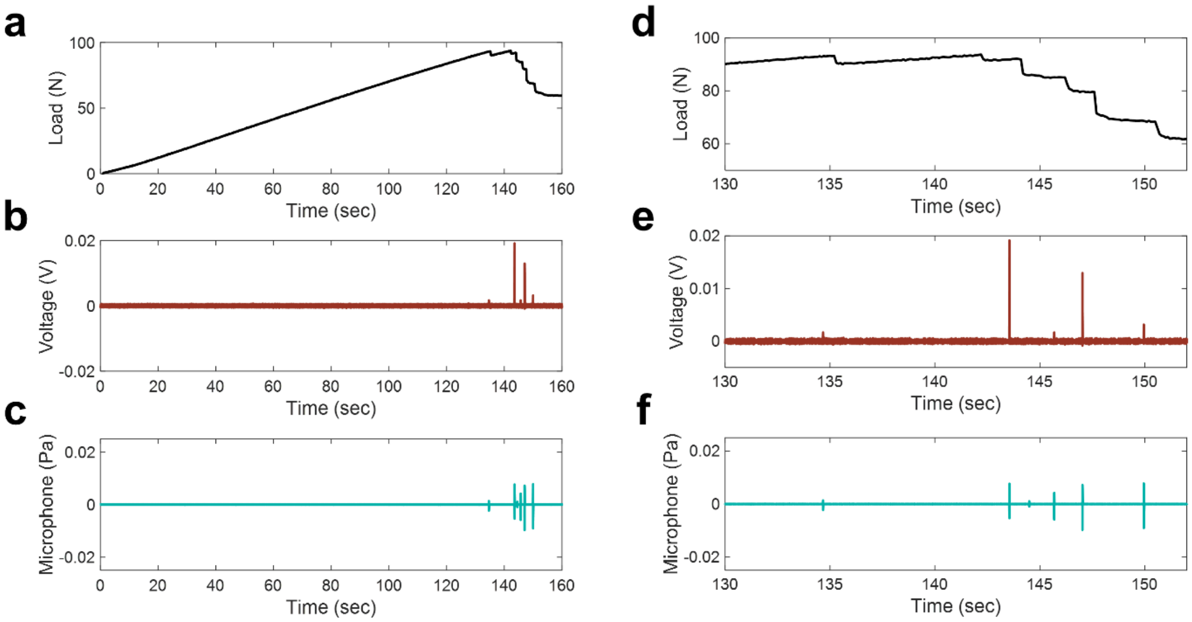

Figure 2.6. (a) Applied load, (b) measured voltage across sample, and (c) microphone reading for a sample containing DHF PVDF during three-point bend test. Magnified section of (d) applied load, (e) measured voltage across sample, and (f) microphone reading during the same three-point bend test.

2.3.4. Baseline Sample Results

To validate that it is in fact the piezoelectric nanowires and prepreg responsible for indicating damage rather than other constituents, several baseline samples containing no ZnO nanowires or DHF PVDF polymer were also tested using the same methodology and testing setup. The resulting load, test specimen voltage, and microphone reading, all versus time for one baseline composite specimen fabricated using neat aramid fabric sandwiched between carbon fiber fabric can be seen in Figure 2.7a through Figure 2.7c respectively, while the same measurements for a composite specimen fabricated using neat fiberglass sandwiched between carbon fiber can be seen in Figure 2.7d through Figure 2.7f. As damage occurred within the loaded composite specimens, a corresponding release in mechanical energy resulted in a propagating elastic wave that was detected via the high frequency microphone. The validity of this methodology was confirmed here through the correlation between changes to the load curve and microphone acoustic emission measurements. In contrast to active load and acoustic emission measurements, the voltage measurements across the bare samples remain relatively constant and show little to no measureable change in response to the damage. Thus, the baseline neat hybrid composite samples prove unable to detect damage using voltage measurements, indicating that the integrated piezoelectric component is indeed required for passive damage detection.

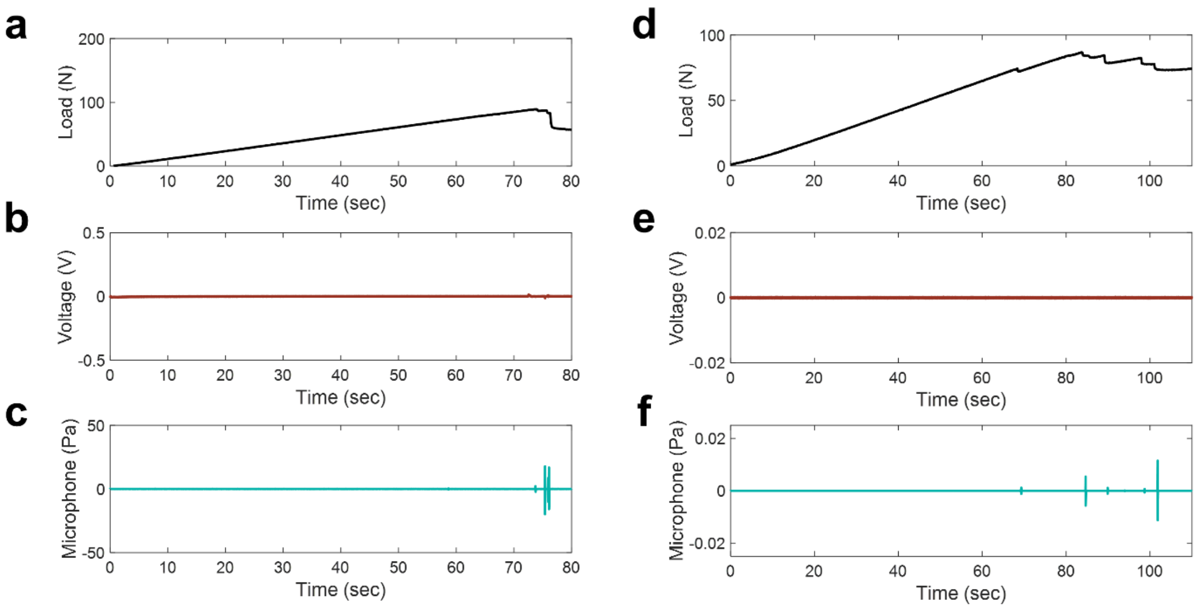

Figure 2.7. (a) Applied load, (b) measured voltage across sample, and (c) microphone pressure reading for a neat aramid-carbon fiber hybrid sample during three-point bend test. (d) Applied load, (e) measured voltage across sample, and (f) microphone pressure reading for a neat glass-carbon fiber hybrid sample during three-point bend test.

The results from both the baseline and functional samples combine to establish the functionality of composites containing integrated ZnO nanowires or the piezoelectric DHF PVDF prepreg for in-situ damage detection, as the voltage measurements indicate that the piezoelectric properties of the ZnO nanowires and DHF PVDF polymer are responsible for detectable voltage emissions resulting from composite damage. Additionally, the time of occurrence of the emissions as well as the relative amplitude are in line with signals detected by the external microphone indicating variance in the measured signal with damage severity. However, the type of damage the test specimen is exposed to in a three-point bend test is restricted primarily to matrix cracking and some interfacial debonding with limited fiber breakage, thus further testing is required to fully characterize the role of the integrated piezoelectric materials for in-situ damage detection during more extensive delamination and fiber failure.

2.4. Tensile Testing

2.4.1. Experimental Setup

To expand the information obtained from the three-point bend test, a standard composite tensile test was also completed for samples containing ZnO nanowires, samples fabricated with a DHF PVDF prepreg, and both aramid-carbon and fiberglass-carbon baseline samples without a piezoelectric element. To achieve this, the samples were loaded in a tensile test per ASTM standard D3039 using the same Instron Model 5982 load frame with a 100 kN load cell at a crosshead speed of 1 mm/min. As mentioned previously, fiberglass tabs were attached to the ends of the tensile samples which resulted in a gauge length of approximately 75 mm. The fiberglass tabs attached to the ends of each composite sample served a dual purpose as they both prevented slipping of the composite samples and acted as an electrically insulating barrier between the composite sample and the test frame. As with the flexural testing, the voltage across the thickness of the sample was monitored throughout the duration of the tests, and the same high frequency microphone and signal conditioner were once again used to confirm the damage via acoustic emissions. An image of the tensile test setup can be seen in Figure 2.8.

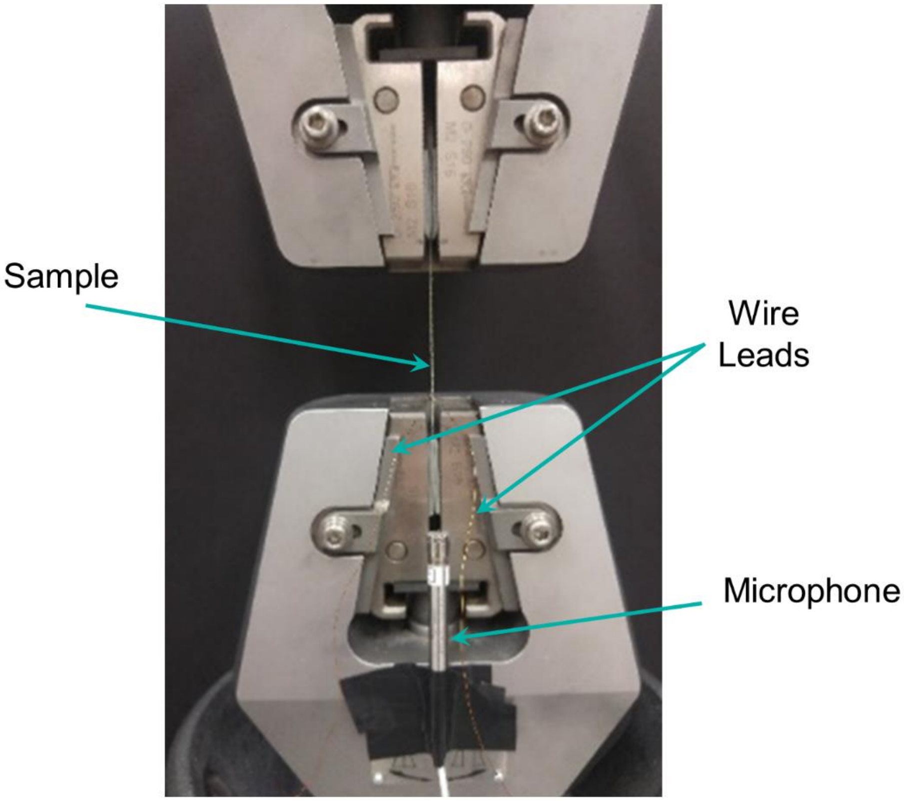

Figure 2.8. Image of tensile test setup.

2.4.2. Zinc Oxide Composite Results

In addition to further validating the detection of matrix cracking and interfacial debonding as seen during the three-point bend test, the tensile test also served to subject the test specimen to additional failure modes including widespread fiber failure. Moreover, an increased number of emissions from both the microphone and voltage measurements were detected due to the nature of the damage progression. As a result of the relatively high value of the applied load during the tensile test as compared to the change in load during minor damage, damage prior to catastrophic failure was not visible in the measured load as it was in the three-point bend test, however the microphone was again used to detect acoustic emissions resulting from matrix cracking, interfacial debonding, and fiber failure. As before, several samples were tested with each showing comparable results. A representative measured load, test specimen voltage, and microphone pressure reading for a test specimen with ZnO are shown in Figure 2.9a through Figure 2.9c respectively, with magnified voltage and microphone readings shown for a portion of the test in Figure 2.9d and Figure 2.9e, respectively. Although the coherence between emission measurements from the voltage and acoustics detected by the microphone is not exact, good correlation is seen in the majority of the test duration, indicating that the nanowires are again capable of detecting the same composite damage as more conventional methods with the benefit of full integration. Additionally, the close correlation between measurements also confirms that the functional composite is capable of detecting debonding or fiber breakage in both the reinforcing carbon fiber electrodes as well as the insulating aramid fabric with ZnO as damage to either material is detected by the acoustic emissions from the microphone.

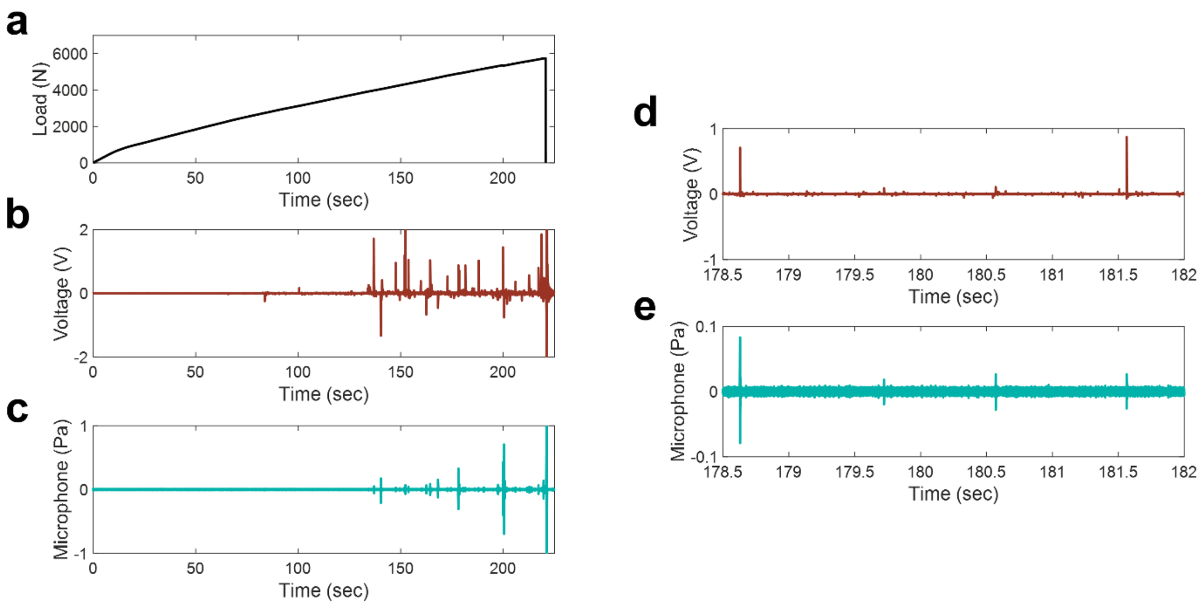

Figure 2.9. (a) Measured testing load, (b) voltage across test specimen, and (c) microphone pressure reading during tensile test of sample containing ZnO nanowires. Magnified portion of (d) voltage across test specimen and (e) microphone pressure reading.

A closer examination of the voltage emission during the tensile test as shown in Figure 2.10a and Figure 2.10b provides additional insight regarding the damage detection mechanism of the sample containing integrated piezoelectric ZnO. Rather than detecting an acoustic burst-type pressure wave as is seen in the microphone reading (Figure 2.10b), the composite sample instead acts as a capacitor which is initially charged as damage occurs and subsequently discharged (2.10a). The rate of decay thus closely aligns with the expected theoretical rate calculated using the appropriate time constant for the measured resistance and capacitance of the sample. The increase in measured voltage at the onset of the variety of damage types seen during testing is due to the inherent piezoelectricity of the individual nanowires which produce a corresponding charge as they are rapidly strained and mechanically perturbed. This charge was then detected via voltage output between the two external carbon fiber electrodes. The shape of the signal seen in this work is not unexpected as it closely aligns with the measurements seen in other works studying the use of ZnO nanowires or nanorods in flexible nanogenerators [129, 130].

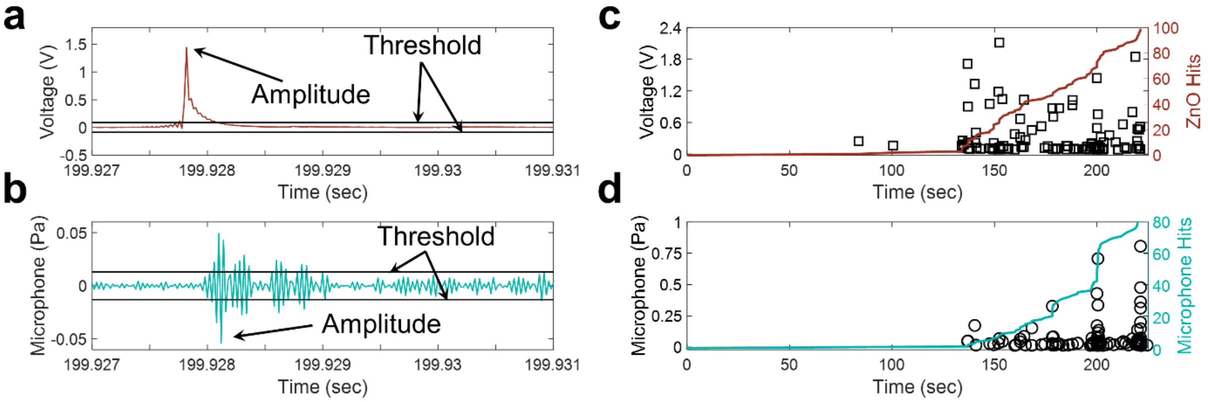

Figure 2.10. Example of a “hit” indicating damage detection from (a) the ZnO composite and (b) the AET microphone. Detected hit amplitude (left) and cumulative number of hits (right) versus time for (c) ZnO composite and (d) the AET microphone.

The signal measurements of the test specimen voltage can be further evaluated to produce various signal characteristics based on traditional AET in order to provide additional damage progression information. A minimum voltage threshold above the baseline noise level of both the baseline samples and the samples containing ZnO was defined for both the voltage measurement and the microphone pressure reading. Any instance of the voltage crossing the selected threshold was then defined as a “hit,” and the maximum absolute value of the voltage throughout the hit duration was defined as the corresponding “hit amplitude”. An example of the voltage hit, threshold, and amplitude of a voltage emission are shown in Figure 2.10a for clarity. As a basis for comparison, similar characteristics were also defined for the microphone burst signal as is seen in Figure 2.10b. In processing, each burst was defined as a single hit rather than counting each oscillation, and each hit was also required to be separated by 0.005 seconds to avoid recording echoes. To determine the threshold value, the root-mean-square (RMS) value of the baseline noise of both the voltage and microphone were initially calculated. An initial threshold was then selected for each data set and the RMS value of the detected hit amplitudes was calculated and divided by the RMS value of the baseline. The threshold of both the microphone and voltage was then iterated until the RMS signal to noise ratio (SNR) was within 10 between the two measurements. The threshold was thus designed to account for variance in baseline noise between the voltage and microphone as well as variance in relative signal amplitude during a hit. In the case of the data set presented, the voltage threshold was set to 87.5 mV and the microphone threshold was set to 13 mPa resulting in RMS SNR values of 1,998.6 and 1,996.7 respectively.

A scatterplot of the hit amplitude versus time during testing as well as the cumulative number of hits for both the test specimen voltage and the microphone pressure is shown in Figure 2.10c and Figure 2.10d respectively. The figure shows clear correlation between the damage detected using the developed functional composite and the established method using acoustic emissions. In both figures, and most notably the figure representing the ZnO voltage measurements, the hit rate increases dramatically as the specimen approaches total failure. This indicates the nanowires alone can be used to predict the onset of catastrophic failure by monitoring the cumulative number of hits as well as the average time separation between hits. A closer analysis of both scatterplots also shows a higher number of hits at lower magnitude. This result follows a similar trend to that of data obtained using traditional AET sensors as well as established alternative sensors in prior works which have correlated the emission amplitude with damage severity [29, 127, 128]. Using the method established in this work, it can be inferred that the hit amplitude from the ZnO nanowires corresponds to the severity of the detected damage, i.e. more frequently occurring low-level damage such as matrix cracking corresponds to low-amplitude voltage emission, while fiber failure can be expected to correspond to higher-amplitude voltage emission. Although the nanowires follow similar trends, which indicates their potential use in classifying damage, it should also be noted that the integrated nature of the sensing nanowire interphase may result in damage to the nanowires themselves as interfacial debonding and fiber failure occurs in the composite. This likely leads to a subtle decrease in the amplitude of the voltage output during such damage, resulting in a larger overlap between the amplitude distribution of matrix cracking with interfacial debonding and interfacial debonding with fiber breakage as the specimen approaches total failure. However, as previously stated, prior works have already established the difficult nature of classifying damage during in-situ detection using alternative methods. Additionally, the benefit of the integrated and omnipresent ZnO nanowire sensing interphase in detecting early stage low-level damage outweighs any loss in amplitude detection when the sample is near catastrophic failure.

2.4.3. Dehydrofluorinated Polyvinylidene Fluoride Composite Results

As expected due to their inherent piezoelectric properties, the composite samples containing DHF PVDF also showed an active voltage response during tensile testing. Figure 2.11a through Figure 2.11c show the applied load, voltage emission across the sample, and acoustic emission reading from the microphone for a representative DHF PVDF composite sample. Similar to what was observed from the ZnO sample and from the flexural loading, the sample shows a voltage emission correlating to acoustic emission readings from the high frequency microphone, which is particularly evident as the sample approaches complete failure. For greater clarity, the microphone pressure reading and voltage across the PVDF sample during a portion of the test is shown at higher magnification in Figure 2.11d and Figure 2.11e, respectively. As was discussed previously, the propagating waves detected by the microphone and the voltage emissions measured across the sample once again show correlation, not only in approximate time of occurrence, but in relative amplitude as well. This supports the assertion that the amplitude of the voltage emission, similar to AET measurements, corresponds to the significance of the damage. As previously stated, prior AET work has shown that the AET amplitude increases with damage significance, with matrix cracking being the least, followed by fiber matrix debonding and interlaminar delamination, while fiber breakage results in the highest amplitude emission [29]. In addition to the evidence shown in Figure 2.11, this phenomenologically holds true for multifunctional composites containing a piezoelectric component as well. While less significant damage such as matrix cracking results in only a small mechanical perturbation of the piezoelectric component, more significant damage such as delamination or fiber breakage results in a large mechanical change in strain, resulting in increased charge separation due to the direct piezoelectric effect, and thus a larger magnitude voltage emission measurement across the surrounding electrodes.

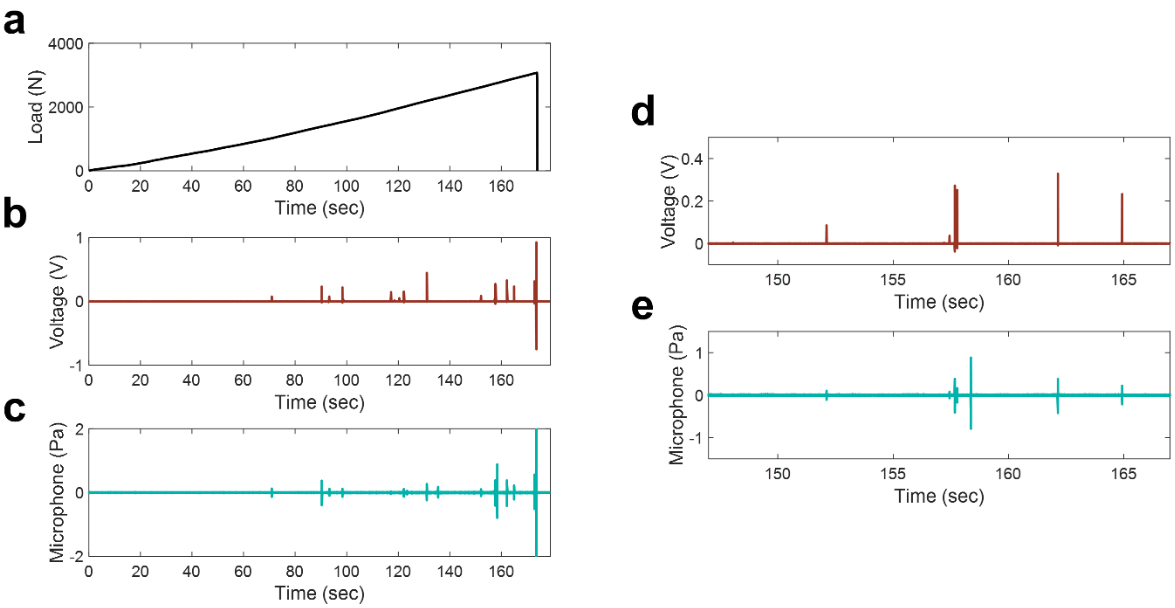

Figure 2.11. (a) Applied load, (b) sample voltage, and (c) microphone reading for one representative sample containing DHF PVDF during tensile testing. Magnified sections of the (d) voltage across the sample and (e) microphone reading to confirm damage detection.

To further analyze the response of the DHF PVDF hybrid composite using a similar method to the ZnO nanowire composite, a closer examination of the response mechanism of both the microphone readings and the voltage measurements across the sample was completed. A single acoustic emission burst detected by the microphone and the corresponding voltage emission measured across the sample are shown in Figure 2.12a and Figure 2.12b, respectively. From Figure 2.12b, the high frequency microphone functions as an AET sensor which detects the propagating waves resulting from damage. As damage occurs, a release in mechanical energy results in the propagation of an elastic wave that was detected by the microphone as a burst signal. In contrast, Figure 2.12a shows the corresponding voltage response to the same damage incident. Similar to the composites containing ZnO nanowires, the composite containing DHF PVDF was also designed and fabricated to possess the same fundamental functional components as a traditional piezoelectric sensor. As was previously discussed in Section 2.4.2, as the composite experiences an internal change in strain, charge separation occurs and results in the rapid increase in the voltage measurement. This is followed by a discharge manifested by an exponential decay, which is characteristic of capacitive components. Therefore, the combined results of both the ZnO and DHF PVDF indicate that the multifunctional composites act as capacitors that charge and discharge in response to a strain impulse resulting in the initial charge. The consistency in damage detection mechanism between the sample sets thus supports the assertion that this voltage emission damage detection mechanism is characteristic of composites fabricated with inherent piezoelectric sensing functionality.

To further evaluate the occurrence of damage, a minimum threshold was once again defined for both the microphone reading and the voltage measurement. In an effort to establish a fair comparison between damage detection methods, several requirements were met in determining the hit threshold for both the microphone and voltage measurements: (1) each burst signal recorded by the microphone was considered a single hit, (2) each hit was required to be separated by 0.005 seconds to eliminate the counting of reflective waves by the microphone, (3) an RMS SNR was defined by calculating the RMS value of the hit amplitudes divided by the RMS value of the baseline noise, and (4) the threshold of both the microphone and voltage was adjusted until the RMS SNR was within 10 between the two measurements. These requirements account for the difference in fiber reinforcement and sensing material between the ZnO and DHF PVDF composites which resulted in varying signal amplitudes from both the microphone and composite samples. Additionally, the threshold accounted for differences between the baseline readings of the voltage and microphone measurements and provided a fair comparison between the two measurements techniques to establish the effectiveness of the DHF PVDF against the widely accepted acoustic emission benchmark. The resulting RMS SNR values were calculated to be 1,259 and 1,252 for the microphone and voltage readings, respectively, which resulted in threshold magnitudes of approximately 25 mPa for the microphone reading and approximately 2.4 mV for the voltage reading. Using these defined thresholds, the amplitude of each hit and the cumulative number of hits versus time for both the microphone and voltage are shown in Figure 2.12a and Figure 2.12b, respectively. A visual examination of the data illustrates that the sample containing DHF PVDF shows comparable damage detection capabilities to the high frequency microphone in the approximate instance of occurrence, relative amplitude, and cumulative number of hits, indicating that the voltage emission method shows similar effectiveness to traditional AET. Therefore, voltage measurements taken directly from the composite allow for the tracking of the damage history of the composite for structural failure prediction and prevention purposes. However, unlike AET methods, the voltage emissions here are detected via the multifunctional composite itself, without any need for external sensors. Furthermore, the DHF PVDF is present throughout the entirety of the two-dimensional plane of the composite, therefore allowing for complete damage detection capabilities throughout the full area of the composite structure under investigation. To this end, it should also be noted that the woven carbon fabric comprising the top and bottom plies of the composite also serve as electrodes, which cover the two-dimensional plane of the composite, further supporting the omnipresent nature of the proposed sensing mechanism.

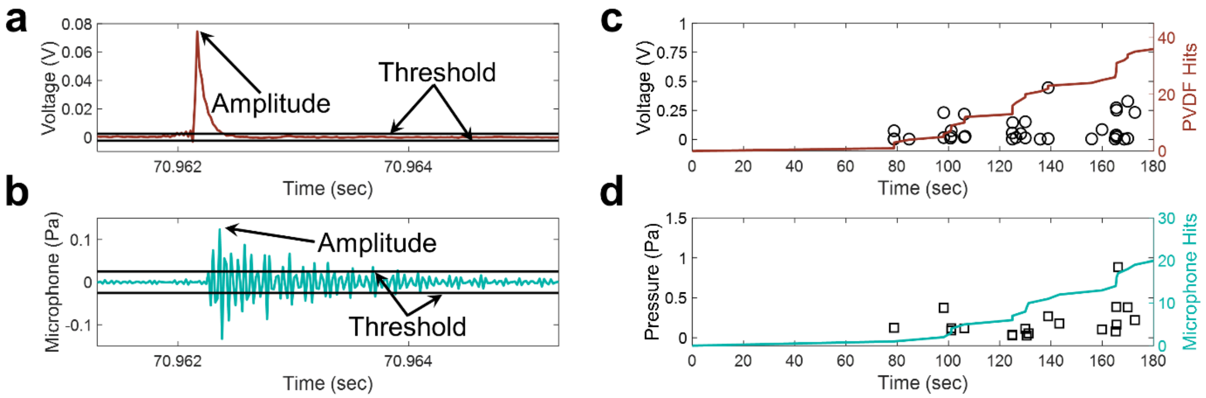

Figure 2.12. Example of a “hit” indicating damage detection from (a) the DHF PVDF composite and (b) the AET microphone. Detected hit amplitude (left) and cumulative number of hits (right) versus time for (c) DHF PVDF composite and (d) the AET microphone.

2.4.4. Neat Composite Sample Results

Finally, both samples containing neat aramid fabric with no ZnO nanowires and samples fabricated with neat fiberglass containing no DHF PVDF were also subjected to tensile testing to provide baseline measurements. The resultant applied load, voltage across the sample, and acoustic reading from the microphone for a representative neat aramid-carbon fiber hybrid sample are shown in Figure 2.13a through Figure 2.13c, respectively. The same measurements are also shown for a representative neat fiberglass-carbon fiber hybrid sample in Figure 2.13d through Figure 2.13f, respectively. As was observed during the tensile testing of the piezoelectric samples, the microphone pressure readings (Figure 2.13b and Figure 2.13e) show acoustic emission activity during the latter portion of the test (final ~30%). However, the voltage readings across both neat samples show no measurable activity due to the lack of any inherent sensing component. However, it can be noted that at catastrophic failure, the voltage measurements across the neat samples show an increase resulting from the complete failure of the sample leading to a rapid change in resistance and capacitance, as well as disturbance to or complete detachment of the wire leads attached to the surface of the samples which produce artifacts in the measurements. Thus, the results indicate that the baseline samples are incapable of sensing any damage prior to complete failure.

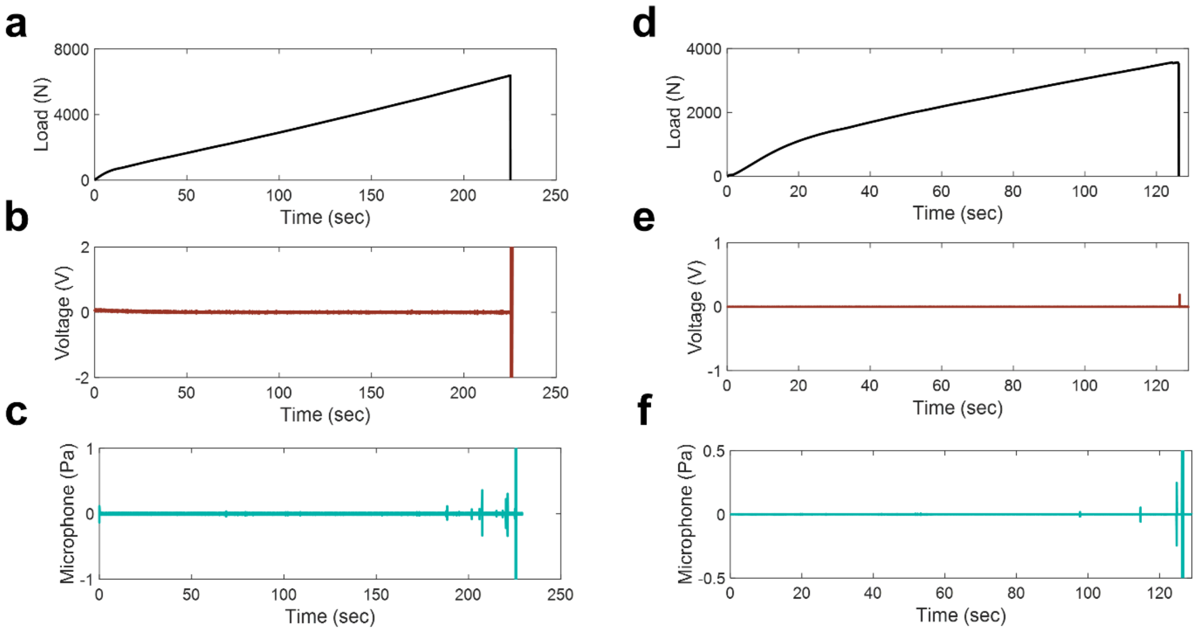

Figure 2.13. (a) Applied load, (b) voltage across sample, and (c) microphone reading for a neat aramid-carbon hybrid composite during tensile loading. (d) Applied load, (e) voltage across sample, and (f) microphone reading for a neat fiberglass-carbon hybrid composite during tensile loading.

2.5. Chapter Summary

In this chapter two multifunctional materials were characterized for damage sensing in fiber-reinforced composites: an interphase of piezoelectric ZnO nanowires on aramid fabric, and a piezoelectric DHF PVDF prepreg fabricated with woven fiberglass. The electrically insulating fabric with integrated piezoelectric components were then sandwiched between conductive carbon fiber electrodes. Thus, both the sensing materials and electrodes were comprised of structural materials and were fully distributed throughout the composite material allowing for the detection of minor damage in any location. Additionally, the same multifunctional composites have the potential to scavenge small amounts of power from ambient vibrations due to the piezoelectric coupling of the materials used. As a result, this work further advances the multifunctional nature the of composites containing ZnO nanowires and DHF PVDF polymer by conclusively establishing the ability of these materials to detect damage in fiber-reinforced composites during both flexural and tensile loading and validating the damage detected using acoustic emissions. Matrix failure, interfacial debonding, delamination, and fiber failure within the test specimens containing ZnO or DHF PVDF were shown to result in a spontaneous charge separation that could be detected via voltage output and was defined as a voltage emission. Each measured voltage emission was thus used to indicate the occurrence of damage, while the accumulation of such events indicated damage progression and the approach of catastrophic failure. Trends in both the distribution of hit amplitude as well as the rate of emissions during testing and the cumulative number of hits were shown to follow similar trends to those of traditional acoustic emission sensors; consequently, the performance of the piezoelectric nanowires and piezoelectric prepreg are comparable to traditional acoustic emission sensors with the significant added benefit of full incorporation into the entirety of the composite structure. As a result, this work overcomes major hurdles in the widespread application of alternative in-situ damage detection techniques by exploiting the ability of multifunctional structural composites to self-sense damage.

CHAPTER 3

In-Situ Strain and Damage Sensing Using Piezoresistive Laser Induced Graphene

3.1. Chapter Introduction

The focus of Chapter 3 is the use of fully integrated laser induced graphene (LIG) to create multifunctional materials with embedded piezoresistivity for the simultaneous and in-situ monitoring of both strain and damage in aramid fiber- and fiberglass-reinforced composites. Aramid and fiberglass reinforcement was selected for this work since both sets of fibers are electrically insulating, and the respective composites thus possess no inherent piezoresistive properties. The addition of LIG therefore adds additional functionality to these composites. To accomplish this, the LIG layers are integrated during the fabrication process either through the direct conversion of the surface of the fibers to LIG in the case of aramid fibers, or through transfer printing of the LIG to the surface of fiberglass prepreg before being laid up into the ply stack. The resultant LIG thus forms an interlayer in the interlaminar region of both fiber-reinforced composites. Each of the methods used in this work are simple and require no treatment or modification to the aramid fabric or commercial fiberglass prepreg prior to the addition of the LIG interlayers, which is promising for industrial scale use. The performance of the piezoresistive interlayers in monitoring strain and damage in-situ is demonstrated via three-point bend and tensile testing for each composite set. In the case of the fiberglass composites, the interlaminar properties were observed to be largely maintained with the LIG present in the interlaminar region of the composite, while the damping properties were found to be improved. The interlaminar properties of the aramid composites were observed to increase with the addition of the LIG. This work therefore introduces novel multifunctional materials with fully integrated sensing capabilities through cost-effective and scalable processes.

3.2. Sample Preparation and Composite Layup

Two separate methodologies were used to integrate LIG within the aramid and fiberglass-reinforced composites. The processes used as well as the resultant LIG and composite properties for each set of test specimens are discussed in the following sections.

3.2.1. Laser Induced Graphene on Aramid Fabric

3.2.1.1. Laser Induced Graphene Fabrication Process

Aramid-based fiber-reinforced composites with LIG were fabricated based on the work of Lin et al. [111]. It is worthwhile to note that common methods and equipment were used and the aramid fabric received no treatment or chemical modification prior to the generation of the graphene from the aramid surface. The as-received plain-weave aramid fabric (Kevlar® KM2+, style 790, CS-800, 4.3 oz/yd^2, received from BGF Industries) was first coated with graphene via a laser irradiation process using a 40 W CO_2 laser engraver (Epilog Zing 16 universal laser system) operating in raster mode. During the laser process, the surface fibers of the aramid fabric are converted to a porous graphene coating, which remains attached to the surface of the fabric as the aramid itself is used as the precursor for the LIG generation. During the laser irradiation, the pulsed laser photothermally converts the sp^3-carbon atoms to sp^2-carbon atoms without the need for an external graphene source [111]. To ensure optimal mechanical performance of the aramid fiber-reinforced composites, the LIG was generated on the aramid fabric at an output power of 20%, an impulse per unit area of 400 dots per inch (DPI), and laser raster speed of 1 $cm^2 \cdot s^{-1}$ [119]. For sensitivity comparison, two sets of fabrics were prepared, one set with LIG on only one side, and a second set with LIG on both sides of the aramid fabric.

3.2.1.2. Laser Induced Graphene Characterization

To evaluate the quality of the LIG coating on the surface of the aramid, characterization using scanning electron microscope (SEM) imaging was completed. In this case, a JEOL JSM-7800FLV field-emission SEM was used to image the surface of the fabric which can be seen in Figure 3.1. Traditionally, the untreated aramid fabric surface consists of smooth, individual aramid fibers which lack the necessary roughness for a strong interfacial bond in a fiber-reinforced polymer matrix composite (Figure 3.1a – c). However, by subjecting the fabric to a defocused laser irradiation process, the high temperature poly(p-phenylene terephthalamide) (PPTA) is converted to amorphous carbon of various surface morphologies. It should be noted that this conversion only takes place on the surface fibers, and the remainder of the aramid fibers, which make up the majority of the weave, remain unaffected. The morphology and properties of the resulting carbon microstructure are dependent on the processing parameters such as the raster speed, raster density, and power. By generating the LIG at an operating power of 20%, the aramid surface exposed to the laser is covered with a fuzzy LIG morphology that is capable of providing mechanical reinforcement to the interlaminar region of the aramid composite (Figure 3.1d – i) [119]. Further observation under SEM confirms that the LIG is comprised of a uniform layer of fuzzy microfibers which is approximately 10 – 15 µm in height. Once embedded within the final composite, this LIG layer was found to be approximately 6.5 – 7 µm thick in the one-sided configuration, which is below the diameter of a single Kevlar® filament, and 15 µm thick in the double sided configuration [119]. The morphology shown in Figure 3.1d – i is an accurate representation of the layer covering the full surface area of the fabric that is exposed to the laser. The resulting areal density of the single-sided LIG-coated aramid fabric is 0.0261 g/cm^2 while the areal density of the double-sided LIG-coated aramid fabric is 0.0228 g/cm^2. For reference, the areal density of neat aramid fabric is 0.0281 g/cm^2. The fabric density is decreased during the LIG process due to the conversion of the exposed fibers to porous LIG. It should be noted that the reported areal densities are that of LIG-coated fabrics and not that of the individual LIG layer or of LIG-coated composites with the supporting matrix. Rather, the weight of the fabric was measured using a high precision balance before and after the laser irradiation process. Given the reported low yield of the laser irradiation process (< 5%), it is expected that the measured weight post-treatment is primarily that of the aramid fabric [118].

The primary merit of the LIG surface coating presented here is the piezoresistive layer provided to the originally electrically insulating aramid fabric. At a power of 20%, the single-sided aramid composite specimens, which are those with fabric coated on one side with LIG, have a resistance value of 100 – 800 Ω for width between 11 – 14 mm and length between 85 – 110 mm. At the same laser power, the double-sided aramid composite specimens, which are those with fabric coated on both sides with LIG, have an initial resistance between 60 – 100 Ω for width between 11 – 14 mm and length between 85 – 110 mm. It can be noted that the variations in resistance values are attributed to the need to manually adjust the defocusing distance of the laser. Additional analysis of the double-sided resistance values relative to the single-sided resistance values shows that adding the resistance of two equivalent single-sided samples in parallel results in a value that is similar to the values obtained from the double-sided sample. Thus, it can be inferred that each LIG surface on a single ply acts similarly to two resistors in parallel. It should be noted that the resistivity of the fabric can be further decreased by increasing the power of the laser or the raster pulsing density; however, the chosen parameters were used in order to generate a surface morphology capable of providing mechanical reinforcement to the composite and therefore taking advantage of the structural performance of the LIG [119]. In summary, the LIG coating provides the insulating aramid fabric with a multifunctional piezoresistive layer that, when monitored, is capable of providing information about the damage state of aramid fiber-reinforced composites.

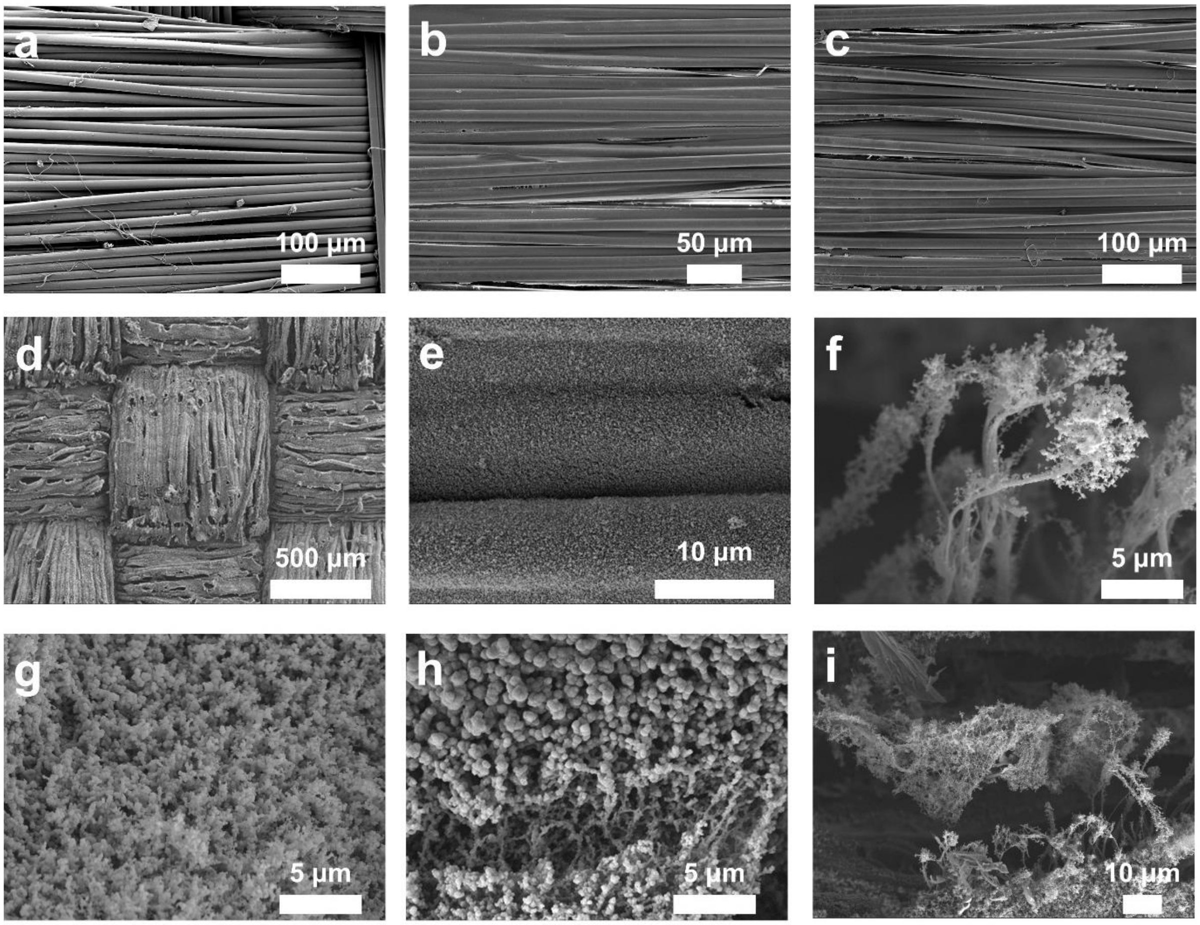

Figure 3.1. (a – c) SEM images of the untreated aramid surface. (d – i) SEM images of LIG on aramid surface.

In addition to the qualitative analysis completed using SEM, Raman spectroscopy was also used to chemically characterize the LIG microstructure. The resulting spectra for both the untreated aramid fabric as well as the aramid fabric with LIG can be seen in Figure 3.2. From Figure 3.2a, the untreated aramid fabric has peaks at 1517 cm^{-1}, 1569 cm^{-1}, 1608.5 cm^{-1}, and 1647 cm^{-1}, all of which are characteristic of aramid fabric [118]. In contrast, Figure 3.2b shows that the aramid fabric with LIG displays peaks at 1354 cm^{-1}, 1580 cm^{-1}, and 2699 cm^{-1} which are representative of the D-band, G-band, and 2D-band of graphitic structures, respectively. The degree of aramid fabric surface graphitization can be evaluated by examining the ratio between the G- and D-bands (I_G/I_D). Pristine graphene shows no D-band peak, and instead shows a strong G-band peak [131]. With an increasing number of defects in the graphene or decreased distance between defects, the strength of the D-band peak relative to the G-band peak increases [131]. For reference, the LIG on polyimide film, which is the original substrate, was reported to have an I_G/I_D ratio of 2.5 [111]. In contrast, the I_G/I_D ratio of the LIG in this work is ~1.2, which indicates low graphene quality from the LIG on the surface of the fabric, however, the quality observed here is similar to that seen in previous analyses of LIG on aramid fabric [118, 119]. Additionally, the added conductivity is sufficient for in-situ resistance measurements and damage detection, while also maintaining the specific strength of the aramid fabric. Therefore, the resulting LIG is of sufficient quality for introducing multifunctionality to the aramid reinforcement.

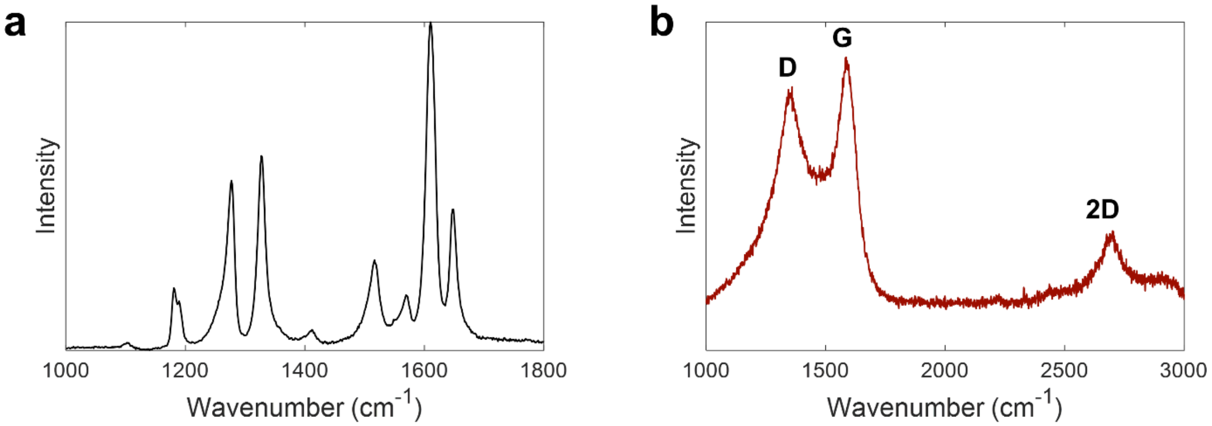

Figure 3.2. Raman spectroscopy of (a) untreated aramid fabric and (b) aramid fabric coated with LIG.

3.2.1.3. Composite Fabrication and Resultant Properties

Following the completion of the LIG process, three layers of LIG-coated aramid were used as preforms and then infused with an epoxy resin consisting of Epon 862 resin and Curing Agent W (both received from Hexion) at a ratio of 100:26.4 using a standard vacuum-assisted resin transfer molding (VARTM) process. The composite was then cured at 177 °C under 100 psi (689.5 kPa) pressure for three hours in a hot press. It should be noted that the conductivity of the fabric was maintained throughout the VARTM process indicating that the LIG remained intact throughout the layup procedure. After the epoxy matrix was fully cured, the composite panels, with thickness between 0.85 – 0.9 mm, were cut to dimensions of ~11.2 mm in width and ~85 mm in length according to ASTM standard D7264 for three-point bend testing, however, additional length was added to each sample to allow for the attachment of wire leads for electrical measurements during testing. Similarly, composite panels were also cut to dimensions of ~12.5 mm in width and ~160 mm in length for tensile testing according to ASTM standard D3039. Fiberglass tabs were then attached to the ends of the tensile test samples using high shear strength epoxy (Loctite® EA 9430™ Hysol®) as is recommended in the ASTM standard. Finally, the specimens were coated around their perimeter with silver paint, and 33-gauge copper wires were connected to each silver paint ring using a combination of silver paint and epoxy (Loctite® Epoxy Instant Mix™ 5 Minute). A schematic of the completed test specimen can be seen in Figure 3.3f. The described process was completed for both single-sided LIG aramid as well as double-sided LIG aramid as is shown in Figure 3.3b and Figure 3.3c respectively. An image of the neat Kevlar® fabric used is shown as Figure 3.3d and an image of Kevlar® fabric coated with LIG is shown in Figure 3.3e for reference.

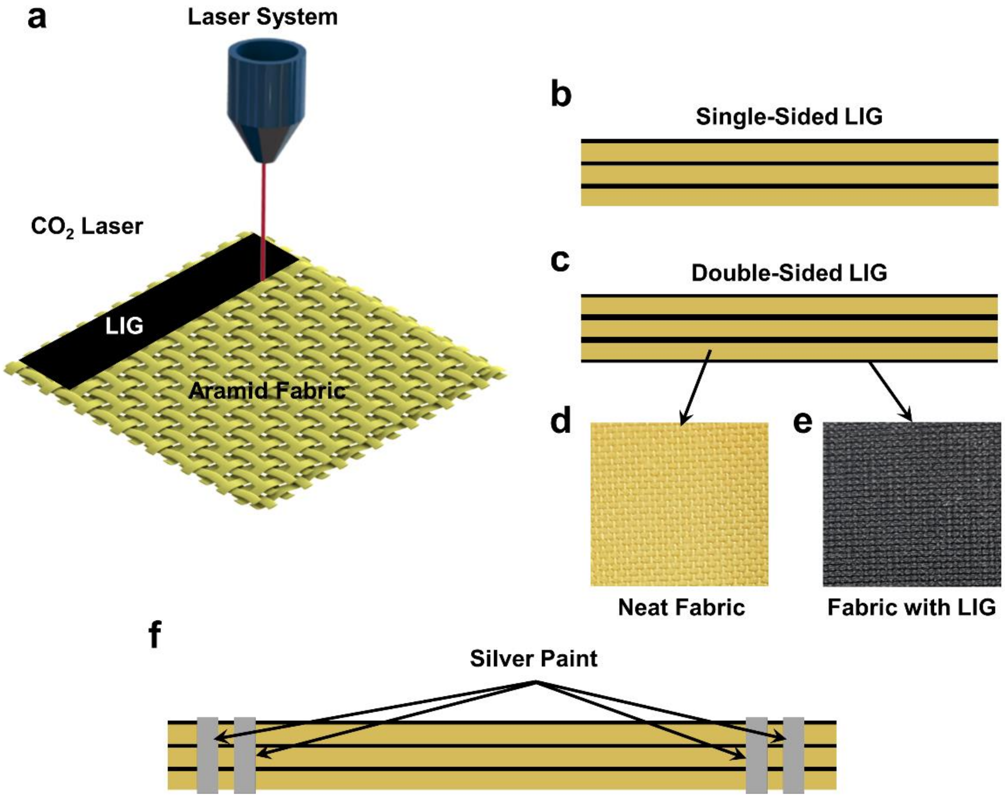

Figure 3.3. (a) Schematic of LIG process on aramid fabric, (b) schematic of single-sided LIG aramid sample layup, (c) schematic of double-sided LIG aramid layup, (d) image of untreated aramid fabric, (e) image of aramid fabric coated with LIG, and (f) schematic of final composite sample.

The structural characteristics of the aramid fiber-reinforced composites with LIG were investigated by Nasser et al. [119]. The results from that work conclusively show that the addition of the LIG in the interlaminar area of the composite, using the same fabrication methods used in this chapter, results in increased interlaminar properties. Specifically, the short beam shear (SBS) strength of the single-sided LIG aramid composites exhibited a 55% increase over that of the neat aramid composites, while the double-sided LIG samples resulted in a 46% increase in SBS strength over the neat composites [119]. Furthermore, both the single-sided and double-sided composites were shown to possess improved Mode I fracture toughness in comparison to the untreated composites, with a maximum improvement of 20% observed from the single-sided samples [119]. These enhanced mechanical properties were attributed to improved mechanical interlocking and chemical interaction between the fiber reinforcement and the binding matrix. Moreover, the increased interlaminar properties are achieved without detriment to the tensile strength of the fabric normalized by the areal density, which was shown to be maintained for both the single- and double-sided samples [119].

3.2.2. Laser Induced Graphene on Fiberglass Prepreg

3.2.2.1. Laser Induced Graphene Interlayer Fabrication Process

The LIG interlayer in the fiberglass-reinforced composites was also fabricated based on the work of Lin et al. [111], similar to the LIG process used for aramid fabric described in Section 3.2.1.1. However, since the formation of LIG relies on the polymeric makeup of the substrate used during the laser irradiation process, a novel transfer printing process is adopted here to integrate LIG within fiberglass prepreg that has not yet been developed or used with LIG and fiberglass prepreg. To generate the LIG, the same Epilog Zing 16 universal laser system with a 40 W CO_2

infrared laser described previously was used to generate the textured graphene films on 2 mil (0.0254 mm) thick Kapton® polyimide tape sheets at a pulsing density of 400 dots per inch (DPI) and power of 14%, as illustrated in Figure 3.4a and Figure 3.4c. It should be noted that variation in the power, speed, and DPI can be used to adjust the density and resistivity of the resulting LIG patterns [115]. The graphene layer resulting from the parameters used in this work has a fuzzy texture which is transferrable to the tacky surface of the uncured fiberglass prepreg (CYCOM® E773 epoxy prepreg with S-2 glass fiber-reinforced roving), resulting in preservation of the microstructure and the printed pattern.

Once the LIG layer was complete, the graphene was transferred to a fiberglass prepreg using a constant-pressure rolling process, where the prepreg was slightly heated to approximately 80 °C in order to ensure the matrix was softened for the embedment of the LIG. During this process, the LIG coating is rolled onto the tacky prepreg causing the LIG to adhere to the prepreg surface and detach from the remaining polyimide film. As a result, the LIG is completely transferred from the Kapton® tape to the tacky surface of the prepreg, yielding a conductive surface in the same pattern as was originally printed onto the Kapton®, which is illustrated in Figure 3.4b and Figure 3.4d. Two sets of prepregs were prepared using the transfer printing process: one set with LIG covering the entire surface of the fiberglass prepreg (Figure 3.4a – b), and another with the graphitic microstructure printed onto the Kapton® in serpentine patterns between 10.15 – 20.32 mm in width and 25.4 mm in height (Figure 3.4c – d) to form LIG strain gauges. The effective length of the printed serpentine patterned LIG was varied by controlling the length of the pattern printed (Figure 3.6c) in order to vary the resistance of the strain gauge for additional characterization.

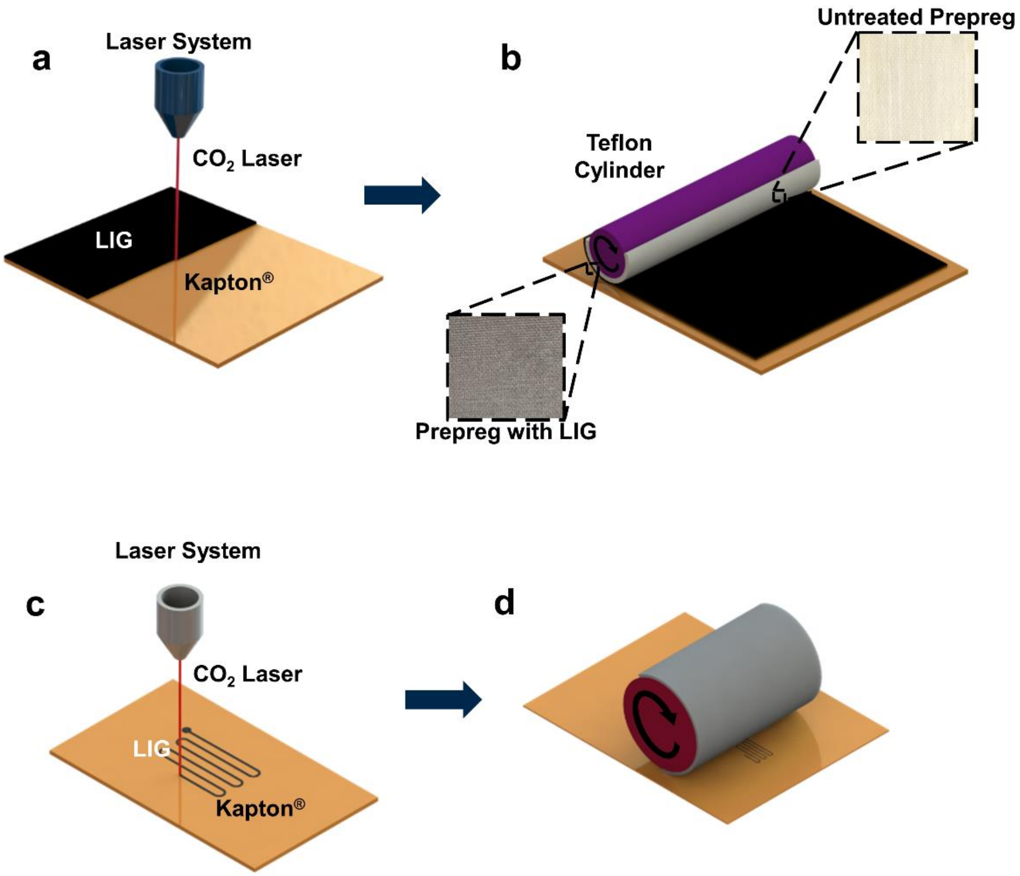

Figure 3.4. (a) Schematic of laser printing process and (b) schematic of transfer printing process for continuous LIG interlayer. (c) Schematic of laser printing process and (d) transfer printing process for LIG strain gauges.

3.2.2.2. Laser Induced Graphene Characterization

The LIG surface on the Kapton® tape directly after printing was characterized using SEM, and the resulting images which are shown in Figure 3.5a and Figure 3.5b indicate that the LIG consists of a porous nanostructure which is comprised of interlaced graphene fibers. The nanostructure of the LIG can be controlled by varying the output power and pulsing density of the laser, however, the nanostructure seen in Figure 3.5 was determined to provide the most effective transfer from the polyimide tape to the prepreg, thus resulting in the most advantageous conductivity for piezoresistive measurements. Additionally, to confirm the structure of the LIG was not altered during the transfer process from the polyimide tape to the fiberglass prepreg, additional SEM images were taken of the LIG coated prepreg surface following the transfer. As can be seen in Figure 3.5c – d, the LIG nanostructure remains intact following the transfer, maintaining a similar surface morphology and alignment as was seen following the initial laser treatment (Figure 3.5a – b). It should be noted that the fuzzy texture observed is drastically changed from the initial smooth surface of the as-received fiberglass prepreg which is shown in Figure 3.5g – h. It is also clear from Figure 3.5e – f that post-curing, the LIG is embedded within the matrix of the fiberglass prepreg following the transfer, thus reinforcing the matrix in a controlled manner prior to the layup of the composite. During the curing process, the matrix solidifies around the LIG thus fully integrating the LIG within the composite.

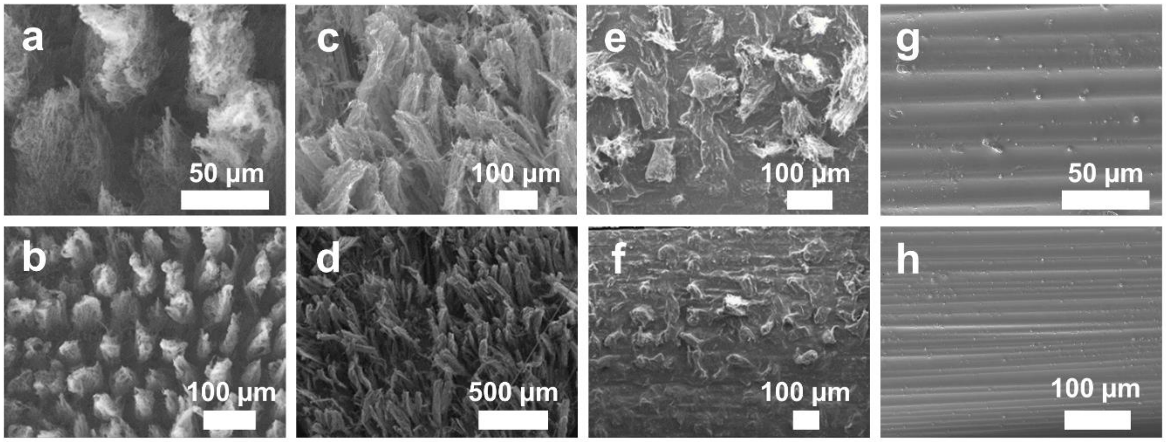

Figure 3.5. (a – b) SEM image of LIG coating on polyimide tape. (c – d) SEM images of LIG coating on uncured fiberglass prepreg. (e – f) SEM images of LIG coating on cured fiberglass prepreg. (g – h) SEM images of cured neat fiberglass prepreg.

3.2.2.3. Composite Fabrication and Resultant Properties

Following the introduction of the LIG, four sets of samples were fabricated using the prepreg with a continuous LIG interlayer covering the entire surface for both mechanical and functional analysis. First, 16 layers of unidirectional LIG-coated fiberglass were combined to assess the short beam shear (SBS) properties. To evaluate the damping characteristics, three layers of unidirectional LIG-coated fiberglass were combined, while three layers of fiberglass with LIG were also stacked together at [+45/-45/+45]° for three-point bend testing. Finally, two sets of three-ply composites of unidirectional and [+45/-45/+45]° plies were fabricated for tensile testing to assess the ability of both unidirectional and angled composites to detect tensile strain. Neat fiberglass samples were also fabricated using the same number of layers for both the SBS and dynamic testing to provide a basis for comparison. To fabricate fiberglass samples with an integrated LIG strain gauge, two additional plies of neat unidirectional prepreg were added to one ply containing the transferred LIG strain gauge to complete the layup for mechanical testing. The ply with the transferred strain gauge was placed on top in the layup to enable direct strain measurements from the composite. The prepreg layers for each composite layup were then pressed at 127 °C and 100 psi (689.5 kPa) in a hot press under vacuum for two hours as is recommended by the manufacturer. Once the composite layups were completed, the samples with continuous LIG interlayers were cut to their respective widths and lengths as recommended by each ASTM standard, however additional length was added to the three-point bend samples for the addition of wire leads used for the application of current and voltage measurements during testing. Additionally, to reduce slipping and create a non-conductive barrier between the sample and the load frame, woven fiberglass composite tabs were added to the ends of the tensile samples using high shear strength epoxy (Loctite® EA 9430™ Hysol®). Furthermore, four silver paint rings were added to each three-point bend and tensile sample with a continuous LIG interlayer, with two rings at each end as can be seen in Figure 3.6a. Since the LIG was located throughout the entire plane of the fabricated composite, the silver paint around the edges formed a conductive contact between plies. The outer rings served as contact points where the current was applied, and the inner rings were contacts for voltage measurements using the four-probe method for resistance monitoring. Wire leads (33-gauge copper wire) were then added to each silver paint ring using a combination of silver paint and epoxy (Loctite® Epoxy Instant Mix™ 5 Minute). The samples with a serpentine LIG strain gauge (Figure 3.6b) were cut to a width of 25.4 mm and length of 101.6 mm, and wire leads (33-gauge copper wire) were directly attached to the conductive LIG strain gauge ends using a combination of silver paint and epoxy (Loctite® Epoxy Instant Mix™ 5 Minute). Finally, a commercial strain gauge was attached to the surface of the completed composite tensile specimens to provide reference strain measurements (Figure 3.6c). The resulting resistance values of the 3-ply samples with the LIG covering the entire surface of the prepreg range between 100 – 1,000 Ω for the angle ply and unidirectional composites, both of which were 11 – 14 mm wide and 65 – 76 mm long. The serpentine patterned LIG possessed resistance values from approximately 14 – 80 kΩ.

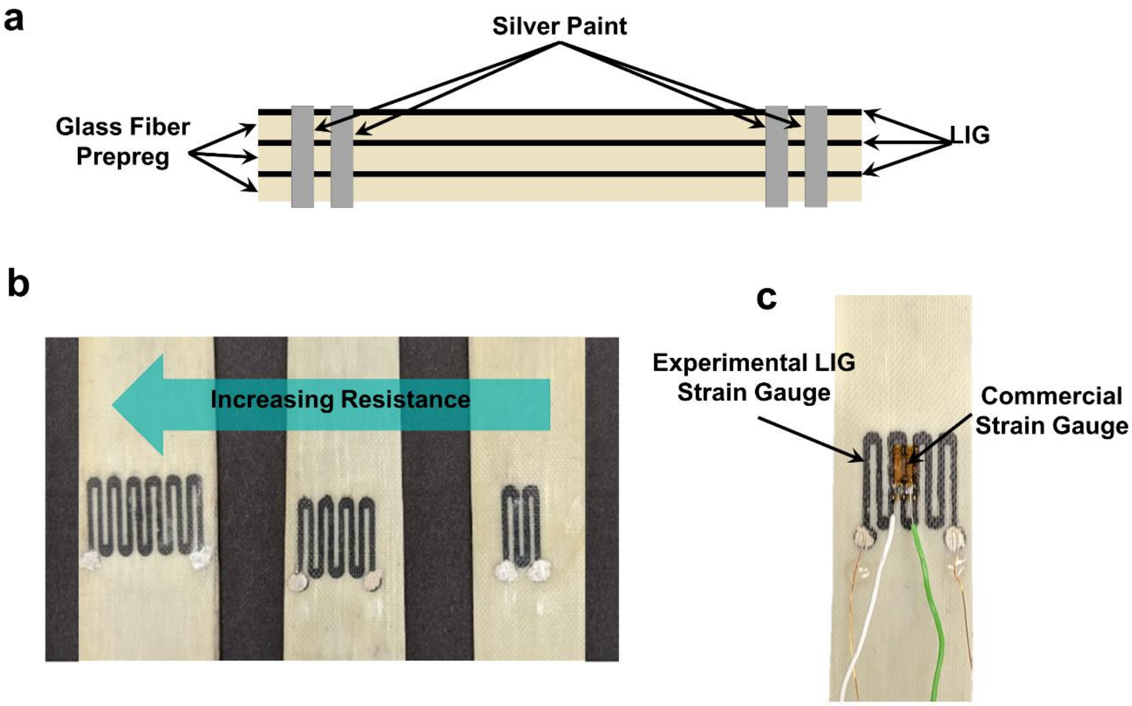

Figure 3.6. (a) Schematic of completed test specimen with continuous LIG. (b) Image of transfer printed strain gauges with varying resistance. (c) Image of completed sample with serpentine patterned LIG and commercial strain gauge.

To evaluate the viscoelastic properties of the fiberglass-reinforced composites containing LIG, dynamic mechanical analysis was performed on 3 neat fiberglass samples and 3 fiberglass samples containing LIG. The composite samples, which were approximately 0.8 mm in thickness, were cut to dimensions of 60 mm in length and 10 mm in width in accordance with the suggested testing parameters for the TA Instruments Q800 dynamic mechanical analyzer (DMA). The composite beams were then tested using a dual cantilever clamp at 10 Hz from room temperature (~20 – 25 °C) to 200 °C with heating at a ramp rate of 5 °C/min. Neat fiberglass-reinforced composites without LIG were also tested using the same setup and testing parameters for direct comparison of the viscoelastic properties of the composites. To evaluate the relative damping of the composites, the ratio between the loss modulus (E'') and storage modulus (E'), known as tan δ, was measured directly by the DMA and was the primary parameter considered here. The damping properties of fiberglass-reinforced composites play an important role during dynamic loading which is commonly experienced in aircraft and automobile applications among others [132]. Furthermore, to confirm that the addition of the LIG does not significantly affect the curing process of the LIG, two samples, one neat fiberglass prepreg and one fiberglass prepreg with LIG were tested using differential scanning calorimetry analysis (DSC). The samples were heated to 126.67 °C at a rate of 2.75 °C/min, following the curing cycle recommended by the manufacturer, and the heat flow was monitored to evaluate the cure.

The results of the DSC analysis from both a neat fiberglass prepreg composite and a fiberglass prepreg composite with LIG are shown in Figure 3.7a. From the results, both the neat fiberglass and fiberglass with LIG follow the same trend throughout the cure cycle, thus indicating that no significant change to the curing reaction of the composite due to the addition of the LIG is observed. Additionally, the resulting storage modulus, loss modulus, and tan δ averaged between the samples tested are shown in Figure 3.7b – d, respectively. The results shown in the figure clearly indicate an increase in damping as observed in the average tan δ at the peak temperature, while the storage modulus remains relatively constant between the sample sets. Thus, the addition of the LIG interlayer within the fiberglass composites contributes damping to the material at the peak physical displacement experienced at the transition temperature, which is calculated to be a ~12% increase in tan δ, while the damping at low temperature is maintained. The increase at the transition temperature is attributed to additional surface area between the fibers and the matrix due to the addition of the LIG, in combination with the stick-slip phenomenon resulting from the interfacial friction between the fuzzy LIG and the matrix. Stick-slip behavior is commonly observed in composites containing carbon nanotubes (CNTs) due to the poor chemical bonding between the CNTs and the polymer matrix [133]. The carbon-based LIG is likely to exhibit similar behavior with the dominant mode of energy dissipation relying on friction at the interface between the LIG and the matrix. The mechanical energy from vibration of the sample is dissipated as heat through the interfacial friction resulting in the improved damping. It should also be noted that since commercial prepreg was used for both sets of composites, the amount of epoxy matrix relative to the fiber content was held constant between the sample sets, so the fraction of epoxy does not play a role in the increase in damping. The LIG coating is therefore considered to be fully responsible for any observed increase in composite damping between the two sample sets. For reference, the mean value and standard deviation of the tan δ of both the untreated and LIG-treated samples at low temperature (50 °C) and the peak value at the transition temperature are shown in Table 3.1.

Prior to the addition of the LIG interlayer, no treatment to the fibers was needed in this work, and since the LIG was introduced to the surface of existing commercial prepreg, the fibers were not altered or damaged during the transfer process. However, the LIG considerably modifies the structure of the interlaminar region of the composite, therefore, to confirm that the presence of the LIG does not weaken interply strength and increase the risk of delamination, the SBS strength of the fiberglass composites with the LIG surfaces was established using SBS testing. To accomplish this, SBS specimens were cut from the 3 mm thick panel to dimensions of 6 mm wide by 18 mm long, as specified in ASTM standard D2344. Three-point bend testing was then performed to assess the SBS strength of the composites containing LIG compared to neat fiberglass prepreg samples. The primary mode of failure in SBS testing is located within the interlaminar region, thus this method of testing provides crucial information regarding the effect of the LIG on the interply strength of the composite. The tests were completed per ASTM standard D2344 with a span to thickness ratio of 4:1, and 12 samples were tested for each data set using an Instron load frame (Model 5982) with 100 kN load cell. The thickness of both the neat fiberglass composite and the LIG coated fiberglass composite was approximately 3 mm, thus the addition of the LIG interlayer was not found to increase the thickness of the composite samples. The sample thickness has a significant effect on the short beam shear strength [125], therefore, since changes in the thickness were negligible, a direct comparison between the neat samples and samples containing LIG was possible. The SBS strength of the composites containing LIG was found to be approximately unchanged relative to that of the neat composites, with the LIG having a SBS strength of 90.4±1.1 MPa and the untreated samples having a SBS strength of 91.2±1.34 MPa (see Table 3.1). In addition, an analysis of variance (ANOVA) test of the data reveals a p-value of 0.16, which is much higher than the typical cutoff value of 0.05, indicating that the null hypothesis is not rejected, and a statistically significant difference in the SBS strength is not present. Therefore, these results confirm that the addition of the LIG to the surface of the fiberglass prepreg does not significantly weaken interlaminar adhesion between adjacent plies, thus avoiding an increase in the probability of delamination during application.

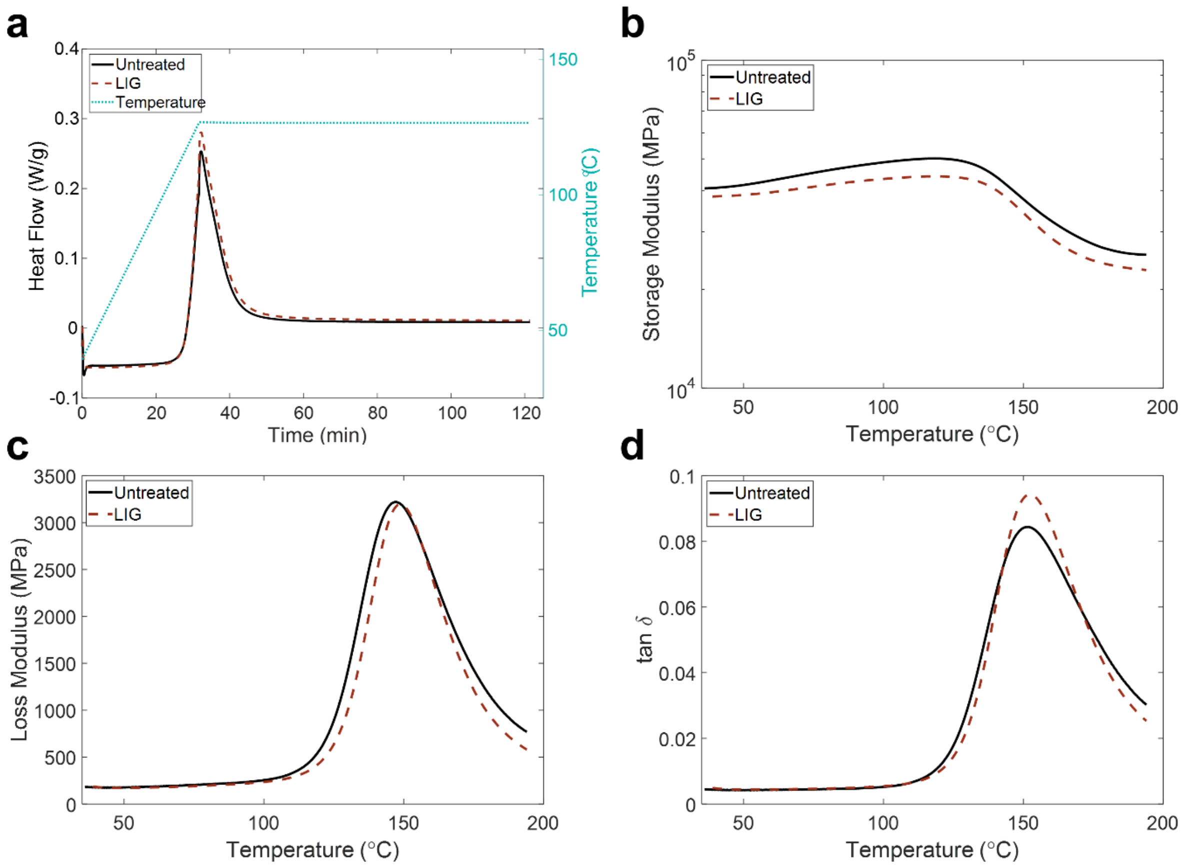

Figure 3.7. (a) DSC results of heat flow versus time for a neat fiberglass sample and a fiberglass sample with LIG during curing cycle. Average (b) storage modulus, (c) loss modulus, and (d) tan δ of untreated fiberglass and fiberglass with LIG.

Table 3.1. SBS strength, tan δ at low temperature, and peak tan δ values for untreated fiberglass composites and composites with LIG.

	Short Beam Shear Strength	**tan δ @ 50 °C**	**Peak tan δ**
Untreated	91.2±1.34 MPa	0.0043±0.00014	0.084±0.008
LIG	90.4±1.1 MPa	0.0044±0.0002	0.094±0.003

3.3. Strain Sensing in Aramid and Fiberglass Composites

3.3.1. Experimental Setup

Following the completion of the sample fabrication, each sample set was subjected to quasi-static cyclic tensile testing. Reference strain measurements were obtained using a commercial strain gauge (VISHAY® micro-measurements & SR-4 general purpose strain gauge, 120±0.3% Ω, 2.075±0.5% gauge factor) that was mounted to the surface of the sample (Figure 3.6c) and coupled with a Wheatstone bridge and millivolt amplifier (Omega™ model MN1400-4). The constant voltage input for the Wheatstone bridge used with the commercial strain gauge was provided by a Hewlett Packard model 6217A DC power supply. The resistance of the LIG was monitored using a second Wheatstone bridge, in combination with a Transducer Techniques TMO-2 signal conditioner. A schematic of the measurement method is shown in Figure 3.8. An Instron model 5982 with a 100 kN load cell was used for tensile testing, and the samples were subjected to quasi-static cyclic loading to a pre-defined maximum stress. Prior to testing, current was applied to the bridge for several minutes to allow the LIG sample to thermally equilibrate. Following completion of the test, the gauge factor of the LIG samples was identified using a linear fit of the resistance change to the true strain measured by the commercial strain gauge for each cycle.

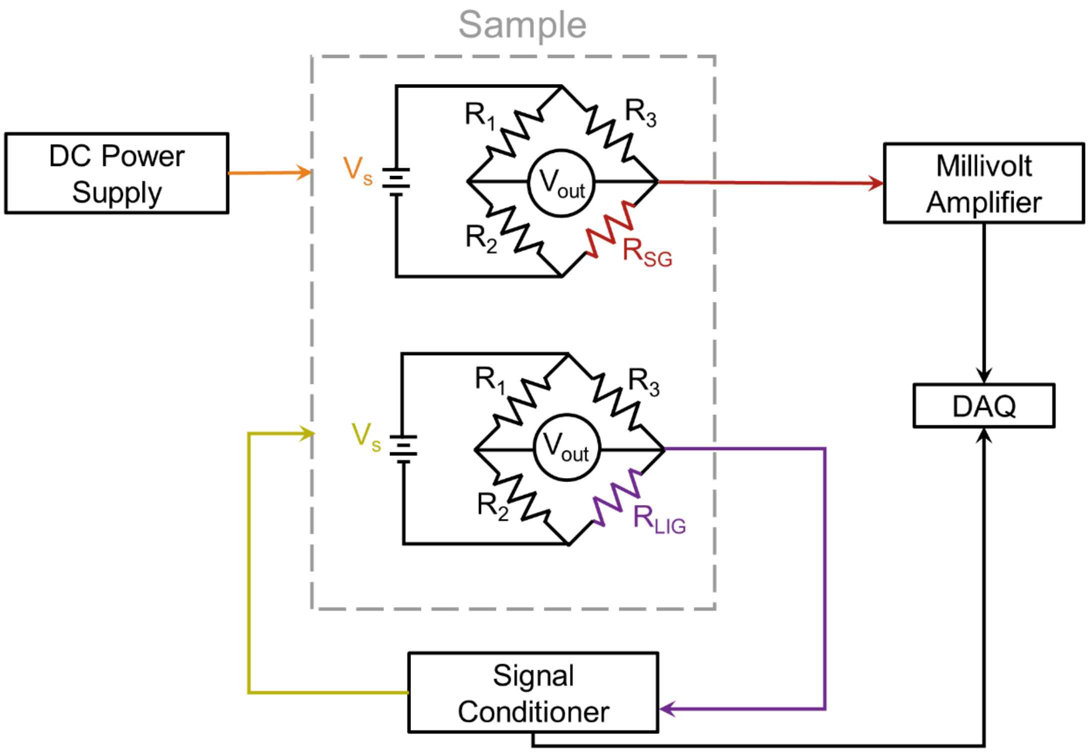

Figure 3.8. Schematic of measurement methods for one test specimen.

3.3.2. Strain Sensing in Aramid Fiber-Reinforced Composites

Given the similar strain tracking behavior displayed by both single- and double-sided aramid sample sets when subjected to initial tensile loading, only the response of single-sided LIG coated aramid composites under repeated loading and unloading was investigated. Additionally, the single-sided samples have a higher maximum tensile load (although the specific strength is maintained for both sample sets [119]), therefore larger applied loads are possible prior to initiating significant damage within the sample. The samples were loaded and unloaded quasi-statically at a crosshead speed of 1 mm/min for several cycles between 0 MPa up to predetermined maximum stress levels of ~20, ~50, and ~100 MPa, and one precycle was allowed for stabilization. The maximum stress was varied between samples to determine repeatability of the sensing mechanism and to separate the strain and damage sensing capabilities. The resulting percent change in resistance and the strain of the sample versus time can be seen in Figure 3.9a – c for the samples loaded to ~20, ~50, and ~100 MPa, respectively. To evaluate if plastic deformation or damage occurs within each cycle, the initial value of the stress, strain, and resistance are all considered. Changes in the trend between initial stress and strain indicate mechanical changes to the modulus of the composite which occur during plastic deformation or damage to the sample. At very low values of applied stress (~20 MPa), the initial strain remains relatively constant throughout the test, as shown in Figure 3.9d. As the sample is unloaded and the stress approaches zero, the strain also returns to a value close to zero, indicating that no significant damage occurs within the sample as the composite is within the elastic regime. Throughout each cycle, the electrical resistance of the specimen follows the trend of the strain, thus the LIG is conclusively able to track the strain of the sample in the absence of damage. As the applied stress is increased to ~50 MPa (Figure 3.9b and Figure 3.9e), the initial strain begins to trend upward with increasing cycles. Since the sample is loaded and unloaded to the same stress values, the residual strain can be attributed to plastic deformation within the sample. The initial resistance, however, remains relatively constant, indicating that the plastic deformation is below the sensing threshold, until the stress is further increased to ~100 MPa. In Figure 3.9c and Figure 3.9f, the initial strain shows irregularity and a slight trend upward, which indicates that some plastic deformation and damage are occurring within the sample. Similarly, the initial resistance also shows an increasing trend with each cycle as the plastic deformation and damage are compounded. The observed increasing trend in residual resistance is similar to responses seen from composites containing CNTs when cyclically loaded [59, 68, 134], and is attributed to the irreversible separation between carbon-carbon contacts of the LIG on the aramid surfaces resulting from micro-damage during initial tensile loading and low-levels of plastic deformation in the aramid fabric. Therefore, from Figure 3.9a and Figure 3.9b, the samples are capable of repeatedly tracking low values in strain, while the increase in resistance after loading and unloading at higher loads above a certain threshold (Figure 3.9c) allows for retrospective detection of micro-damage due to the permanent increase in resistance from the initial measured value. The gauge factor of the first two samples was calculated for each cycle (Figure 3.9g) according to the equation shown in Figure 3.9g, where ε is the reading from the commercial strain gauge, R is the resistance of the composite, and R_0 is the initial resistance. The average gauge factor of Sample 3 was not considered since Sample 3 experienced damage and plastic deformation as was previously discussed. Thus, the average gauge factor of the undamaged samples is ~0.81, which is lower than the gauge factor of most commercial strain gauges. However, the integrated nature of the LIG used in this work overcomes this small decrease in gauge factor.

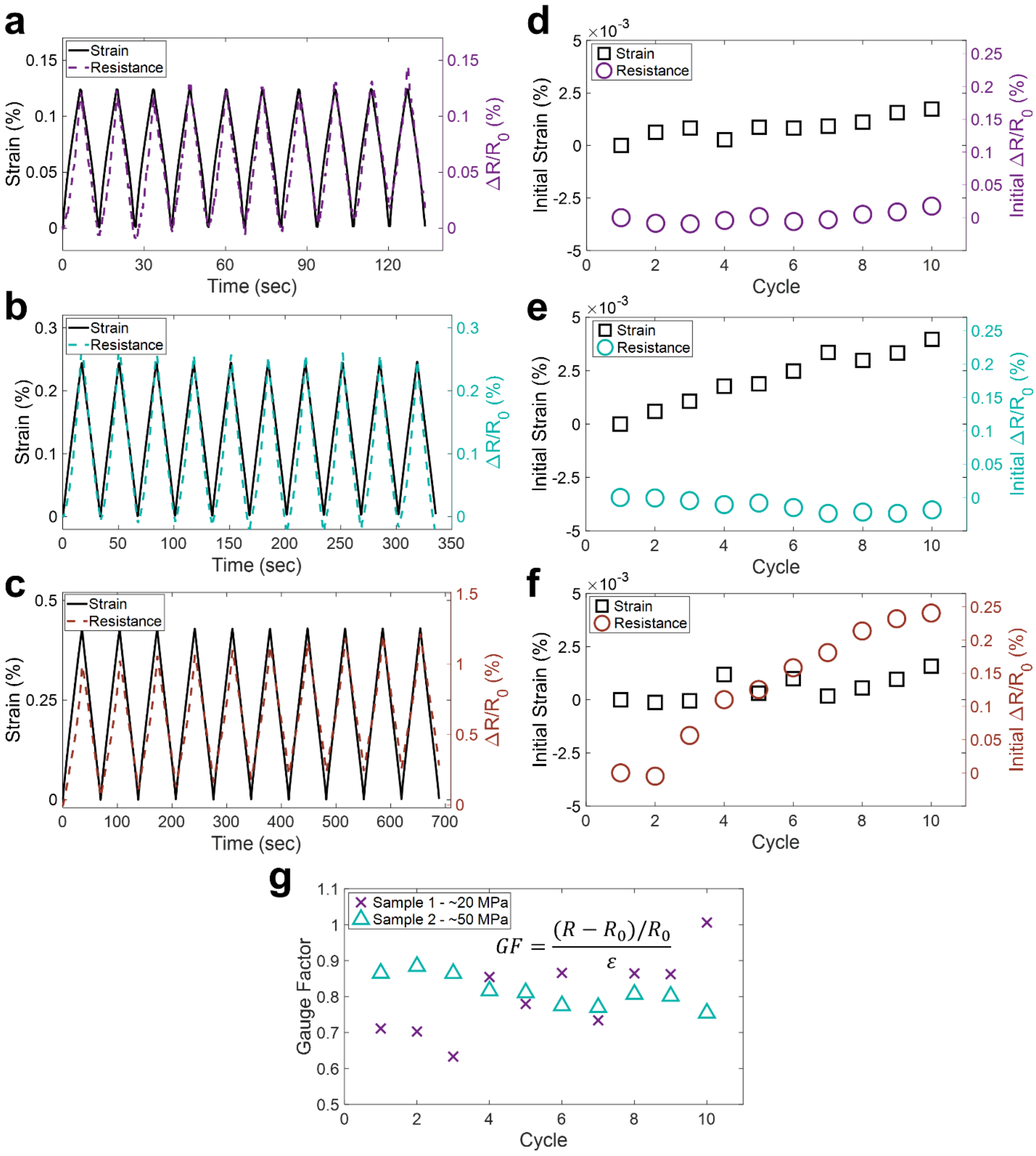

Figure 3.9. (a) Percent strain and percent change in resistance for a sample loaded cyclically to ~20 MPa, (b) percent strain and percent change in resistance for a sample loaded cyclically to ~50 MPa, and (c) percent strain and percent change in resistance for a sample loaded cyclically to ~100 MPa. (d) Initial strain and resistance at the beginning of each cycle for a sample loaded cyclically to ~20 MPa, (e) initial strain and resistance at the beginning of each cycle for a sample loaded cyclically to ~50 MPa, and (f) initial strain and resistance at the beginning of each cycle for a

sample loaded cyclically to ~100 MPa. (g) Gauge factor versus cycle for two undamaged samples and gauge factor equation.

3.3.3. Fiberglass Strain Sensing

Two separate methods of LIG integration were used for strain sensing in fiberglass-reinforced composites: first, a continuous interlayer of LIG covering the full surface of the prepreg similar to the aramid fiber-reinforced composites with LIG, and second, a serpentine patterned LIG strain gauge with controllable dimensions and properties. Each method and the results are discussed in more detail in the following sections.

3.3.3.1. Continuous Laser Induced Graphene Interlayer

To investigate the in-situ strain sensing performance of the fiberglass composites coated with a continuous layer of LIG at low strains, cyclic testing with a maximum stress at approximately 50% of the ultimate strength was completed for the angle ply specimens. It can be noted that one pre-cycle of loading and unloading was used to allow the response to stabilize prior to data collection. The resulting percent change in the electrical resistance of the test specimen in comparison to the percent change in strain as measured by a surface mounted strain gauge are shown in Figure 3.10a. From the figure, the resistance of the sample follows the trend of the strain very closely, showing the ability of the LIG to act as an integrated strain sensor encapsulated within the composite. The gauge factor of the LIG was then calculated for each cycle, the equation for which is shown in Figure 3.9g for reference. The average gauge factor for the fiberglass samples with integrated LIG was found to be 0.38±0.05. The calculated gauge factor is lower than that of the aramid fiber-reinforced composites with LIG as well as the typical value of commercial strain gauges (~2) and alternative methods using embedded CNTs (1.6 – 4.14) [135, 136]; however, the integrated nature of the strain sensing mechanism removes the need for externally bonded sensors, such as commercial strain gauges, and the methodology used here is more scalable than current nanofiller alternatives as discussed previously.

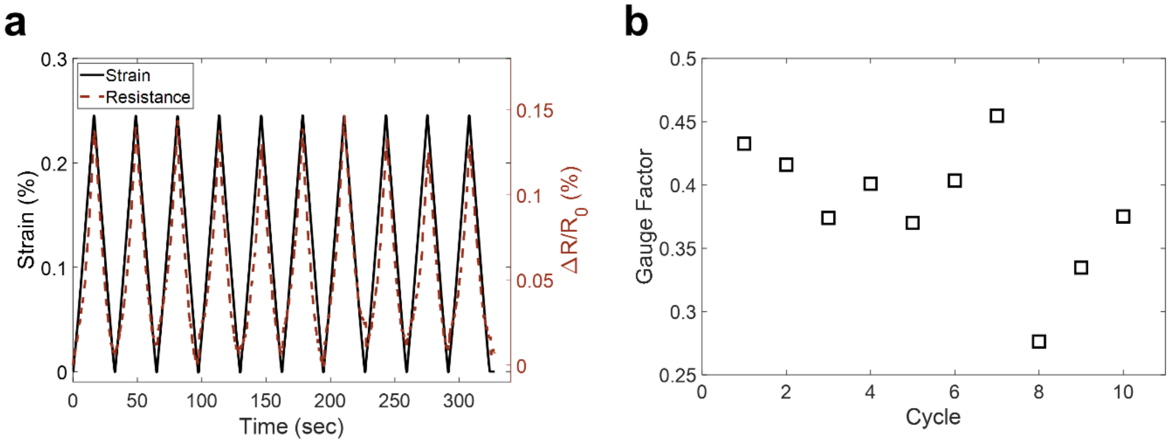

Figure 3.10. (a) Percent strain measured using commercial strain gauge and percent increase in resistance from test specimen with LIG. (b) Gauge factor versus cycle.

3.3.3.2. Serpentine Patterned Laser Induced Graphene Strain Gauge

3.3.3.2.1. Quasi-Static Testing

To investigate the effect of an increased effective LIG length on the gauge factor, serpentine printed LIG strain gauges were also evaluated for quasi-static strain sensing. To assess the response of the serpentine LIG strain gauge during both loading and unloading, corresponding to increasing and decreasing strain, the samples were cycled between zero and 1,200 N which was determined to be well below the threshold at which the composite experienced significant damage. The strain versus applied load for one sample is shown for reference in Figure 3.11a. The experimental results from the commercial strain gauge versus time in comparison to the percent change in resistance of the LIG during the same test are shown in Figure 3.11b. From this representative sample, it can be seen that the LIG shows very little additional noise or signal distortion in comparison to the commercial strain gauge, and instead smoothly transitions from loading to unloading and vice versa. Notably, this minimal noise was observed from each sample regardless of the effective size or final gauge factor of the LIG strain gauge. It can be noted that the LIG results also display no residual change in resistance, and instead show a full recovery within the range tested here. At a microscale, the LIG senses strain by taking advantage of its inherent piezoresistance; as a load is applied and the LIG is positively strained, small microcracks or gaps form within the microstructure of the LIG, resulting in a decrease in conductive contacts and an increase in electrical resistance [116, 117]. As both load and strain are decreased, these microcracks and the conductive pathways are repaired, thus resulting in a repeatable effect [116, 117]. Since little to no mechanical damage or plastic deformation was caused in the host fiberglass structure, no permanent separation within the LIG strain gauge is observed to occur, and the measurements show a full recovery as the load is removed.

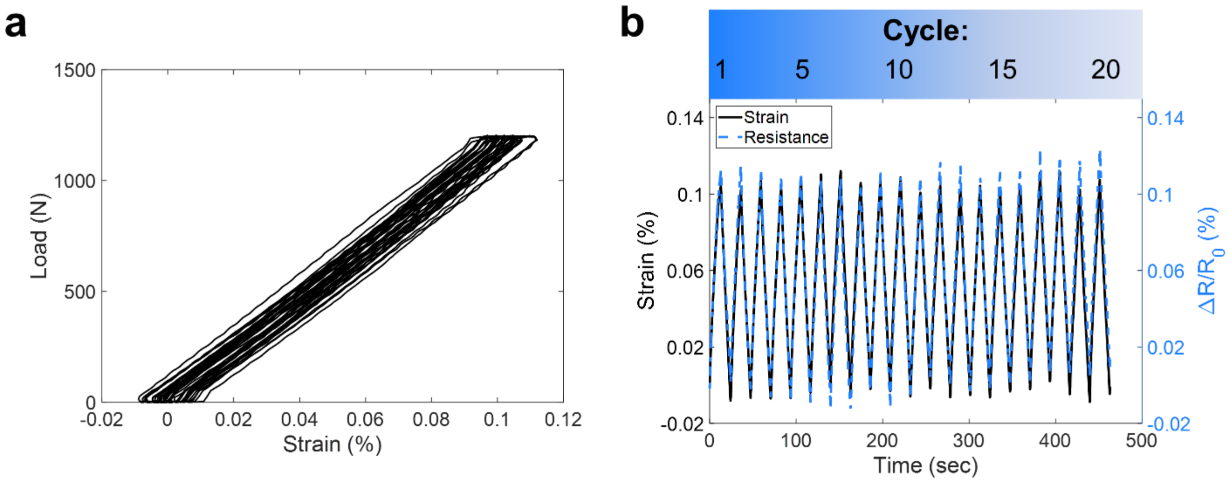

Figure 3.11. (a) Load versus strain for one strain gauge sample. (b) Percent strain and percent change in resistance versus time for quasi-static cyclic loading.

The strain measured by the LIG was calculated based on the gauge factor calculated from the loading portion of each cycle. To accurately calculate a representative gauge factor for each sample, a linear fit between the percent change in resistance and the percent change in strain (determined by the commercial strain gauge) was used for each leg of increasing strain over 20 cycles, and the results were averaged. For reference, the percent change in resistance versus the percent strain for two samples, one with relatively high initial resistance (65 kΩ) and one with relatively low initial resistance (14 kΩ), are shown in Figure 3.12a. The resulting LIG-based strain of the same two samples are compared to the strain from commercial strain gauges in Figure 3.12c and Figure 3.12d. From these representative samples, although the overall error was variant based on each sample, the commercial and LIG strain show very close agreement across most of the applied strain. While the majority of the cyclic loading exhibited negligible error, the points at which the sample transitions from an unloaded to a loaded state and vice versa result in the largest error values. This is anticipated to be due to a slight delay in response as the LIG begins to stretch or compress, resulting in a decrease or increase in carbon-carbon contacts, respectively. In particular, some LIG and commercial strain gauges showed significant misalignment at strain values very close to 0%; however, it should be noted that some of the error between the commercial strain gauge and the LIG measurements can also be attributed to the error of the commercial strain gauge itself. To further characterize the LIG-based strain gauges, the gauge factor of the LIG in comparison to its initial resistance was investigated by examining the trend over several samples with varying initial resistance values. From Figure 3.12b, the average gauge factors of the samples show an increasing trend with initial resistance, which indicates that the gauge factor is tailorable by controlling the initial resistance of the LIG-based strain gauge during the laser printing process. In other words, as additional resistance is added, the sample shows increased sensitivity to strain due to the added degree of separation between conductive contacts. The gauge factor is notably higher than that of the fiberglass samples with a continuous LIG interlayer, yet it is still slightly below that of the commercial strain gauge. However, the LIG strain gauge adds negligible weight and no bulk to the structure, while also eliminating the need for external adhesion and surface requirements, such as limitations on surface roughness or curvature. Therefore, the LIG strain gauge can function as a fully integrated alternative to the commercial strain gauge, removing the need for surface bonding and the relatively extensive processing and preparation required by the commercial strain gauge.

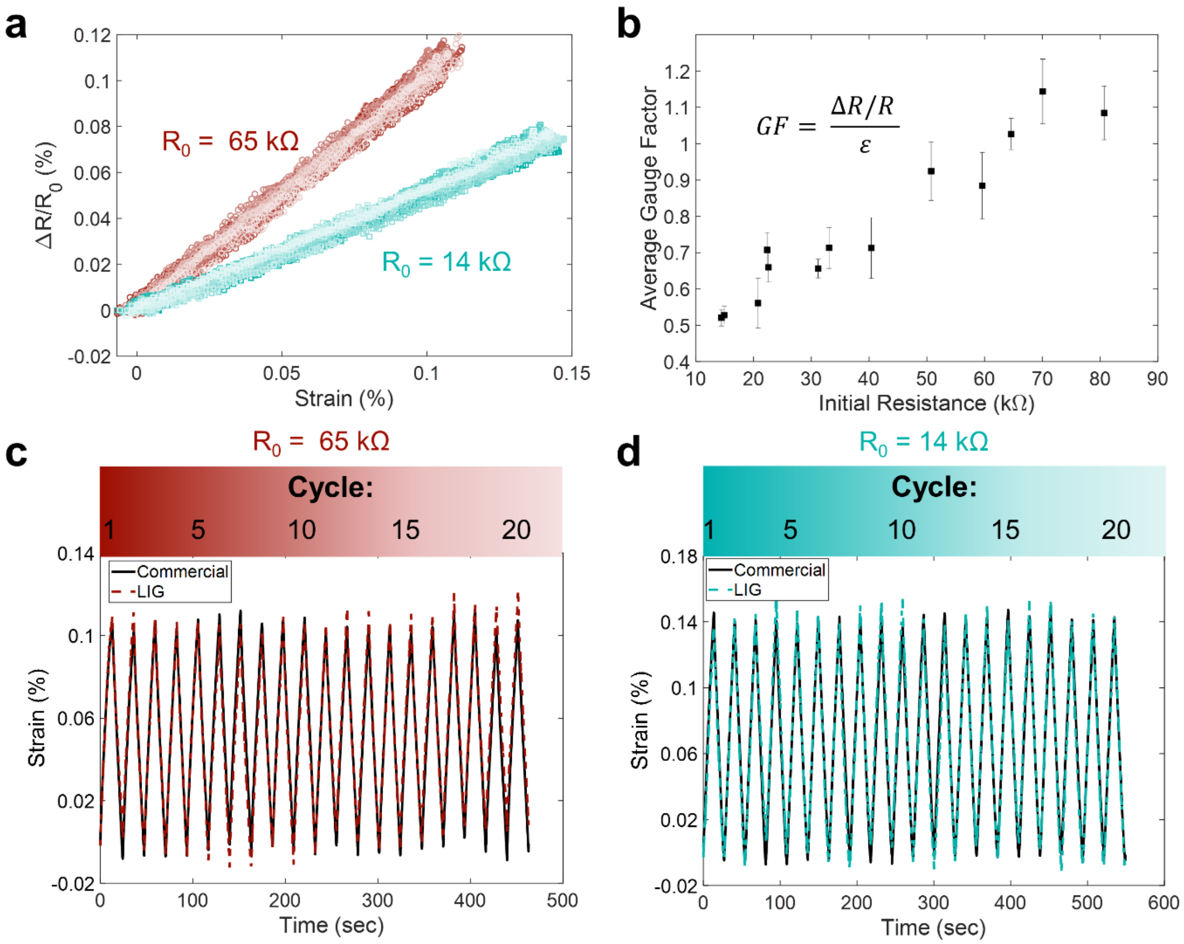

Figure 3.12. (a) Percent change in resistance versus strain for increasing load over 20 cycles for two samples. (b) Gauge factor versus initial resistance. (c) Commercial strain and LIG strain versus time for high resistance sample. (d) Commercial strain and LIG strain versus time for low resistance sample.

3.3.3.2.2. Dynamic Testing

In addition to sensing quasi-static strain, the ability of the LIG strain gauges to measure dynamic strain was also evaluated. To establish their dynamic capabilities, the fiberglass beams with LIG strain gauges were mounted in a cantilever configuration and excited with an impulse using a PCB model 086C03 impact hammer measured through a PCB 482A16 signal conditioner. The frequency response of the sample, using resistance measurements from the LIG strain gauge and the impulse measurement from the impact hammer, was then calculated to determine the natural frequency of the sample. To examine the ability of the samples to track a sine wave at a random frequency away from resonance, the samples were also excited at their base with a sine wave using a Keysight 33500B series waveform generator and Labworks Inc. pa-119 power amplifier in combination with an LDS electromagnetic shaker system. The base acceleration of the sample was measured during excitation using a PCB 352C22 accelerometer in combination with the PCB 482A16 signal conditioner, and during each measurement, the resistance of the sample was again monitored using a Wheatstone bridge in combination with a Transducer Techniques TMO-2 signal conditioner.

Figure 3.13a and Figure 3.13b show the magnitude and phase of the frequency response of the sample resistance from the impulse hammer excitation, respectively. The natural frequency of the sample is clearly detectable from the strong peak in the magnitude which coincides with a 180° phase shift. These results indicate that the resistance measurements from the LIG strain gauge can be used to track the frequency content of the beam for the purpose of material and damage characterization or for the tracking of vibrations experienced by a structure in service. In addition, the sample was excited with a sine wave at a randomly chosen frequency of 165 Hz, which was away from resonance, during which the response of the LIG strain gauge is found to be a sine wave at the same frequency as that of the excitation, as shown in Figure 3.13c. Therefore, the strain gauge is capable of tracking dynamic displacement locally, however it may be noted that a larger strain gauge or a system of printed strain gauges would need to be used in the case of a larger structure. Although this is a similar requirement to more common strain gauge materials, the addition of multiple LIG strain gauges to a composite will result in negligible additional weight and is not limited by surface requirements or size constraints as the LIG is integrated within the material component itself.

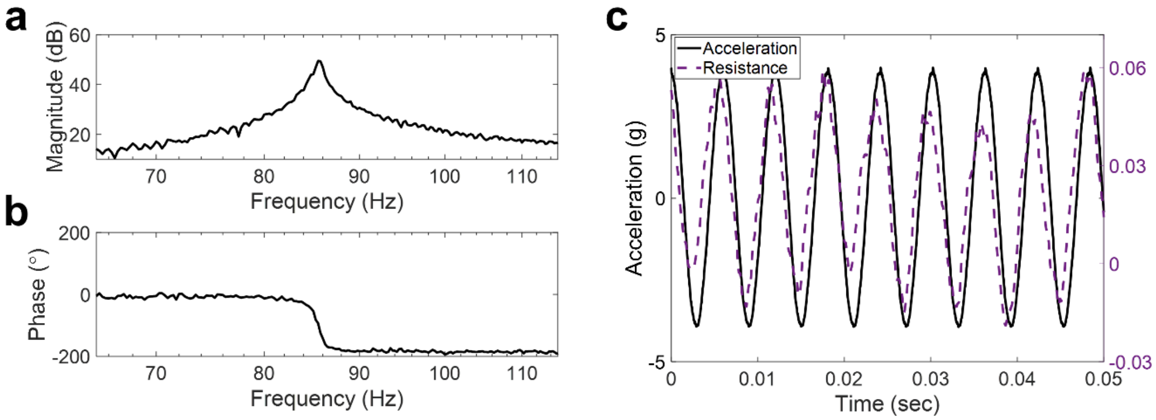

Figure 3.13. (a) Magnitude and (b) phase of the frequency response of the sample resistance to an impulse. (c) Base acceleration and measured resistance of the strain gauge during sine wave excitation.

3.4. Tensile Damage Sensing

Following the characterization of the strain sensing capabilities of both fiberglass and aramid fiber-reinforced samples with LIG, tensile testing to failure was also completed to evaluate the sensing behavior of the samples as they experience damage and approach complete failure. Both aramid and fiberglass composites with continuous LIG interlayers are investigated in this section, however the LIG strain gauges were not tested to failure as the primary purpose of the design was for sensing low magnitude strain.

3.4.1. Experimental Setup

The ability of the LIG-coated aramid samples to sense tensile damage was assessed by testing the specimens in a tensile loading configuration per ASTM standard D3039. A minimum of five samples for both single sided and double sided LIG-coated aramid composites were tested with the plain weave oriented at 0° and 90° from the applied load, and four unidirectional and four angle ply fiberglass samples were tested. The same Instron load frame (Model 5982) described previously with a 100 kN load cell was used at a crosshead speed of 1 mm/min. The resistance of the sample during the test was monitored using the four-point probe method utilizing the four silver paint rings on each sample as contact points (see Figure 3.3f and Figure 3.6a). Throughout the duration of the test, 3 – 4 mA of DC current was applied through the sample with a BK Precision® model 9130 triple output programmable DC power supply using the copper wires connected to the outermost silver paint rings. The resulting voltage across the innermost silver rings from the copper wires was then measured with a NI 4431 data acquisition system (DAQ), and Ohm's law was used to calculate the resistance. An image and schematic of the tensile test setup is shown in Figure 3.14. Due to differences in the fiber composition and composite properties, aramid fiber-reinforced composites tend to exhibit significant plastic deformation followed by fiber failure. In contrast, fiberglass-reinforced composites display relatively sudden instances of damage occurrence such as matrix cracking, delamination, and fiber failure. Thus, for clearer visualization and detection of sudden increases in resistance within the fiberglass-reinforced composites, the second derivative of the percent change in resistance was calculated numerically by taking the numerical gradient of the response with respect to time. Additionally, to confirm the occurrence of damage to the fiberglass composites through acoustic emissions, a high frequency microphone (PCB 426A05) was attached to the test frame close to the sample and was read through a PCB 482A16 signal conditioner which was then connected to the same NI 4431 DAQ. Once again, this microphone was not used during the aramid composite testing, and was only used for the fiberglass composites as the fiberglass composites exhibited a more brittle behavior resulting in measurable acoustic emissions, while the aramid fiber composites exhibit significant plastic deformation due to the polymeric composition of the fibers.

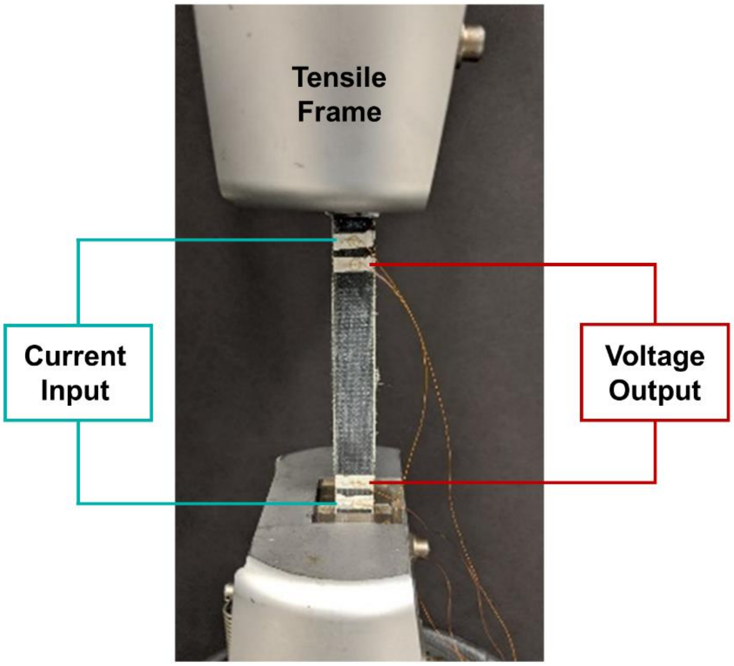

Figure 3.14. Image and schematic of tensile test setup.

3.4.2. Tensile Damage Sensing in Aramid Fiber-Reinforced Composites

The resultant resistance, measured in-situ using the four-point probe method, and the applied load, recorded by the Instron, can be seen for a representative single-sided LIG aramid fiber-reinforced composite in Figure 3.15a. As the single-sided LIG aramid samples were loaded to failure, an increase in the electrical resistance of the sample was observed due to the inherent piezoresistivity of the sample. As tension is applied to the sample, the number of carbon-carbon contacts on each LIG surface is decreased which results in the observed increase in resistance. This effect is approximately linear during elastic deformation, similar to what was seen during quasi-static cyclic loading, and is thus predominantly dictated by the rate of extension. Beyond approximately ~3% increase in resistance correlating to ~25% of the final elongation, the resistance grows nonlinearly as the sample plastically deforms. During this region of tensile loading, irreversible separation between the LIG is observed. Additionally, as sudden damage occurs to the sample, either as delamination or as fiber breakage, the rate of increase in resistance changes due to a sudden separation of the conductive pathways on the LIG located on the surface fibers of each ply. This effect is particularly evident toward the latter portion of the test. It should also be noted that the sudden drop in resistance observed at complete tensile failure of the sample is due to the wire leads suddenly breaking off, and is not due to a change in the resistance of the sample.

Similar to the single-sided LIG aramid samples, the double-sided samples also show an increasing trend in resistance with applied load and strain as can be seen in Figure 3.15b. As before, there is a roughly linear increase during the first ~20% of the test which corresponds approximately to the elastic region of the material, after which, as the sample transitions to plastic deformation, the percent increase in resistance increases nonlinearly. Due to the higher graphene content and the decreased fiber volume resulting from the laser treatment process of the double-sided samples, fiber failure may be less likely to cause a sudden increase in resistance as was evident in the single-sided samples. As has been discussed previously, the exterior fibers in each tow, which are exposed to the laser, are irradiated and converted to piezoresistive LIG. As the sample is loaded, the interior fabric, not converted to LIG, decreases in cross-sectional area due to Poison's deformation, resulting in increased conductivity from the LIG coating. Therefore, as the fiber reinforcement begins to fail, there is little separation between the carbon contacts and the failure is thus not detectable via sudden increase in resistance in the double-sided LIG samples. It is interesting to note that although the double-sided LIG samples are more conductive than the single-sided samples, the maximum percent increase observed during tensile testing is similar to that seen from the single-sided samples which have a much higher initial resistance. In addition to evaluating the piezoresistive response of the composite samples in tension, compression was also applied to single-sided samples for an improved understanding of the response of the LIG coating. Figure 3.15c shows the applied load and percent change in resistance versus the strain of the composite taken from compression to the point of buckling. The response indicates that compression of the sample results in increased conductivity which is a result of additional conductive contacts within the LIG. Therefore, the composites containing LIG are shown to sense both tension and compression through an increase or decrease in electrical resistance, respectively.

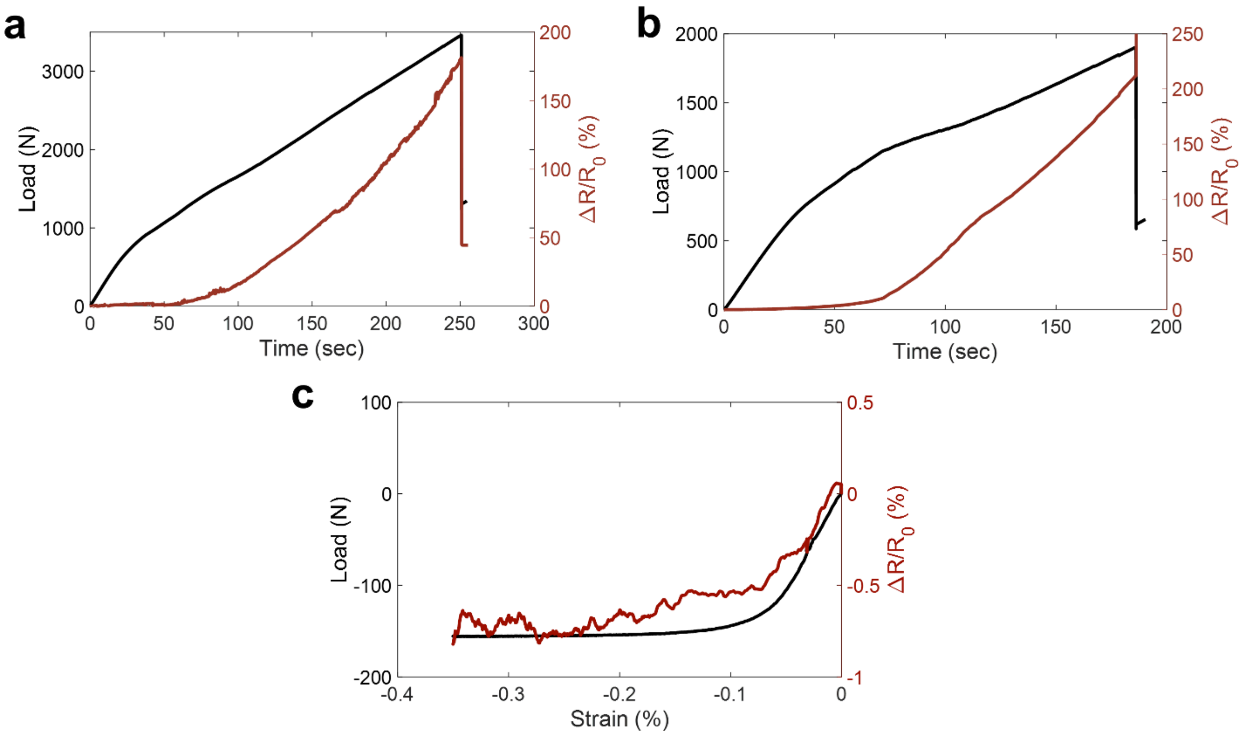

Figure 3.15. Load and percent change in resistance versus time for (a) a single-sided LIG aramid sample under tension and (b) a double-sided LIG aramid sample under tension. (c) Load and percent change in resistance versus strain for a single-sided LIG aramid sample under compression.

3.4.3. Tensile Damage Sensing in Fiberglass-Reinforced Composites

The fiberglass-reinforced samples were also loaded in a tensile configuration following the same methodology used for the aramid fiber-reinforced composites. Since the fiberglass reinforcement exhibits more brittle behavior rather than the plastic deformation exhibited by the aramid fiber composites, the second derivative of the resistance measurements, calculated numerically, was also considered for greater visualization of sudden resistance changes. Furthermore, as was stated in Section 3.4.1, a high frequency microphone was employed to detect acoustic emissions. The resulting applied load, percent change in resistance, second derivative of the percent change in resistance, and acoustic emission response from the microphone for a representative unidirectional test specimen is shown in Figures 3.16a – d respectively, and similar measurements for an angle ply test specimen are shown in Figures 3.16g – j. For reference, the initial resistances of the angle ply test specimens were between approximately 300 and 1,000 Ω while the initial resistances of the unidirectional specimens were between approximately 150 and 300 Ω. As a result of the piezoresistivity of the LIG interlayers in both samples, the electrical resistance and its second derivative show clear and distinct jumps, which are inversely proportional to sudden decreases in the applied load and correlate to detected acoustic emissions from the microphone. This is more clearly shown in the magnified sections of the second derivative and acoustic emission reading from the microphone shown in Figures 3.16e – f for the unidirectional specimen and Figures 3. 16k – l for the angle ply specimen. The combination of each of these measurements indicate significant damage to the specimens such as fiber failure or delamination as the samples near catastrophic failure. As each sample delaminates, the conductivity between LIG layers decreases as some of the carbon-carbon contacts are broken, resulting in an increase in measured resistance. Fiber failure also results in an irreversible increase in resistance as the LIG at each interface separates with the physical separation of the fiber and the surrounding matrix. The increase in resistance is proportional to the acoustic emissions indicating that the methods are comparable in their damage detection capabilities. However, as confirmed by the cyclic testing in Figure 3.10 which is discussed further in Section 3.3.3, prior to significant damage as detected by the decreasing load and acoustic emissions from the microphone, the resistance of the sample increases approximately linearly due to the piezoresistive nature of the LIG interlayer. Specifically, as the sample is strained, the carbon-carbon contacts in the LIG coating separate, resulting in the observed increase in resistance correlating to the increasing stress and strain. It should be noted that the sudden decrease in resistance observed at failure from the unidirectional test specimen in Figure 3.16e is an artifact from the electronic measurement as the wire disconnected from the sample at catastrophic failure.

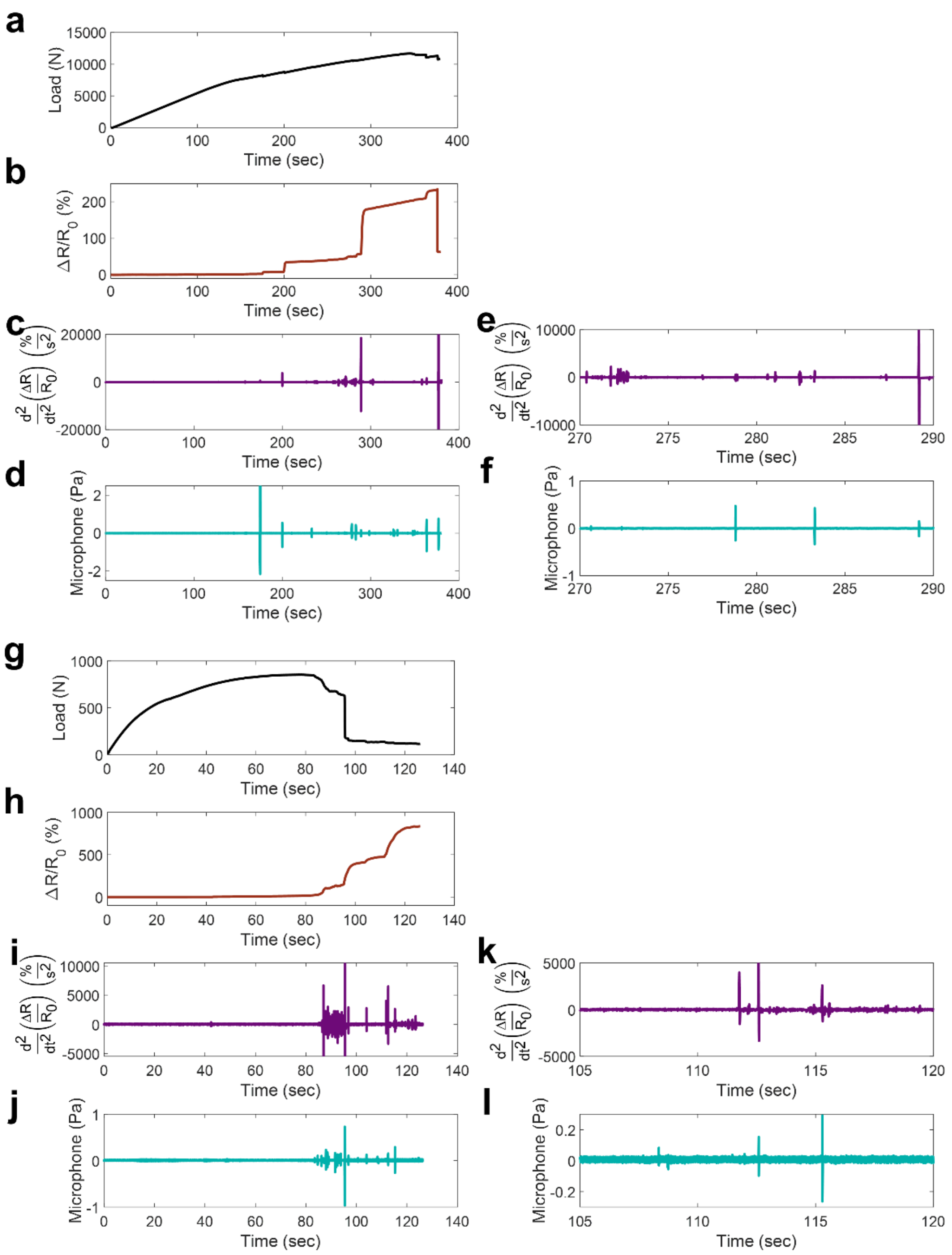

Figure 3.16. (a) Applied load, (b) percent change in resistance, (c) second derivative of the percent change in resistance, and (d) microphone reading for a unidirectional composite specimen with LIG under tensile loading. Magnified portion of the (e) second derivative of the percent change in resistance and (f) acoustic emission reading from the microphone for the same unidirectional specimen. (g) Applied load, (h) percent change in resistance, (i) second derivative of the percent change in resistance, and (j) microphone reading for an angle ply composite specimen with LIG under tensile loading. Magnified portion of the (e) second derivative of the percent change in resistance and (f) acoustic emission reading from the microphone for the same angle ply specimen.

3.5. Laser Induced Graphene for Flexural Damage Sensing

3.5.1. Experimental Setup

In addition to sensing tensile strain, the ability of the composites to sense flexural strain was evaluated by testing the prepared sample beams in a three-point bend configuration per ASTM standard D7264 with a span to thickness ratio of 20:1 for the aramid fiber composites, to generate high strain levels, and 32:1 for the fiberglass composites. To test the fiberglass response, an angle ply composite (three plies) was cut to beams of dimensions ~13 mm wide by ~76 mm long as specified by ASTM standard D7264 for three-point bend. Additionally, single- and double-sided aramid composites of approximately the same dimensions were also tested. The same universal Instron load frame (Model 5982) and 100 kN load cell were used at a crosshead speed of 1 mm/min, and a minimum of five aramid and five fiberglass samples were tested. To eliminate current transfer from the sample to the load frame, non-conductive Kapton® tape was placed on the surface of the three-point bend pins. Throughout the duration of the test, 3 – 4 mA of DC current was again applied through the sample using the same DC power supply employed during the tensile test with the copper wires connected to the outermost silver paint rings, and the resulting voltage across the innermost silver rings from the copper wires was then measured with the NI 4431 DAQ. The resistance of each sample during the test was calculated afterward using Ohm's law. An image of the test setup can be seen in Figure 3.17a. Similar to the tensile tests, a high frequency microphone (PCB 426A05) was attached to the test frame close to the sample during the fiberglass testing to confirm damage through acoustic emissions, and was read through a PCB 482A16 signal conditioner which was then connected to the NI 4431 DAQ. Due to the fact that the LIG coatings are located on the surface of only one side of each fiberglass prepreg layer and the single-sided aramid samples, the samples are inherently asymmetric and the LIG surfaces are primarily in compression (LIG surfaces facing up) or tension (LIG surfaces facing down) as illustrated in Figure 3.17b and Figure 3.17c, respectively. For this reason, multiple three-point bend samples were tested in each configuration to establish differences in sensing potential during compression and tension. The double-sided aramid composites, which were symmetric, were also tested to establish differences in the sensing potential.

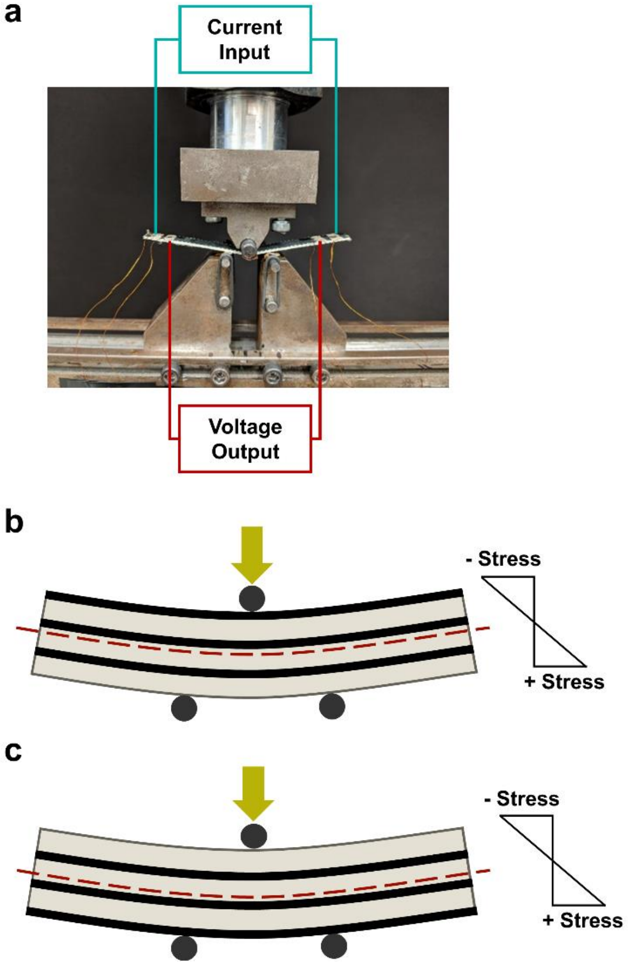

Figure 3.17. (a) Image and schematic of three-point bend test setup. Schematic of three-point bend configuration with LIG surfaces primarily under (b) compression and (c) tension.

3.5.2. Flexural Damage Sensing in Aramid Composites

An analysis of the load and resistance measurements taken during three-point bend testing of aramid samples with different configurations provides insight into the strain sensing mechanism of the LIG coated aramid samples. As previously stated, the single-sided samples are inherently asymmetric in layup due to the added LIG layers, thus resulting in the majority of the LIG surfaces being either under compression or under tension during flexural loading depending on the orientation of the sample. Figure 3.17b – c shows a schematic of the single-sided LIG coated aramid samples in both orientations during flexural loading and the associated midline. It should be noted that the LIG surfaces are separated by untreated Kevlar® fabric as only the exterior fibers of each tow are converted to LIG as discussed in Section 2.1. If the sample is oriented such that the LIG surfaces are facing upward during flexural loading (Figure 3.17b), the majority of the sensing surfaces are under compression. In contrast, if the sample is oriented such that the LIG surfaces are facing downward during loading, the majority of the sensing surfaces are under tension (Figure 3.17c). Thus, the two effects can be individually investigated during flexural loading by changing the orientation of the composite test specimen.

Figure 3.18a shows the percent increase in resistance of a sample with the LIG surfaces oriented toward the bottom of the sample or primarily under tension. From the figure, when the majority of the LIG surfaces are experiencing positive strain, little to no linear increase is seen while the sample is elastically deformed (~10 – 15% of the final stress). This is likely due to the simultaneous separation between electrical carbon contacts on the intact LIG surfaces and the transverse compression of the LIG surfaces, which results in increased carbon-carbon contacts within the LIG microfiber bundles and thus increased conductivity. As the sample continues to deform beyond the first 1% strain, accumulated damage and plastic deformation causes the resistance to increase non-linearly as a result of drastically reduced conductive contacts on each LIG surface in tension. In the case of tension, the carbon-carbon contacts on each LIG surface are reduced or eliminated due to increased distance between each microstructure. In contrast, Figure 3.18b shows the behavior of the sample when the majority of the LIG surfaces are primarily under compression. In the case of compression, the electrical resistance of the sample shows an initial decrease in resistance during the first ~40% of the test. This is attributed to both the compression of the LIG surfaces in the top half of the asymmetric composite which creates additional transverse contact between lamina, as well as additional carbon-carbon contacts on each LIG surface resulting in decreased electrical resistance. During the final 60% of the test, the response of the lamina in tension overtake the compressive effects, due to the large amount of separation between the LIG contacts, consequently resulting in increased electrical resistance with plastic deformation. However, the overall percent increase in resistance does not exceed 1.5% in contrast to the 6% increase observed from the previous configuration that was tension dominant.

For comparison, the applied load and resulting composite resistance versus time of the double-sided LIG coated aramid composite is provided in Figure 3.18c. In contrast to the single-sided LIG samples, the symmetric double-sided LIG samples show very small changes in resistance during flexural testing. This is due to the cancellation of the piezoresistive effects of the LIG while under compression and tension. Similar to the single-sided samples with LIG facing up (primarily under compression), the double-sided samples show some small initial decrease in resistance at the beginning of flexural loading. As previously discussed, transverse compression of the sample leads to increased contact and conductive pathways as a result of the compression of the LIG surfaces which results in increased conductivity. As the flexural strain increases, the tensile effects slightly overcome the compressive effects leading to an increase in resistance, however the response is not as significant as that seen from the single-sided samples. This may indicate that the increased conductivity of the double-sided samples and the functionality of the two LIG surfaces acting as resistors in parallel reduces the sensing capacity when a portion of the LIG surfaces are under tension. Effectively, the two results experienced separately by the single-sided LIG samples occur simultaneously in the double-sided samples due to the symmetry of the composite beam. Therefore, the outcome is a cancellation between increasing and decreasing conductivity as is evidenced by the minimal changes observed in the measured resistance (less than 1% increase or decrease in resistance).

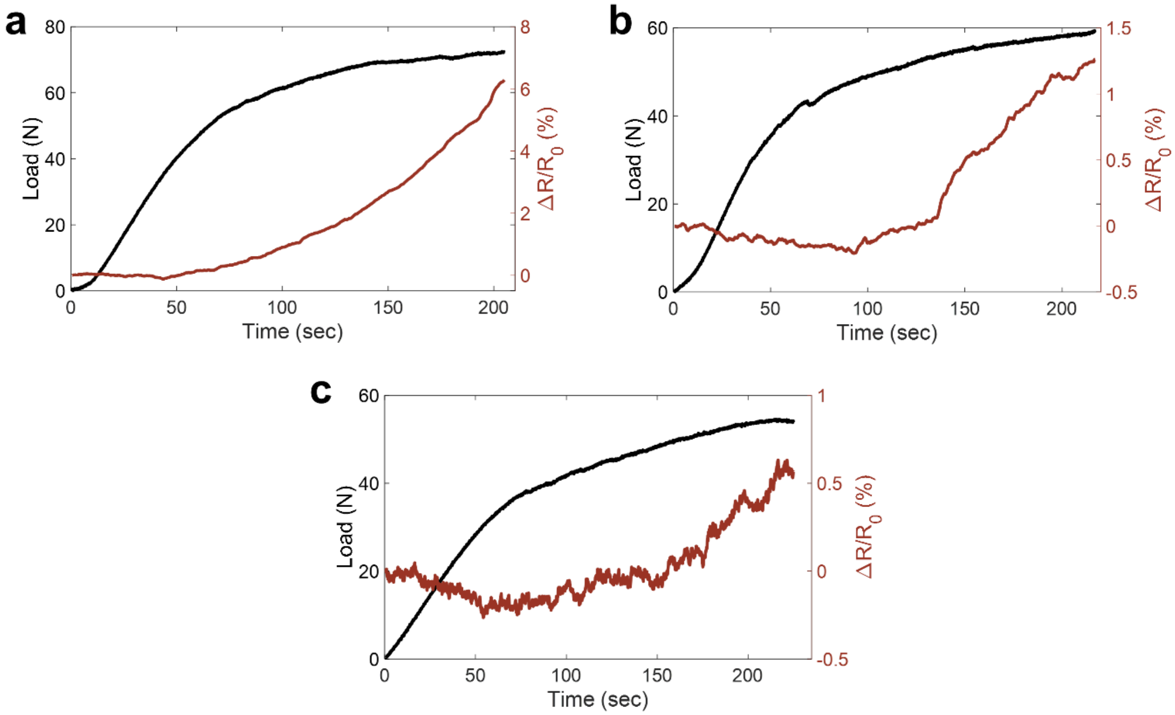

Figure 3.18. Load and percent change in resistance versus time during three-point bend for (a) a single-sided LIG aramid sample with the LIG under tension, (b) a single-sided LIG aramid sample with the LIG under compression, and (c) a double-sided LIG aramid sample.

3.5.3. Flexural Damage Sensing in Fiberglass-Reinforced Composites

To determine the ability of the LIG interlayer to sense flexural loading in fiberglass composites, the samples were again tested by means of three-point bend in two configurations: the LIG surfaces facing toward the top of the sample and the LIG surfaces facing toward the bottom of the sample. The results of the flexural bending tests for a representative sample in the compression and tension configurations can be seen in Figures 3.19a – d and Figures 3.19g – j, respectively, and Figures 3.19e – f and Figures 3.19k – l show the second derivative of the percent change in resistance and acoustic emission reading from the microphone at higher magnification during the latter portion of the test for the compression and tension configurations, respectively. Both sets of figures clearly show sudden and dramatic increases in electrical resistance with the occurrence of damage toward the end of the test as the sample approaches catastrophic failure as seen in both the resistance measurements as well as the second derivative of the percent change in resistance. These increases in resistance also correlate to sudden drops in load and acoustic emissions detected using the high frequency microphone, thus confirming the occurrence of damage. This indicates that as sudden delamination or fiber fracture occur, the carbon-carbon contacts comprising the LIG surfaces are separated, thus increasing the resistance and resulting in a corresponding acoustic emission which is detected by the high frequency microphone. However, the percent increase in resistance correlated with damage was observed to be different between the samples in the compression configuration versus the samples in the tension configuration since more LIG surfaces experienced separation between the conductive carbon-carbon contacts with additional layers under tension, and the cumulative amount of separation was larger when the LIG layer was located at the point of maximum strain at the bottom of the sample. The total percent increase in resistance of the composite in the tension configuration was thus observed to be significantly higher than that under compression. In addition, the ability of the samples to track low levels of flexural strain was also different between the samples under primary compression and the samples under primary tension. As LIG-coated samples are compressed, a small amount of additional conductive carbon contacts are formed in each LIG interlayer, resulting in increased conductivity and a decrease in the measured resistance. In the case of a flexural sample, transverse compression and decreased resistance happens simultaneously to the separation of carbon contacts in the LIG interlayers under tension, resulting in cancellation between the two effects and a lower magnitude change in resistance compared to the sample experiencing primary tension in the LIG interlayers. Therefore, samples in both configurations are capable of detecting damage and sensing strain, however, the degree to which they are able to sense flexural strain is dependent on the orientation of the LIG interlayers.

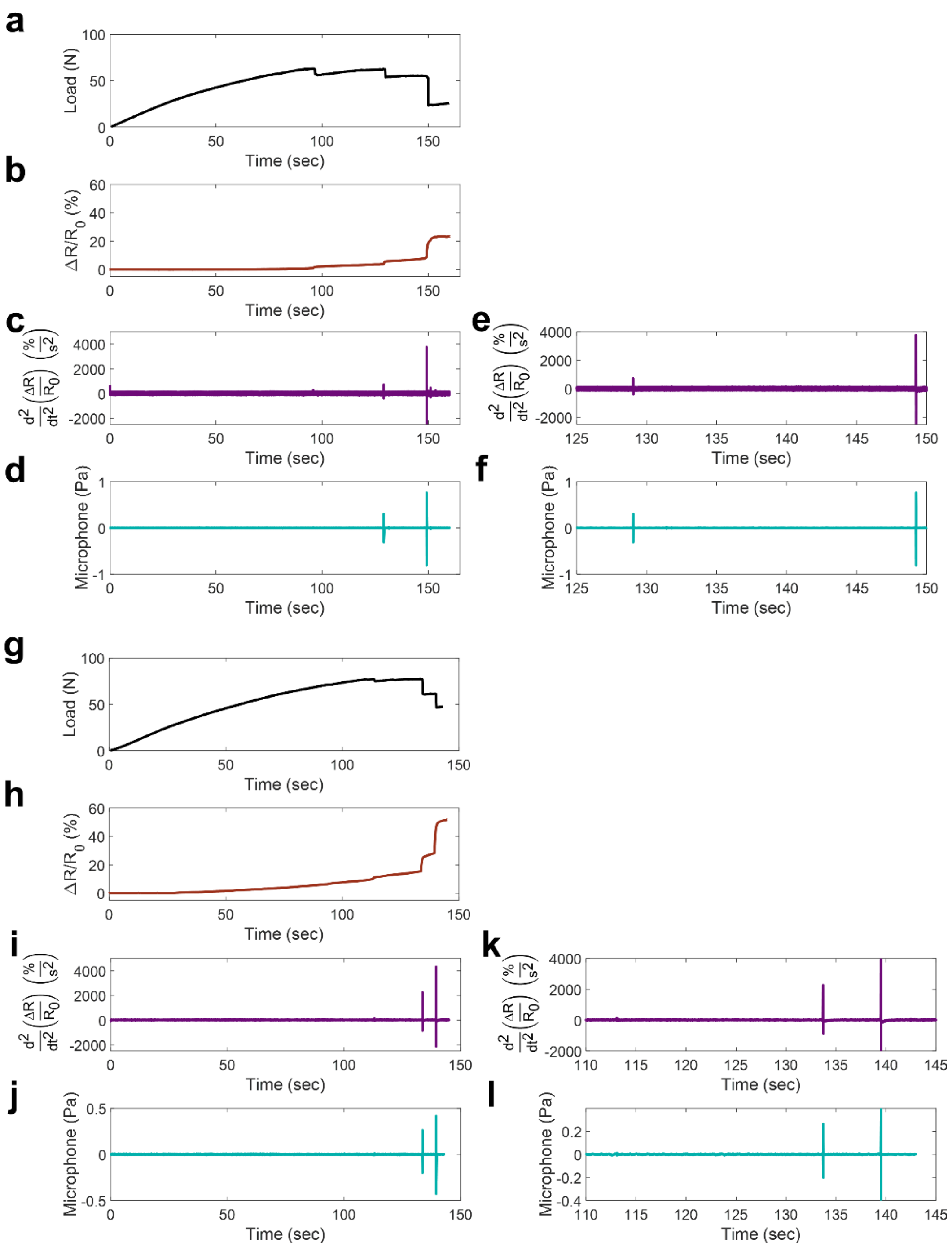

Figure 3.19. (a) Load, (b) percent change in resistance, (c) second derivative of the percent change in resistance, and (d) microphone pressure for three-point bend specimen with LIG primarily under compression. (e) Load, (f) percent change in resistance, (g) second derivative of the percent change in resistance, and (h) microphone pressure for three-point bend specimen with LIG primarily under tension.

3.6. Chapter Summary

This chapter establishes the use of multifunctional LIG interlayers for in-situ monitoring of strain and damage in fiberglass- and aramid-reinforced composites. The processes used to achieve this in composites fabricated from both types of fiber reinforcement are both low-cost and scalable which is promising for future applications and large-scale production. In the case of the aramid fiber reinforcement, the microstructured LIG surfaces are directly printed onto woven aramid fabrics using a laser irradiation process. To the same end, the LIG is transfer printed on commercial fiberglass prepreg which also results in a similar piezoresistive interlayer. The piezoresistive sensing abilities of the composites containing LIG were then established during flexural loading, tensile loading, and quasi-static cyclic tensile loading during which the LIG proves capable of tracking both strain and detecting damage in-situ using common resistance monitoring methods. Additionally, transfer printed LIG strain gauges integrated within fiberglass prepreg composites were shown to exhibit multiple tailorable properties including size, location, and gauge factor which ranged from approximately 0.5 to 1.2. The LIG strain gauges are also shown to be capable of sensing both quasi-static and dynamic strain in-situ. Thus, in each case presented in this chapter, any need for external sensors is removed. Moreover, the techniques presented here are highly scalable and automatable relative to the current methods adopted to introduce piezoresistivity in fiberglass- or aramid-reinforced composites. The result of this work is thus promising multifunctional materials with applications in dynamic and unpredictable loading conditions where in-situ tracking and damage detection is of benefit.

CHAPTER 4

Damage Localization in Fiberglass Composites using Laser Induced Graphene

4.1. Chapter Introduction

The focus of Chapter 4 is the application of the simple and scalable laser induced graphene (LIG) process to coat electrically insulating commercial fiberglass prepreg with piezoresistive LIG for the localization of damage. To accomplish this, the LIG is transfer printed onto commercial fiberglass prepreg using the same methods described in Chapter 3, and is subsequently used to localize damage in all three dimensions of the resultant fiberglass-reinforced composites. A combination of in-situ and ex-situ resistance measurements are used to accomplish this objective. First, in-situ measurements are used to determine the relative location of damage in one-dimension under tensile loading. Subsequently, separate in-situ measurements are used to locate damage through the thickness under flexural loading. Finally, ex-situ methods are used to calculate the two-dimensional location of a hole in a plate. Therefore, this work presents a self-sensing structural material capable of locating damage in all three-dimensions using commercial materials and simple damage detection methodology.

4.2. Sample Preparation and Composite Layup

The methodology used for the composite fabrication in this chapter follows similar processes to those discussed in Section 3.2.2.1, where the LIG was coated onto the surface of the fiberglass prepreg using a two-step transfer printing process. First, commercial polyimide tape (2 mil (0.0254 mm) thick Kapton®) was irradiated using a 40 W CO_2 laser (Epilog Zing 16 universal laser system). It should be noted that the polyimide tape acts as a precursor for the LIG, thus requiring no additional graphene source [111]. The LIG microstructure can be varied by adjusting the power and pulsing density of the laser, which determine the conductivity of the LIG as well as the transferability of the LIG microstructure onto the tacky prepreg surface. To ensure clean transfer and sufficient prepreg conductivity, 14% power and 400 dots per inch (DPI) were used for the purpose of this work. Following the laser treatment, the LIG was transferred to the surface of the fiberglass prepreg (CYCOM® E773 epoxy prepreg with S-2 glass fiber-reinforced roving) using a constant pressure rolling process, during which the LIG was removed from the polyimide tape. To assist in the transfer process, the prepregs were slightly heated to a temperature of 80 °C, which increases the adhesion between the matrix of the prepreg and the LIG microstructure. Following the transfer of the LIG from the polyimide tape to the surface of the prepreg, a hot press was used to combine the LIG-coated prepregs under vacuum at 121 °C and 100 psi (689.5 kPa) for two hours. The described method was used to fabricate three separate composite plates for tensile testing, three-point bend testing, and two-dimensional damage localization. The composites for both tensile and flexural loading were comprised of three plies of fiberglass prepreg stacked at [+45/-45/+45]° (Figure 4.1a and Figure 4.1b), while the composites used for two-dimensional localization were made up of two plies of fiberglass prepreg stacked at [0/90]° and (Figure 4.1c). To allow for wire leads to be attached to each ply in the three-point bend composite, the lengths of each ply were staggered as shown in Figure 4.1a. Once each set of composites was fully cured, the samples were cut to the desired size, and wire leads (33-gauge copper wire) were attached directly to the LIG surface using a combination of silver paint and epoxy (Loctite® Epoxy Instant Mix™ 5 Minute).

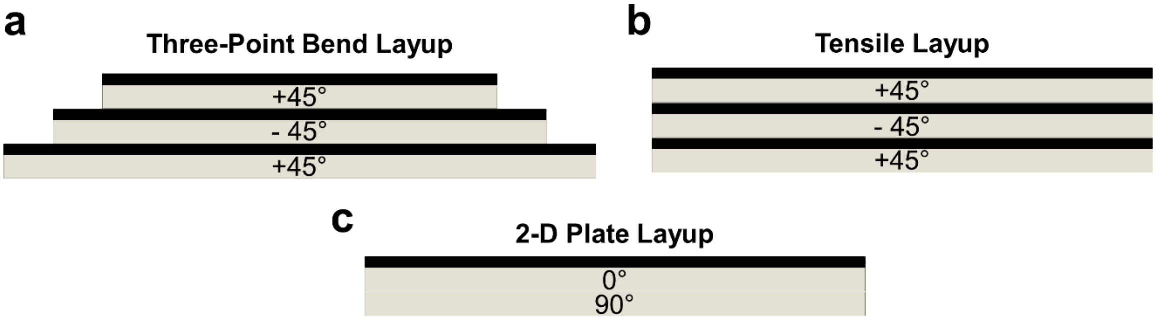

Figure 4.1. (a) Schematic of LIG process on polyimide substrate. (b) Schematic of LIG transfer process onto fiberglass prepreg. (c) Stacking sequences of final composites for respective mechanical testing.

4.3. One-Dimensional Localization during Tensile Testing

4.3.1. Experimental Method and Testing Setup

The in-situ localization of composite failure under tension was evaluated by loading the previously described tensile specimens in a tensile test per ASTM standard D3039. Prior to testing, each sample was cut to dimensions of 15.24 – 19 mm in width and 125 mm in length, and silver paint was used to divide the specimen length into four quadrants with two additional silver paint lines at each end for current to be applied along the length of the specimen (Figure 4.2). Using the outermost silver paint lines, 5 mA of direct current was applied through the length of the composite using a BK Precision® model 9130 triple programmable DC power supply throughout the duration of the test. The resultant voltage across each of the four quadrants was simultaneously measured using a NI 4431 data acquisition system (DAQ). To predetermine the location of the majority of the damage within the sample and the resultant ultimate failure, small notches were cut into the sides of the sample in only one quadrant. It can be noted that additional width was added beyond

15.24 mm to allow for the small slits to be cut into each side of the composite, and fiberglass tabs were added to each end of the sample for tensile testing using high shear strength epoxy (Loctite® EA 9430™ Hysol®). A schematic of a tensile test sample with damage initiated in Quadrant 1 can be seen in Figure 4.2.

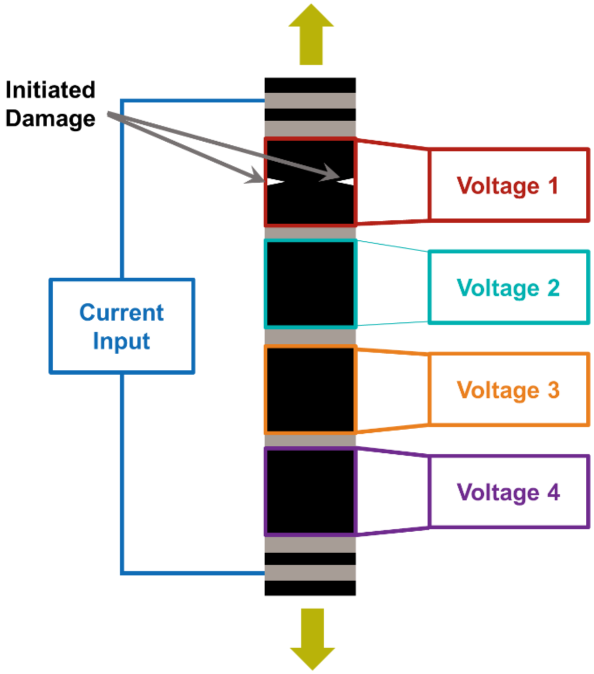

Figure 4.2. Schematic of current application and voltage measurements during tensile test.

4.3.2. One-Dimensional Localization Results

The results for a representative sample are shown in Figure 4.3a – e which correlate to the applied load and percent change in resistance for all four quadrants, respectively, of a sample with damage initiated in the first quadrant. Since the conductivity of the LIG interlayer can have an effect on the sensing ability, it is worthwhile to note that prior to testing, each quadrant had an initial resistance between approximately 115 – 250 Ω, and the quadrant with the damage initiation did not show a significantly different initial resistance in comparison to the other quadrants. From

Figure 4.3b, the final percent increase in electrical resistance in the damaged quadrant is greater than 900%, while the relatively undamaged quadrants show only a small change at catastrophic failure. The significant change in the damaged quadrant is attributed to the complete separation between the positive and negative current connections at failure due to crack propagation. Prior to catastrophic failure, Quadrant 1 also shows a higher rate of increasing resistance relative to the other three quadrants as a result of the propagating damage and increased strain due to the initial slits cut into the sides of the sample. This measured increase in resistance is a result of the increased separation between conductive contacts in the LIG interlayer within the specimen. As the sample is strained, the fibrous LIG decreases in conductivity as a result of the inherent piezoresistivity, while permanent separations, due to the physical separation in the LIG interlayers, result from delamination and fiber failure. Since this occurs predominantly in Quadrant 1 due to the pre-damage, this is the location of the most significant change in measured resistance.

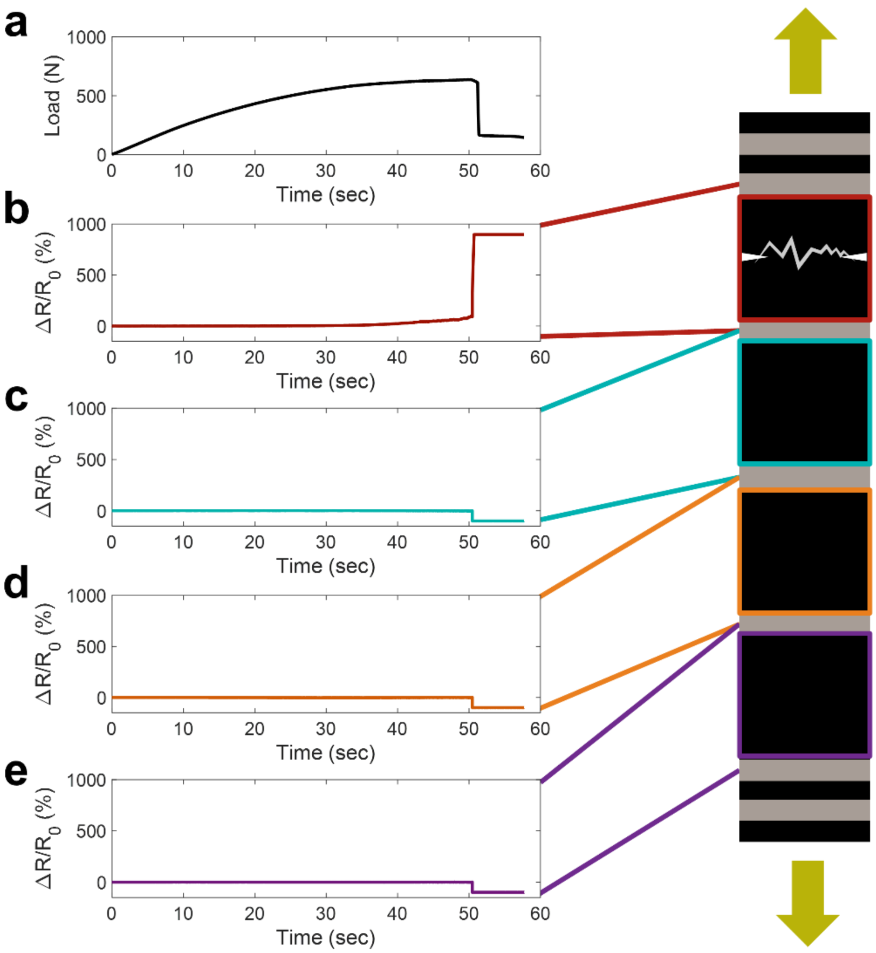

Figure 4.3. (a) Load, (b) percent change in resistance in first quadrant, (c) percent change in resistance in second quadrant, (d) percent change in resistance in third quadrant, and (d) percent change in resistance in fourth quadrant for tensile sample that broke in the first quadrant.

As an alternative example, the sample represented by the schematic and data in Figure 4.4a – e had damage initiated in the fourth quadrant. Similar to the previous sample, the three relatively undamaged quadrants show a negligible changes in electrical resistance while the fourth quadrant, which experienced significant damage and strain, showed a significantly higher increase in resistance with the final value reaching almost 400%. Once again, significant damage resulted in the physical separation of the conductive carbon-carbon contacts within the LIG interlayer leading to the observed increase in resistance. Although the specific value is lower than that of the previously discussed example, the relative increase exceeds any reasonable threshold indicating significant damage, thus signifying that the physical separation within the piezoresistive LIG interlayers is far greater in the damaged quadrant. Therefore, the samples with LIG are conclusively able to provide information which enables the in-situ determination of the damage location in one-dimension. It can be noted that if additional linear resolution were needed for a specific application, increasing the spatial frequency of the measurements along the length of the sample would provide improved dimensional accuracy when localizing damage.

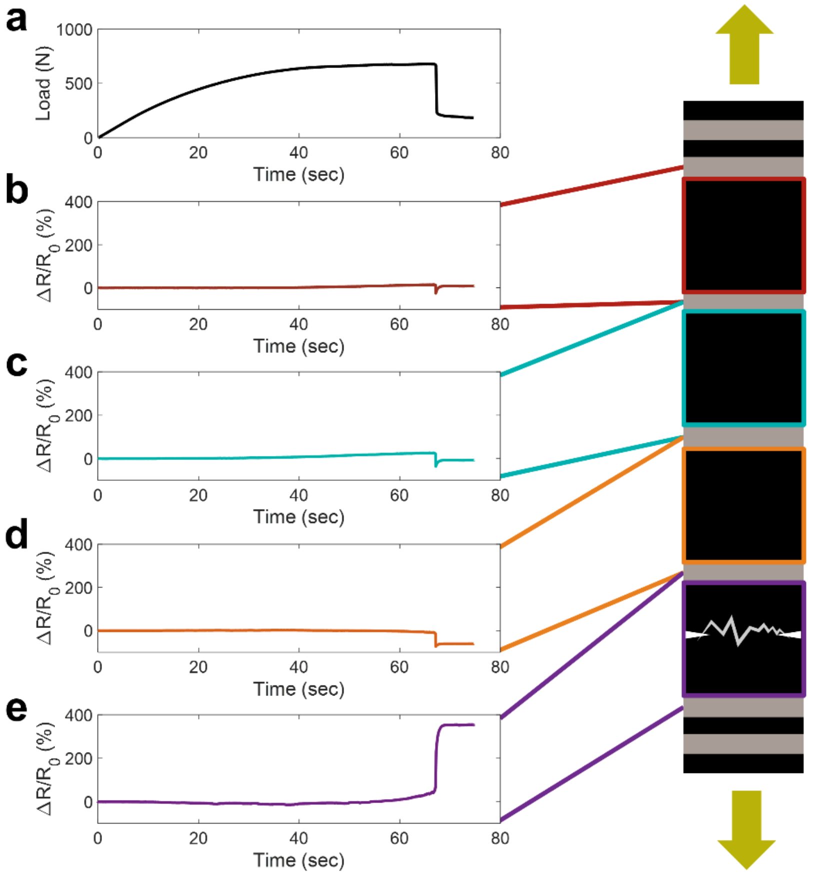

Figure 4.4. (a) Load, (b) percent change in resistance in first quadrant, (c) percent change in resistance in second quadrant, (d) percent change in resistance in third quadrant, and (e) percent change in resistance in fourth quadrant for tensile sample that broke in the fourth quadrant.

4.4. Through-Thickness Localization during Three-Point Bend Testing

4.4.1. Experimental Methods and Test Setup

In addition to in-situ tensile localization, in-situ localization of fracture and interply delamination through the thickness of the composite was evaluated using mechanical testing via flexural loading in a three-point bend configuration. The three-point bend samples were designed in such a manner that the ply lengths were staggered in order to easily attach the wire leads to both ends of each individual ply as illustrated in Figure 4.5a and Figure 4.5b. To reduce the electrical conductivity between the three LIG interlayers and ensure each measurement accurately reflected the intended ply, a small amount of additional quick-cure epoxy (Loctite® Epoxy Instant Mix™ 5 Minute) was placed at the edges of each ply prior to curing the composite to inhibit the flow of graphene around the edges. The offset three-ply samples were loaded as per ASTM standard D7264 with a span to thickness ratio of 32:1, using the thickness of the three-ply section of the composite specimen. In order to take multiple simultaneous measurements using the four-probe resistance measurement technique, four wire leads were attached to each ply of the specimen, with two at each end as illustrated in Figure 4.5a. The outermost wire leads on each ply were used to apply current through the ply, while the innermost wire leads were used to measure the corresponding voltage across each ply. In summary, the resulting data set contains three separate resistance measurements, corresponding to each ply, with each taken using the four-probe measurement technique. The samples were tested in two configurations: the LIG interlayers facing downward (tension configuration) shown in Figure 4.5c, and the LIG interlayers facing upward (compression configuration) shown in Figure 4.5d. This concept is discussed more fully in Section 3.5.

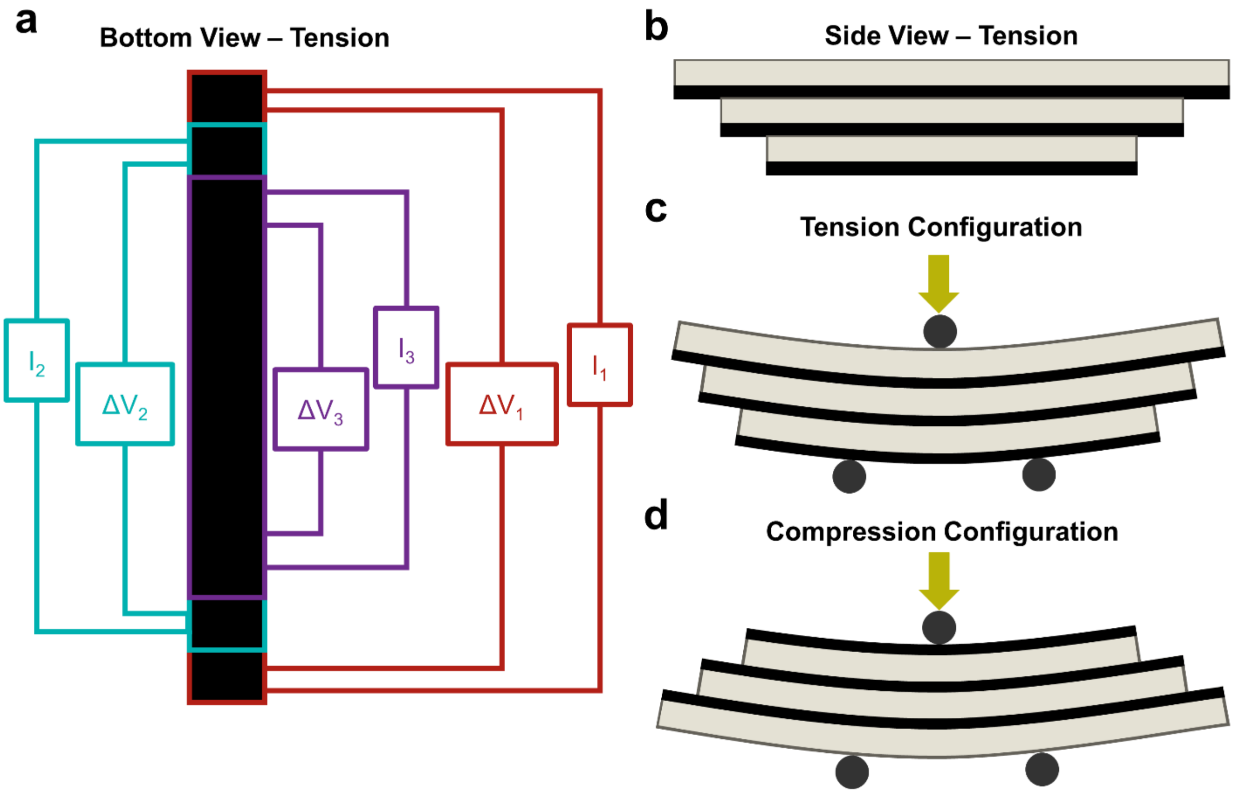

Figure 4.5. (a) Schematic of bottom view of tension configuration prior to flexural loading. (b) Schematic of side view of tension configuration prior to flexural loading. (c) Schematic of tension configuration during three-point bend testing. (d) Schematic of compression configuration during three-point bend testing.

4.4.2. Flexural Loading Results and Discussion

As a result of the three-point bend loading, the composite samples in this work experienced a combination of multiple significant types of damage including: interply delamination, fiber-matrix debonding, and fiber fracture, the combination of which resulted in the fracture of one ply. Images of these types of damage within the samples taken using an optical microscope are shown in Figure 4.6b and Figure 4.6h for the tension and compression samples, respectively. By measuring the change in resistance of each ply individually using the four-probe technique, the extent to which each ply was involved or affected by the damage was determined. Additionally, as previously stated, to evaluate the effect of the LIG orientation on the damage localization ability, the samples with LIG were tested in two separate configurations: the LIG surfaces oriented toward the bottom (tension dominant) and the LIG surfaces oriented toward the top (compression dominant) as represented in Figure 4.5c and Figure 4.5d, respectively. Due to the extreme separation in the bottom LIG interlayer during ply fracture in both configurations, a corresponding increase in resistance of ~80% (Figure 4.6f) in the tension configuration and ~20% (Figure 4.6l) in the compression configuration can be observed in the measurements across the damaged lamina. Additionally, a relatively small, but still significant increase in resistance (~20% in the tension configuration and ~5% in the compression configuration) can be observed in the center ply which delaminated from the severely damaged bottom ply (Figure 4.6e and Figure 4.6k). A comparison of the percent change in electrical resistance of each ply in the tension configuration to those in the compression configuration indicates a smaller percent change in conductivity in each ply loaded in the compression configuration. This is due to the fact that the LIG experiences higher strain in the tension configuration due to the relative location of the LIG to the neutral axis, as the LIG is at a point of higher positive stress in the tension configuration. As the LIG experiences positive strain, a large degree of separation occurs within each LIG interlayer resulting in increased electrical resistance. In contrast, the LIG on the bottom surface of the sample in the compression configuration is subjected to less positive strain which causes a lower increase in resistance. However, as each sample experiences significant fracture and delamination (Figure 4.6b and Figure 4.6h), the physical separation of the LIG interlayers results in a relatively large increase in resistance in both cases. By examining the relative changes in conductivity between each ply, it is clear that the ply at the bottom, which showed delamination and fracture, exhibited a significantly larger change in conductivity in comparison to the plies which experienced minimal damage in both the tension and compression configurations. Consequently, the samples with LIG are capable of locating the presence of damage through the thickness during flexural loading regardless of LIG orientation.

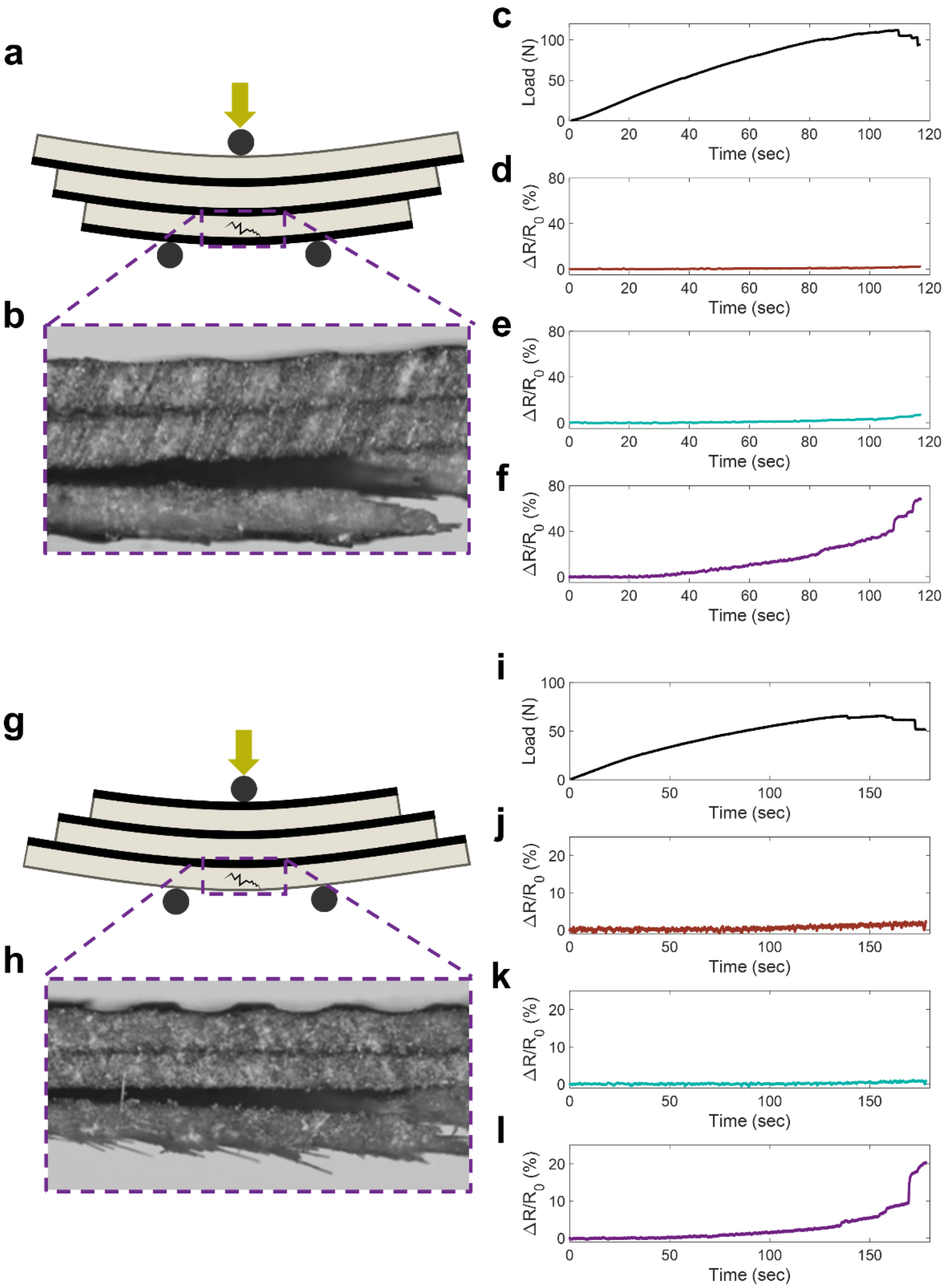

Figure 4.6. (a) Schematic of tension configuration and damage. (b) Optical microscope image of damage to the bottom ply. (c) Applied load, (d) percent change in resistance of the top ply, (e) percent change in resistance of the center ply, and (f) percent change in resistance of the bottom ply for one sample in the tension configuration during three-point bend testing. (g) Schematic of compression configuration and damage. (h) Optical microscope image of damage to the bottom ply. (i) Applied load, (j) percent change in resistance of the top ply, (k) percent change in resistance

of the center ply, and (l) percent change in resistance of the bottom ply for one sample in the tension configuration during three-point bend testing.

4.5. Two-Dimensional Damage Localization in a Plate

4.5.1. Experimental Methods and Test Setup

Square samples comprised of a single layer of LIG coated fiberglass combined with one additional layer of neat fiberglass prepreg ([0/90]° orientation) were used to investigate the potential of the LIG for two-dimensional damage localization using the normalized resistance change approach. The two-ply fiberglass composites with a single LIG layer were cut to square dimensions of approximately 70 mm by 70 mm and 85 mm by 85 mm, and wire leads were attached at ~1 cm intervals along each edge of the composite plates as shown in Figure 4.7a and Figure 4.7e. Prior to initiating damage to the composite, several initial resistance measurements were taken using an Agilent model 34401A digital multimeter. To accurately locate the position of the damage, these resistance measurements were taken in multiple configurations: horizontally and vertically across the plate (Figure 4.7b and Figure 4.7f), and diagonally across the plate in two directions (Figure 4.7c, Figure 4.7d, Figure 4.7g, and Figure 4.7h), similar to damage localization methods using the normalized resistance change method discussed in the literature [70, 137]. Each resistance value between two points was obtained with the current sourced in both directions, and the results were averaged between the two measurements. After the baseline measurements were recorded, a hole was drilled at an arbitrary position in the plate, and final resistance measurements were collected using the same methodology previously employed. The relative percent change in resistance between the final and initial measurements was then evaluated to locate the position of the damage in reference to the plate.

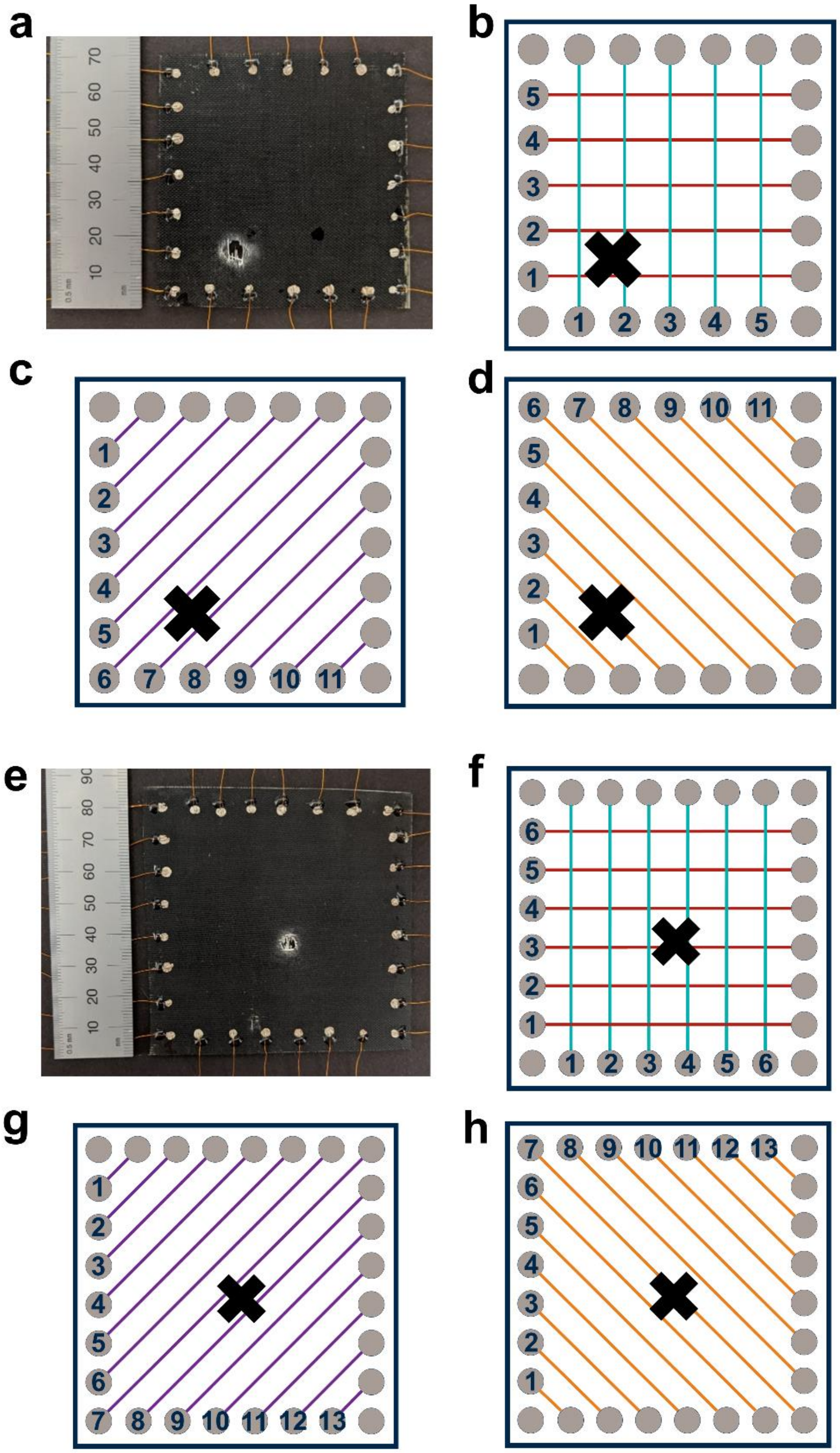

Figure 4.7. (a) Image of Sample 1 with offset hole. (b) Across (horizontal and vertical), (c) +45° diagonal, and (d) -45° diagonal current path measurements for Sample 1. (e) Image of Sample 2

with approximately central hole. (f) Across (horizontal and vertical), (g) +45° diagonal, and (h) -45° diagonal current path measurements for Sample 2.

4.5.2. Two-Dimensional Localization Results and Discussion

As a result of the addition of conductive LIG to a single ply of each plate, the initial resistance values across each plate fell within the range of ~170 – 370 Ω, while the diagonal initial resistance values fell within the slightly larger range of ~70 – 440 Ω, due to the difference in distance between nodes. To increase understanding of the damage localization capabilities of the LIG-coated composites, the holes were drilled at two different locations on the two different plates to evaluate relative differences in the localization accuracy with respect to damage location. On Sample 1 the hole was at an offset location closer to the corner (Figure 4.7a), while, the hole in Sample 2 was located closer to the center of the plate (Figure 4.7e). The resulting percent change in electrical resistance in Sample 1 from the vertical and horizontal measurements are shown in Figure 4.8a and Figure 4.8b, respectively. These measurements were then used to generate the resistance change intensity map shown in Figure 4.8c. For further analysis, the diagonal measurements taken across Sample 1 at +45° and -45° from the horizontal are shown in Figure 4.8d and Figure 4.8e, respectively, while the intensity map generated from the combination of both diagonal measurements is shown in Figure 4.8f. A visual evaluation of the difference in conductivity changes displayed in the mentioned figures conclusively shows that the percent change in resistance is significantly higher in the measurements whose direct paths pass across the damage. Furthermore, the point of highest percent change in each reconstructed intensity map clearly coincides with the grid point where the damage occurred on the sample itself. This is to be expected as the entirely nonconductive hole replaces the LIG which provides a conductive pathway throughout the area of the composite. Thus, a large loss of conductivity is expected in the area surrounding the hole, and this is confirmed by the resistance measurements.

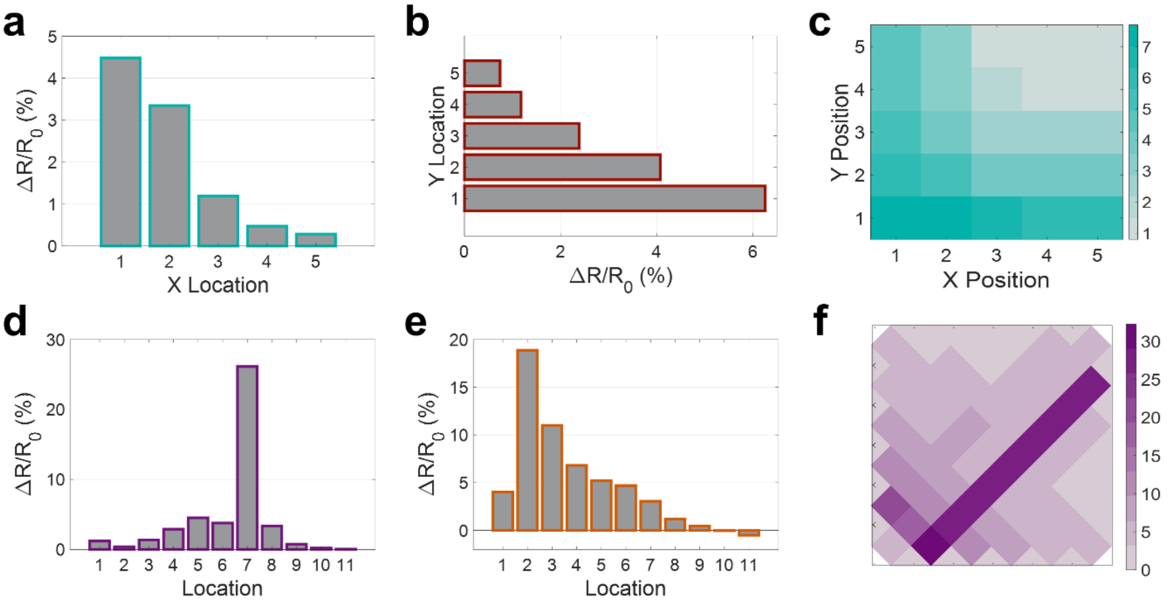

Figure 4.8. (a) Sample 1 percent change in resistance versus *x*-axis location. (b) Sample 1 percent change in resistance versus *y*-axis location. (c) Sample 1 percent change in resistance intensity map from across measurements. (d) Sample 1 percent change in resistance from +45° diagonal measurements. (e) Sample 1 percent change in resistance from -45° diagonal measurements. (f) Sample 1 percent change in resistance intensity map from diagonal measurements.

Similar to the first sample, an evaluation of relative changes in the electrical resistance of Sample 2 allows for the determination of the general location of the damage within the plate. The resulting percent change in electrical resistance in Sample 2 from the vertical and horizontal measurements are shown in Figure 4.9a and Figure 4.9b, respectively, and the corresponding two-dimensional intensity map is then shown in Figure 4.9c. For additional analysis, the diagonal measurements at +45° and -45° from the horizontal are presented in Figure 4.9d and Figure 4.9e, respectively, and the generated two-dimensional intensity map is seen in Figure 4.9f. As with the previous sample, the across measurements which correlate to the *x*- and *y*-position of the hole show the largest increase in resistance, however, the maximum percent change is smaller in magnitude than that of Sample 1. Furthermore, the diagonal measurements provide a location which is less clear than the changes observed in Sample 1 due to the lower overall change in conductivity. A closer comparison of the samples indicates that the resistance measurements show increased sensitivity if the damage is located closer to the measurement nodes. In the case of an offset hole, the nonconductive area is closer to the current source or sink used to measure the electrical resistance; this is expected to cause a greater disturbance in the measured conductivity. Whereas if the hole is located toward the center of the composite, the conductive area surrounding the defect provides some compensation, thus decreasing the sensitivity of the measurement. Overall, the measurements from Sample 2 assist in narrowing the region of damage within the plate, although a more specific location of the hole is not as evident from a visual comparison of the measurements and the two-dimensional intensity maps.

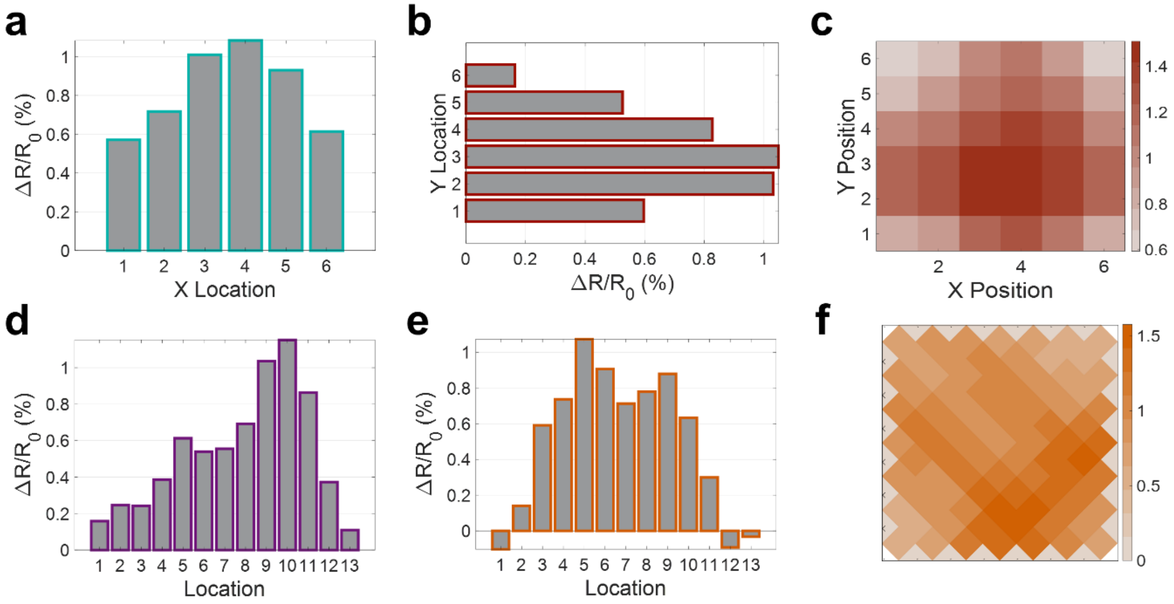

Figure 4.9. (a) Sample 2 percent change in resistance versus *x*-axis location. (b) Sample 2 percent change in resistance versus *y*-axis location. (c) Sample 2 percent change in resistance intensity map from across measurements. (d) Sample 2 percent change in resistance from +45° diagonal measurements. (e) Sample 2 percent change in resistance from -45° diagonal measurements. (f) Sample 2 percent change in resistance intensity map from diagonal measurements.

Although the two-dimensional intensity maps allow for quick visual approximation of the damage location, a more robust quantitative method is needed to quickly determine where on the plate the hole is located. For this purpose, the damage center was calculated for both across and diagonal measurements using adapted center of mass equations, shown as Equation 4.1 and Equation 4.2, following the methodology of Gallo and Thostenson [70], where x_n and y_n are the x-location and the y-location of the center of the measurement, respectively, ΔR_n is the local change in resistance corresponding to the location, and ΔR_{total} is the total change in resistance of measurements taken in the same direction.

$$x_c = \frac{\sum_{i=1}^{n} x_n \Delta R_n}{\Delta R_{total}} \tag{4.1}$$

$$y_c = \frac{\sum_{i=1}^{n} y_n \Delta R_n}{\Delta R_{total}} \tag{4.2}$$

The calculated damage center for both across and diagonal measurements in comparison to the actual damage center for both samples are shown in Figure 4.10a and Figure 4.10b for Sample 1 and Sample 2, respectively, and a comparison of the calculated coordinates with the approximated actual coordinates of the damage are shown in Table 4.1. In both the case of the center and offset hole, the diagonal measurements result in more accurate damage center predictions, which is attributed to the increased number of measurement points and the fact that multiple measurements are sourced from each node. The results also indicate that although the overall percent change in resistance is lower in the plate with a center hole, the calculated center of damage is closer to that of the actual damage with a maximum percent error of ~0.3 cm. The improved accuracy in detecting the location of damage if it is closer to the center than the edge of the plate is similar to previous results from other works using alternative conductive nanoparticles [70], and is expected to be due to an inherent bias of the calculation toward the center of the plate. The majority of the sum of the resistance change (ΔR_{total}) is located throughout the entirety of the plate which is beyond the coordinate of the damage center thus biasing the results. Overall, the center of the damage was predicted with a maximum error of ~1 cm which correlates to the approximate distance between measurement points, thus indicating that an increase in node frequency has potential to increase the measurement accuracy. In summary, a combination of visual inspection of the resistance change intensity maps combined with a calculated approximation of the damage center results in a relatively accurate estimation of the damage location in two dimensions, regardless of the location of the damage, using a scalable and non-intrusive approach.

Table 4.1. Actual damage coordinate versus calculated damage coordinate for both Sample 1 and Sample 2.

	Sample 1		**Sample 2**	
	Actual	**Calculated**	**Actual**	**Calculated**
***x*-coordinate**	1.6	1.8	3.9	3.6
***y*-coordinate**	1.0	2.0	2.7	3.0
distance from origin	1.9	2.7	4.7	4.7

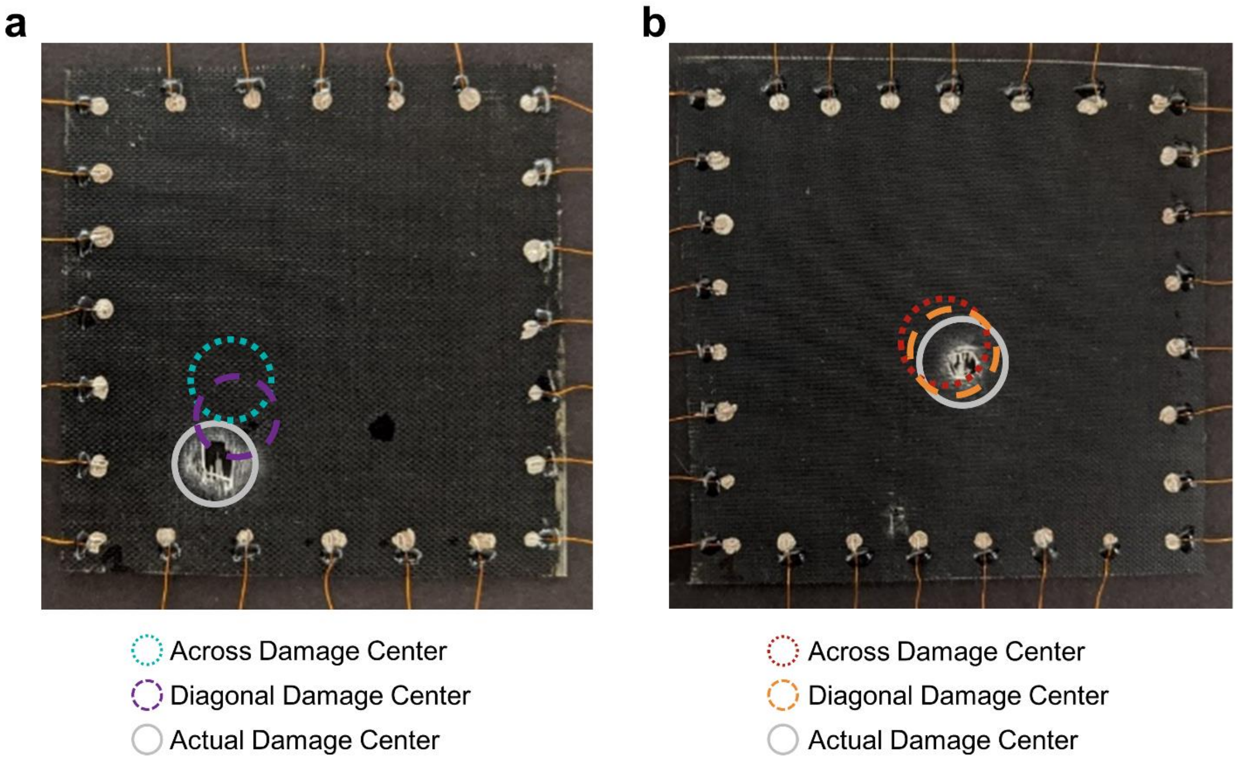

Figure 4.10. (a) Sample 1 damage center calculated from across and diagonal measurements compared to actual damage center. (b) Sample 2 damage center calculated from across and diagonal measurements compared to actual damage center.

4.6. Chapter Summary

This chapter examines the exploitation of the simple and scalable LIG process for the localization of damage in traditionally non-conductive fiberglass prepreg composites using piezoresistive measurements. A series of simultaneous voltage measurements stemming from a single current input allows for the localization of tensile damage in one-dimension in-situ using the piezoresistance of the LIG. An adjusted method was then employed to apply three individual current sources and record the corresponding voltage measurements, one pair for each individual ply, to use the relative changes in conductivity to locate delamination and ply fracture through the thickness. Finally, a combination of several discrete resistance measurements was used to detect the location of a hole in a two-dimensional plate. Although current scattering is observed to affect the ability to accurately predict the damage center, with a maximum error value of ~1 cm in the distance between the actual center and the calculated center, the general location of the damage was proven to be detectable in plates with varying damage locations by using the piezoresistance of the LIG. Therefore, the result of this chapter is the effective localization of damage within fiberglass-reinforced composites in three-dimensions using piezoresistive sensing methods. The processes used in this work excel in their scalability and automatability in addition to the fully integrated nature of the sensing component, thus simultaneously removing complicated processing methods and the need for external or discrete sensors for resistance-based damage localization.

CHAPTER 5

Fatigue Damage Sensing and Life Prediction of Fiberglass-Reinforced Composites Using Laser Induced Graphene

5.1. Chapter Introduction

The work described in this chapter further exploits piezoresistive laser induced graphene (LIG) integrated into fiberglass-reinforced composites for in-situ fatigue damage monitoring and lifespan prediction. The LIG is integrated within fiberglass composites using the same transfer-printing process described in Chapter 3, after which the composite samples are subjected to tension-tension fatigue loading. The addition of the conductive LIG within the traditionally insulating fiberglass composites is proven to enable direct in-situ damage monitoring through simple passive resistance measurements which are capable of tracking the progression of damage throughout the lifespan of the composites. The accumulation and propagation of structural damage are detected throughout the fatigue life of the composite through changes to the electrical resistance measurements, and the measurement trends are further used to predict the onset of catastrophic composite failure. Thus, this work expands the use of multifunctional fiberglass composites containing LIG for unpredictable, dynamic loading environments.

5.2. Materials and Methods

5.2.1. Composite Fabrication

The composite samples were fabricated following the same steps outlined in Section 3.2.2.1. In short, a commercial polyimide film (2 mil (0.0254 mm) thick Kapton®) was irradiated using a 40 W CO_2 infrared laser (Epilog Zing 16 universal laser system). Following the conversion of the polyimide to LIG, the LIG interlayer was transferred to the surface of an uncured fiberglass prepreg (CYCOM® E773 epoxy prepreg with S-2 glass fiber-reinforced roving) through a transfer printing process that consists of rolling the prepreg onto the LIG-coated polyimide substrate while applying manual pressure. The LIG was thus embedded in the uncured prepreg, forming an interlayer, after which the fiberglass prepreg layers were combined in a [+45/-45/+45]° stacking sequence and cured in a hot press at 127 °C under 100 psi (689.5 kPa) for two hours. Once the composite panel was cured, samples were cut to 10 mm in width and 76 mm in length for quasi-static tensile testing to failure and tension-tension fatigue testing. Fiberglass tabs were then attached to each end of the sample with high shear strength epoxy (Loctite® 9430™ Hysol®) before adding sandpaper to the outside of the fiberglass tabs to eliminate slipping during the testing. To enable resistance measurements of the composite samples during testing, thin lines of silver paint were added around the edge of the sample at each end, resulting in a conductive pathway between each ply. Consequently, the resistance measurements taken between each silver paint ring were those of the entire composite rather than just the LIG interlayer at the surface ply. Additionally, copper wires were attached to the silver paint rings using additional silver paint and quick-cure epoxy (Loctite® Epoxy Instant Mix™ 5 Minute) to keep the wires fixed during testing. For reference, the electrical resistance of the samples following the completion of the fabrication process ranged between 200 – 900 Ω. Finally, white spray paint was used to speckle the top LIG-coated surface of the sample for digital image correlation (DIC) measurements.

5.2.2. Fatigue Testing Setup

The completed samples were first tested in a quasi-static tensile test to failure using an Instron model 5982 test frame with a 100 kN load cell according to ASTM standard D3039. Seven samples from multiple composite panels were tested to determine the average ultimate stress of the LIG-coated fiberglass composites ($\sigma_{ultimate}$). Following the testing to failure, ten additional samples were tested in a load-controlled tension-tension fatigue test using an Instron ElectroPuls^{TM} model E1000 test frame with a ±1 kN load cell. A sine wave excitation was used at a 10 Hz frequency and an R-value of 0.1, where R is defined as the ratio between the minimum stress and the maximum stress during the loading cycle ($R = \sigma_{min}/\sigma_{max}$), with the maximum stress ranging from 65-78% of $\sigma_{ultimate}$. While the elastic stiffness of the samples was monitored by the test frame, images for DIC analysis were taken using a Photron FASTCAM Mini AX 200 high-speed camera at 1,000 frames per second (FPS) in periodic bursts throughout the tests. The electrical resistance of each sample was concurrently monitored using a Wheatstone bridge through the test, where the circuit input was provided by a DC power supply (Hewlett Packard model 6217A) and the output was recorded using a National Instruments (NI) compact data acquisition system (cDAQ 9174) with an NI-9223 input module. A schematic of the fatigue test setup is shown in Figure 5.1.

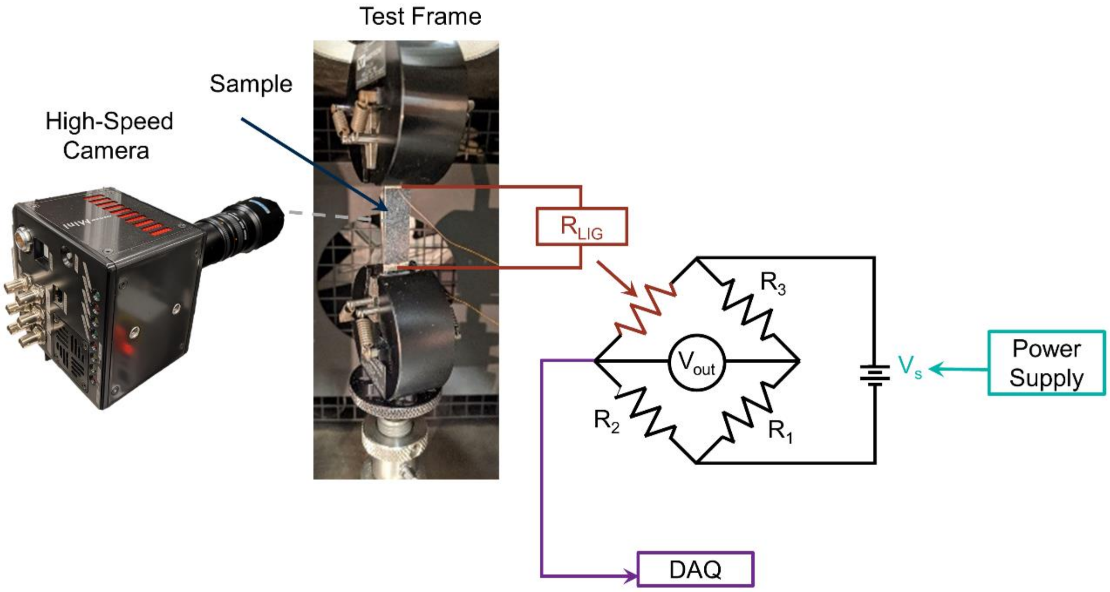

Figure 5.1. Schematic of fatigue sample in test frame with setup for in-situ resistance monitoring and DIC analysis.

5.3. Fatigue Testing Results

Throughout the fatigue testing, the elastic modulus of the specimens was measured by the load frame, while the accumulation of damage in the sample was monitored through DIC measurements. To provide a more direct comparison between samples, the calculated values for the modulus and strain were normalized by their respective values at the beginning of the first loading cycle. Additionally, the normalized fatigue life of each sample was determined by normalizing the cycles during each test by the corresponding number of cycles to failure for each sample. The normalized decrease in the elastic modulus versus the normalized fatigue life for each sample is shown in Figure 5.2a. As expected, the observed trends in decreasing stiffness allow for the categorization of the fatigue tests into three main regions. The literature has defined these regions by the type of damage initiation and propagation predominantly experienced by the sample during those portions of the fatigue life [58, 138]. In region I (approximately < 15% of fatigue life), the sample failure is dominated by matrix cracking throughout the composite. Since the samples tested here consist of entirely off-axis plies, the matrix cracking occurs in each ply and results in a relatively high rate of increase in the average strain experienced by the sample during this region [138]. This can also be confirmed by the DIC measurements shown in Figure 5.2b, which indicate a sharp increase in strain during the same portion of the test. Region II (approximately 15 – 85% of fatigue life) is characterized by interfacial debonding occurring within the interlaminar area of the composite, delamination occurring along the off-axis fibers, additional matrix cracking, and the propagation of all these types of damage. During this portion of the test, both the decrease in modulus and the measured strain show relatively linear increases at a lower rate than that observed in region I or III, which is characteristic of the damage propagation in region II [138]. Finally, region III (approximately > 85% of fatigue life) occurs toward the end of the test and immediately preceding failure of the composite. This portion of the test is characterized by severe fiber fracture and pullout combined with a large degree of delamination along the fiber direction, both of which result in the dramatic decrease in modulus and increase in strain observed in Figure 5.2a and Figure 5.2b, respectively. It can be therefore noted that the trends observed here are similar to those observed in previous studies reported in the literature [138-140].

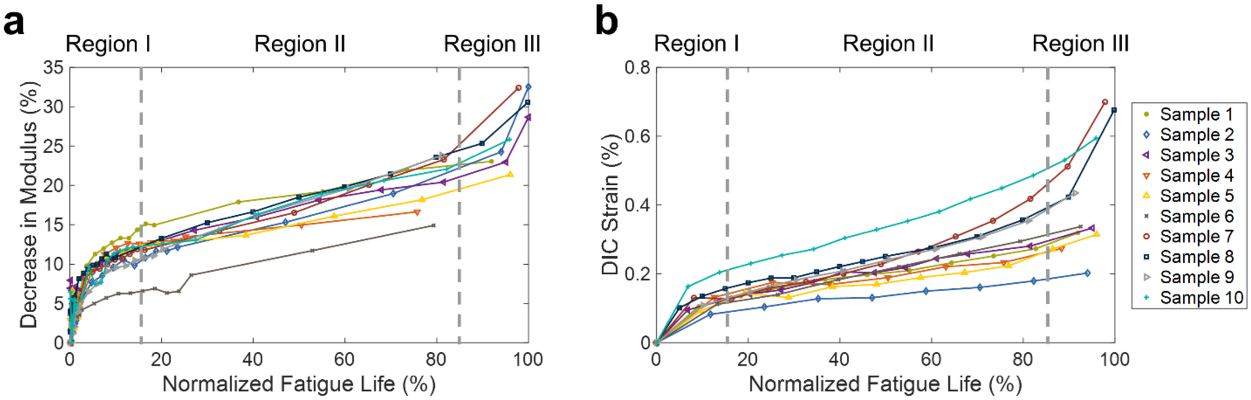

Figure 5.2. (a) Decrease in modulus versus normalized fatigue life. (b) Strain from DIC measurements versus normalized fatigue life.

In addition to monitoring the structural changes using the modulus and strain measurements, the electrical resistance of the samples was also measured throughout the duration of the test to evaluate the self-sensing capabilities of the composites containing LIG. As the samples were cyclically loaded at 10 Hz, the resistance measurements were averaged to obtain one representative measurement each second, resulting in one measurement point for every 10 cycles. The resistance measurements were then normalized by the mean resistance value measured during the first second of the test in order to enable accurate comparison between samples. The resulting average percent change in resistance for each sample versus the normalized fatigue life is shown in Figure 5.3. The trends in the resistance also show some correlation to the three regions characterized by the type of damage occurring within the fiberglass samples. Since the piezoresistive LIG is located within the matrix at each ply level, multiple damage types including matrix cracking, delamination, and fiber breakage are all detectable by the changes in electrical resistance due to the resulting physical separations within the LIG interlayer as discussed in Chapter 3. However, the increase in resistance experienced during matrix cracking, which occurs during region I, is considerably less pronounced than the increase observed during debonding, delamination, and fiber failure which occur during regions II and III. This can be explained by the fact that matrix cracking results in less physical separation within the LIG interlayer, and therefore it is less likely to significantly affect the electrical conductivity. Nonetheless, the trends in the percent change in the mean resistance can be used to track the progression of fatigue damage within the composite samples throughout each region of the fatigue life.

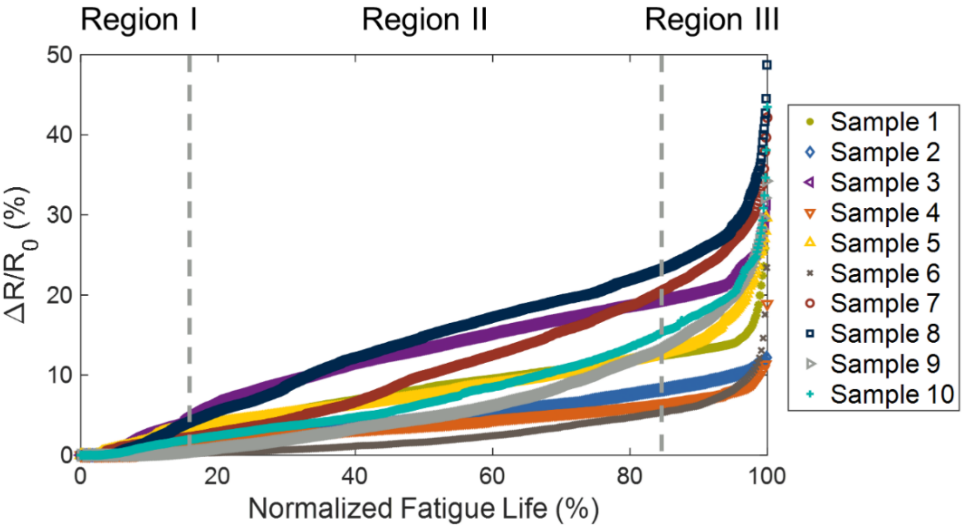

Figure 5.3. Normalized change in resistance versus normalized fatigue life.

In addition to relying on the percent change in resistance to evaluate the progression of damage within the fiberglass composites samples, the first derivative of the normalized resistance taken with respect to the number of cycles provides further insight into the mechanisms at play in the increasing resistance measurements. Figure 5.4 shows the first derivative of the normalized percent change in resistance taken with respect to the number of cycles in log-scale versus the normalized fatigue life. It should be noted that the results shown in Figure 5.4 are not a direct derivative of those shown in Figure 5.3, and are instead the derivative of the normalized resistance measurements with respect to cycles during the test rather than the normalized fatigue life. It is apparent from the results in Figure 5.4 that the same three regions defined by the physical effects of the damage within the composite samples are also clearly detectable by the variation in the slope of the first derivative of the normalized electrical resistance throughout the normalized fatigue life. Initially during region I, where matrix cracking is the dominant damage form, the normalized resistance (Figure 5.3) increases at a relatively low rate resulting in a lower derivative (Figure 5.4). This is due to the location of the LIG within the matrix of the composite. Thus, as the matrix is damaged, a relatively small amount of corresponding separation occurs within the LIG. Then, as delamination, debonding, additional matrix cracking, and some small fiber damage occur, the resistance increases approximately linearly, which results in a constant derivative. During region III, however, the fiber breakage and severe delamination result in significant physical separation between conductive contacts within the LIG interlayers, leading to a non-linear increase in electrical resistance, which correlates to the non-linear physical effects (Figure 5.2). The described trends are notably consistent regardless of the initial specimen resistance or applied stress, thus yielding the good alignment observed in Figure 5.4. As a result of the consistency in the trends observed from each sample and the distinctive regions I, II, and III, the derivative of the normalized resistance with respect to cycles is a promising candidate for fatigue life prediction, which will be further discussed in a later section.

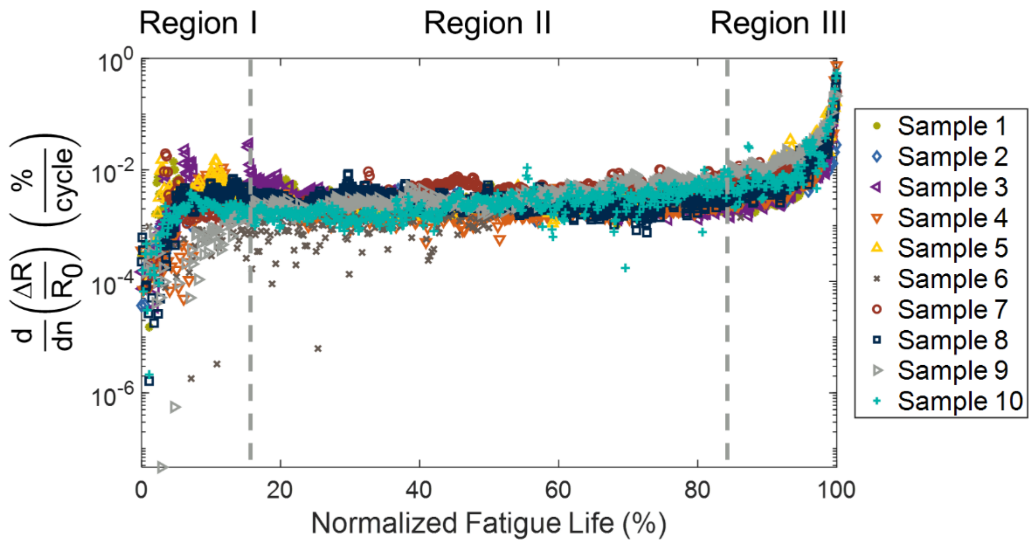

Figure 5.4. Derivative of normalized change in resistance versus normalized fatigue life.

To provide a visual comparison between the three measurement methods, the percent change in resistance, decrease in modulus, and physical damage observed using DIC measurements for a representative sample (Sample 8) are shown in Figure 5.5a and Figure 5.5b. The images corresponding to the DIC measurements (Figure 5.5b) represent the strain in the loading direction (ε_{yy}), which is 45° off-axis from the fiber orientation of each ply. The combined data in Figure 5.5 further validates the conclusions drawn regarding the damage detected during each region of testing. While the matrix cracking in region I results in a slight decrease in modulus and visual increase in strain, the increase in resistance and decrease in modulus become approximately linear when damage progresses through region II, as some delamination along the fibers is visible in the DIC images. Then, in region III at the end of the test (>85% fatigue life), the non-linear increase in the resistance is visually correlated to fiber breakage and severe delamination, highlighted by the highly concentrated areas of damage in the DIC images, as the sample fails in shear due to the stacking sequence of the plies. For additional confirmation of the correlation between the changes in normalized resistance and the strain measured by the DIC, a comparison of the normalized resistance and DIC strain for three representative samples is shown in Figure 5.5c. From the figure, the trend in measured resistance is shown to correlate well to the trends in the measured strain due to the piezoresistivity of the LIG. This correlation improves as the test progresses through region II and III as the fatigue life is between ~40 – 100%. This is expected based on the work outlined in Chapter 3 which investigated the ability of LIG to track strain in fiberglass-reinforced composites through resistance measurements.

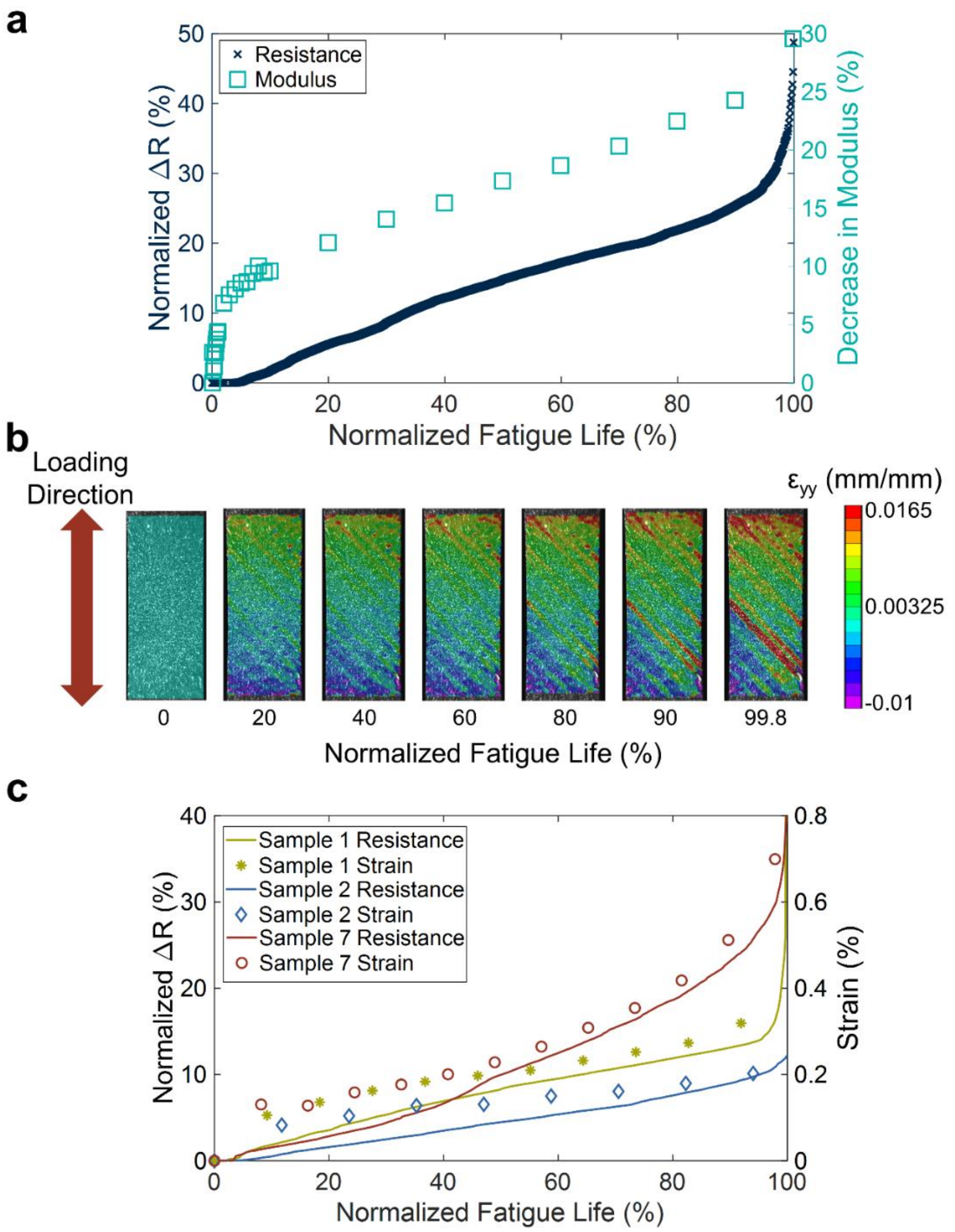

Figure 5.5. (a) Normalized change in resistance and decrease in modulus versus normalized fatigue life. (b) DIC images of ε_{yy} versus normalized fatigue life. (c) Normalized change in resistance and DIC strain versus normalized fatigue life.

In addition to monitoring the mean resistance measurements, the peak-to-peak value of the resistance was also used to track trends in the structural damage to the composite during fatigue loading. In contrast to the mean resistance values, the peak-to-peak values represent the maximum peak-to-peak value over one second of data. As a result, the measurements were highly susceptible to environmental noise, and a post-processing filter was used to reduce the high-frequency noise and eliminate the data points corresponding to high levels of noise. It should also be noted that the peak-to-peak measurements were normalized by the initial value of the peak-to-peak resistance during the first second of data to again provide a fair comparison between samples. Since the tests were performed in a load-control mode, the specimens exhibited larger strains as testing progressed while the elastic modulus decreased due to the accumulated damage. This expected increase in peak-to-peak strain values in return led to increased peak-to-peak resistance measurements as a direct consequence of the piezoresistance of the LIG. It can also be noted that a similar increasing trend in the peak-to-peak resistance measurements of fiberglass composites containing CNTs has also been reported in the literature [141]. The resulting normalized changes in the peak-to-peak resistance measurements versus the normalized fatigue life for each sample tested are shown in Figure 5.6. From the figure, the peak-to-peak resistance measurements increase approximately linearly until the sample approaches region III of failure. As the samples near failure in region III, the moduli change non-linearly, and the peak-to-peak resistance measurements show a similar trend due to the severe damage experienced by the composite samples in this region. The relatively linear behavior through region I is attributed to the fact that in that region, the minor changes in specimen modulus do not cause sufficiently large alterations in the slope of the peak-to-peak strain, which in return minimizes changes within the peak-to-peak resistance measurements. The response in region II is linear as expected because changes in the modulus, strain, and mean resistance measurements are observed to be approximately linear here. This linearity is due to the relatively constant increase in damage modes experienced in this region. In summary, the peak-to-peak resistance measurements are promising for the estimation of fatigue life due to the consistently linear increase in the normalized value during region I of the fatigue life.

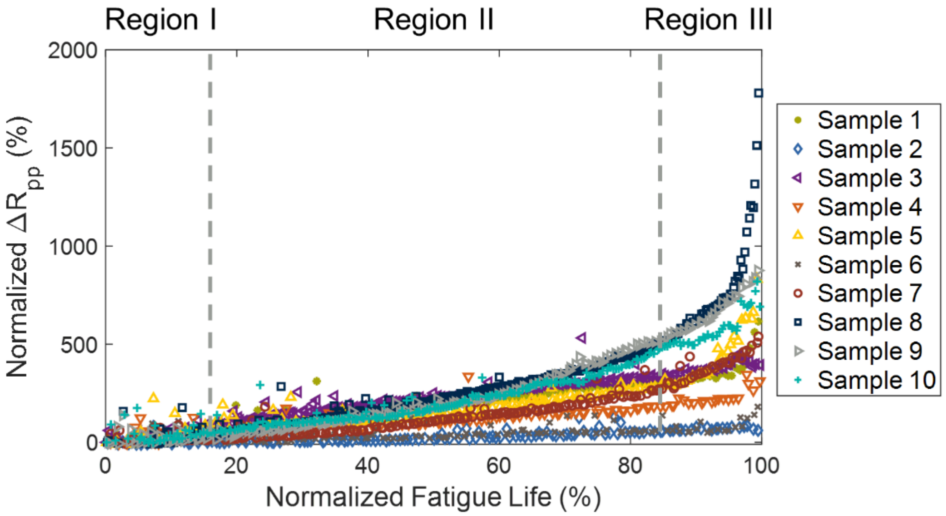

Figure 5.6. Normalized peak-to-peak resistance versus normalized fatigue life.

5.4. Fatigue Life Prediction

Further analysis of the normalized peak-to-peak resistance measurements indicates that a certain degree of correlation exists between the rate of increase in the peak-to-peak resistance and the fatigue life of the fiberglass composite. To take advantage of the proportional relationship between the resistance and strain measurements, a linear fit was applied to the normalized peak-to-peak resistance versus the cycles during the first portion of the test (0 – 2,000 cycles). The normalized experimental peak-to-peak data and the corresponding linear fit for the first 2,000 cycles are shown in Figure 5.7a for a representative sample (Sample 3). The cycle range correlates to the data up to 20 – 50% of the fatigue life for the samples tested in this work. In order for fatigue life prediction to be maximally effective, it is desirable that the estimation be made early during the life of the composite prior to the occurrence of significant damage to the composite material.

Once the linear fit was applied to the first 2,000 cycles of each sample, the maximum number of cycles was plotted versus the slope of these linear fits for each sample (Figure 5.7b). From the figure, the fatigue life of the sample is shown to increase approximately linearly with the slope of the normalized peak-to-peak resistance. A least-squares linear fit of the trend seen in Figure 5.7b results in a good correlation with the experimental data, as the majority of test specimens fall within one standard deviation of the fit. Therefore, the results indicate that the slope of the normalized peak-to-peak resistance versus the cycle number within region I and the early part of region II during the fatigue life is a promising approach for obtaining an initial estimation of the predicted fatigue life of the test specimen without requiring knowledge of the applied load.

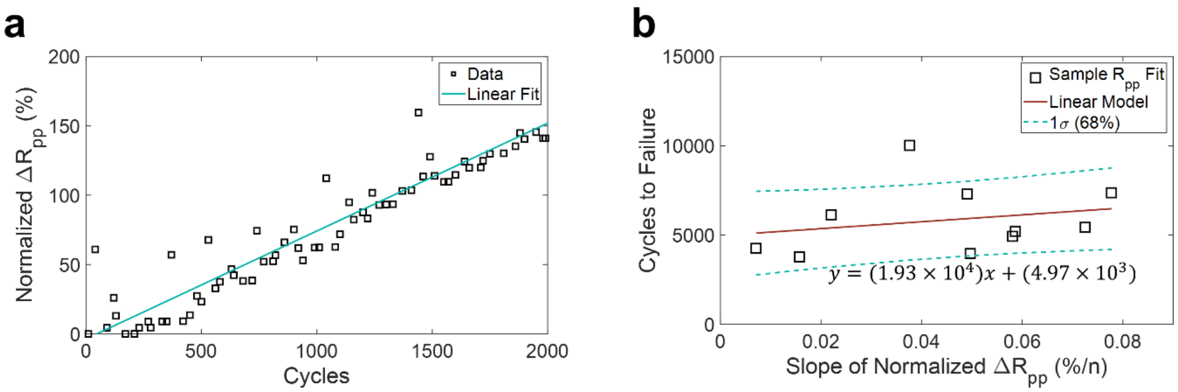

Figure 5.7. (a) Sample 3 normalized peak-to-peak resistance versus cycles with a linear fit. (b) Fatigue life versus slope of normalized peak-to-peak resistance with a linear fit.

Although the normalized peak-to-peak resistance can provide some indication of the sample fatigue life, additional information regarding the progression towards structural failure is still desirable during unpredictable, dynamic loading environments. For this reason, additional analysis was completed for the derivative of the normalized resistance measurements. As previously stated, the trends in the derivative showed good correlation for each sample tested during the entirety of the fatigue life, regardless of the applied load or induced strain. Figure 4 illustrated that each sample showed a relatively constant derivative during region II with a slight increase, followed by a non-linear increase as the sample approaches failure in region III. Thus, the observed trends from region II and region III show a close correlation with an exponential curve. In order to further exploit this relationship, the derivatives of the samples were averaged over the normalized fatigue life, and a non-linear least-squares curve fit was applied to obtain a model exponential curve correlating to the relationship between the $\log_{10}$ of the mean derivative and the sample fatigue life. It is interesting to note that while this method, which uses the derivative of the resistance, models the relationship between the entirety of the data set and the fatigue life, the prior method using the peak-to-peak resistance utilizes only a single data point representing each sample to obtain the predicted fatigue life. The experimental first derivative corresponding to the entire sample set, calculated average of the sample derivatives, and the resultant exponential fit are shown in Figure 5.8. From the figure, the exponential curve shows excellent correlation with the mean derivative and good correlation to the bulk of the experimental data from all samples tested. The results thus indicate the derivative of the normalized resistance measurements with respect to cycles can be correlated to the fatigue life of the sample with no knowledge of the loading amplitude or fatigue life. Although there is some variation in the derivatives early on during the test (< 20% normalized fatigue life), the peak-to-peak measurements can be used to provide an initial estimation of the fatigue life during region I, while the derivatives can be used to provide a more accurate fatigue life estimation as the sample progresses towards failure in regions II and III.

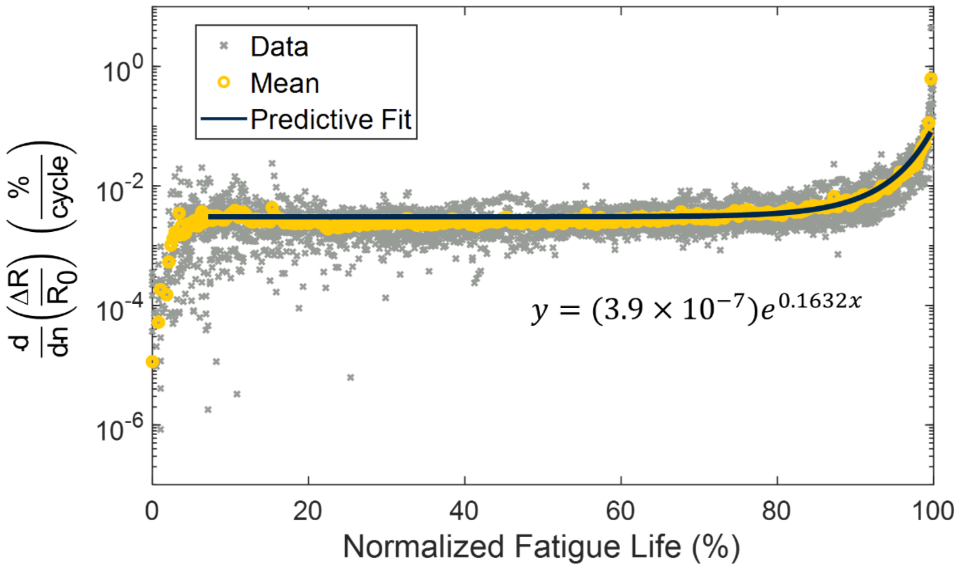

Figure 5.8. Derivative of normalized change in resistance versus normalized fatigue life with exponential predictive fit.

5.5. Chapter Summary

This work utilizes piezoresistive LIG for fatigue damage tracking and fatigue life estimation in fiberglass-reinforced composites. First, LIG is integrated within fiberglass composites using a scalable transfer-printing process, after which the composite samples are subjected to tension-tension fatigue loading while monitoring the stiffness, strain, average electrical resistance, and peak-to-peak electrical resistance. The results indicate that the normalized resistance measurements and peak-to-peak resistance measurements can be used to track matrix cracking, delamination, and fiber failure within the loaded fiberglass composites. Additionally, the peak-to-peak measurements were observed to increase approximately linearly with the number of cycles, and the corresponding slope was shown to have an approximately linear relationship with the overall fatigue life of the sample. The slope of the peak-to-peak measurements can therefore be used to estimate the fatigue life during region I and the first part of region II of the composite fatigue damage. Furthermore, an exponential model is used to correlate the derivative of the normalized resistance measurements to the fatigue life as the samples approach fatigue failure (> 75% of normalized fatigue life). Thus, for the first time, piezoresistive LIG is used for both damage tracking and fatigue life estimation in fiberglass composites, signifying that this novel multifunctional material is promising for structural health monitoring applications in unpredictable dynamic loading environments.

CHAPTER 6

Conclusions

Fiber-reinforced polymer matrix composites have extensive applications with increasing projected use, however, these materials are prone to multiple forms of damage which have the potential to significantly impact the structural integrity of the component or lead to catastrophic failure. Structural health monitoring (SHM) research has turned to a variety of sensing materials that can be externally bonded or discretely embedded within composite materials to detect damage, however the methodologies used are limited in widespread application due to the parasitic aerodynamic effects and environmental exposure of external sensors or the detrimental structural effects caused by the embedding of discrete sensors. To overcome these barriers, more recent research has turned to multifunctional materials to meet the demands of SHM systems by using the inherent properties of the material itself, with the most common example being the use of piezoresistive carbon fiber composites to self-sense strain and damage through changes in the electrical resistance of the composite. However, in the case of electrically insulating fibers such as aramid and glass, efforts to integrate piezoresistive nano- or micro-scale materials have not been widely implemented in industry due to difficult processing limitations or the extreme processing temperature and chemical environments required. Thus scalable, automatable solutions are needed to integrate self-sensing functionality within fiber-reinforced composites without detrimentally affecting the structural properties of the material. The purpose of the research in this dissertation is to overcome current barriers to the widespread use of multifunctional composite materials for in-situ damage sensing by using scalable processes with potential for automation. This has been accomplished for both piezoelectric and piezoresistive nano- and micro-scale materials which were integrated within the composites during the fabrication process, and were conclusively shown to be effective in detecting damage in-situ during multiple loading configurations.

6.1. Brief Summary of Results

The fundamental investigations in this work outline multiple alternatives to advance the current state-of-the-art in multifunctional self-sensing materials. In Chapter 2, two multifunctional materials were characterized for damage sensing in fiber-reinforced composites: an interphase of piezoelectric zinc oxide (ZnO) nanowires on aramid fabric, and a piezoelectric dehydrofluorinated polyvinylidene fluoride (DHF PVDF) prepreg fabricated using woven fiberglass. The electrically insulating fabrics with integrated piezoelectric components were then sandwiched between conductive carbon fiber electrodes to form a composite structure with similar functional components to a traditional piezoelectric sensor. The ability of these materials to self-sense damage through passive voltage measurements taken across the thickness of the composite was investigated during flexural and tensile loading, the results of which illustrate that the fabricated multifunctional materials are capable of providing information comparable to that provided by a commercial acoustic emission sensor.

Previous efforts to integrate piezoresistive nanomaterials within aramid fiber composites have faced hurdles in application due to the incompatibility of extreme processing conditions with the polymer fibers. In contrast, the work discussed in Chapter 3 takes advantage of the chemical composition of aramid fabric to directly print laser induced graphene (LIG) onto the surfaces of woven aramid fabric. As a result, the treated composites contained an integrated piezoresistive LIG interlayer at each ply level of the composite. The subsequent investigation exploited this integrated piezoresistance as the resultant structural composites were shown to be capable of self-sensing elastic and plastic deformation in-situ during tensile and flexural loading, while permanent deformation was also shown to be detectable through residual changes to the sample resistance.

Similar to aramid composites, fiberglass composites also lack inherent piezoresistivity. Therefore, the investigation of LIG as an integrated functional material was expanded to include fiberglass composites. Since the ceramic nature of the fiberglass is not conducive to the direct conversion of the fiber surfaces to LIG, the use of a novel transfer printing process was established to fully embed the LIG within commercial fiberglass prepreg and form piezoresistive interlayers. The sensing capabilities of the resultant piezoresistive composites were then examined using both tensile and flexural loading configurations, during both of which the composites were shown to detect applied strain and structural damage through changes to the electrical resistance of the composite. In addition to embedding a continuous LIG interlayer, the concept of transfer-printed LIG-based strain gauges was also investigated for integrated strain sensing in fiberglass composites. The resultant embedded sensors were shown to be tailorable in size and strain sensitivity with application in both quasi-static and dynamic loading environments, thus exhibiting promising SHM potential.

Beyond simple damage detection during monotonic loading, the localization of damage within composites is also a crucial aspect of effective SHM systems. Therefore, in addition to the previously described in-situ testing, damage localization in fiberglass composites with LIG was also further investigated. To accomplish this, three separate sets of tests were used to establish the damage localization potential in all three-dimensions of the composite. First, a series of simultaneous voltage measurements stemming from a single current input allowed for the localization of tensile damage along a one-dimensional beam. An adjusted method was then employed to apply the four-point probe method to each ply in a composite beam, and the relative changes in the measured electrical resistance were used to locate delamination and ply fracture through the thickness. Finally, a combination of several discrete resistance measurements was used to detect the location of a hole in a two-dimensional plate. In each case, the general location of the damage was proven to be detectable through local changes in the resistance of the LIG, thus establishing the potential of the multifunctional composites to localize damage in all three dimensions of a composite.

Finally, since unpredictable dynamic loading environments are common in composite materials used for aircraft and aviation, fatigue testing was also considered for the fiberglass composites with LIG. The resultant work discussed in Chapter 5 investigated the response of the samples loaded in a tension-tension fatigue configuration while monitoring the stiffness, strain, average electrical resistance, and peak-to-peak electrical resistance. The results indicate that the normalized resistance measurements and peak-to-peak resistance measurements can be used to track matrix cracking, delamination, and fiber failure within the loaded fiberglass composites throughout the entirety of the fatigue life. Further analysis also established consistent trends within the resistance measurements across each of the tested samples, which informed two models for fatigue life prediction that rely solely on the resistance measurements and are independent of the applied load. Therefore, the piezoresistive LIG was shown to be capable of tracking fatigue damage and predicting fatigue life in fiberglass composites during cyclic fatigue loading.

6.2. Contributions

The main contributions of this work center around the integration of functional materials within fiber-reinforced composites that enable self-sensing of damage and, in some cases, strain without detrimentally affecting the structural properties of the composites. Furthermore, the processes used throughout this dissertation overcome current barriers inhibiting the widespread application of multifunctional materials by using simple, scalable methodologies with the potential for automation. This has led to significant contributions to the state-of-the-art in multifunctional materials. In particular, the work discussed in Chapter 2 which uses integrated piezoelectric ZnO for in-situ damage sensing, when combined with previous works which utilize ZnO nanowires within similar composite materials [88], results in a self-sensing structural material with improved mechanical properties that is also capable of harvesting small amounts of energy from ambient vibrations. The outcome is thus a truly multifunctional structural material with the integrated functionality of multiple subsystems. This was accomplished by designing the stacking sequence of the composite to mimic the functional components of a piezoelectric sensor, before expanding this design principle to include additional functional materials by validating the approach using a piezoelectric DHF PVDF prepreg. It can thus be concluded that the methodology used for self-sensing damage in Chapter 2 can also be extended to alternative structural composites containing integrated piezoelectric materials in the form of nanoparticles, nanowires, or films. It is also worthwhile to note that the use of DHF PVDF to form an electroactive prepreg was also the first of its kind, as no other research has documented the formation of a prepreg with PVDF that possesses thermally stable electroactive potential.

The work in this dissertation also scientifically investigates, for the first time, the use of LIG directly printed onto aramid fabric to form a self-sensing piezoresistive composite. The simplicity of the methodology used and the inherent compatibility of the process with aramid fabric significantly improves on the current techniques used to introduce similar piezoresistive functionality, thus overcoming current hurdles for the widespread application of piezoresistive SHM methods for aramid composites. In addition, LIG-coated aramid fiber-based composite materials have also been shown to exhibit improved interlaminar properties [119]; therefore, the combination of the work discussed in this dissertation with prior work once again results in a multifunctional composite with improved structural properties and integrated self-sensing capabilities using scalable methodology.

In a similar manner, a simple and scalable two-step transfer printing process was introduced to integrate LIG within commercial fiberglass prepreg, thus adding piezoresistive functionality to composites which are traditionally electrically insulating. Notably, the techniques used are highly compatible with roll-to-roll processing, which is promising for the up-scaling of these materials and methods. In addition to the utilization of the novel piezoresistive fiberglass composites to monitor both strain and damage in-situ during various loading environments, the approximate location of damage within the composite was detected in all three dimensions using local changes in electrical resistance. Furthermore, this work also exploits trends in the measured resistance of fiberglass composites containing LIG for fatigue damage tracking and fatigue life prediction. In addition to being the first work to investigate LIG as a sensing element in fiberglass composites, this is notably the first time the fatigue life of such composites has been estimated prior to failure using electrical resistance measurements, yielding promising results for dynamic composite applications such as aircraft or automobiles.

Overall, this work responds to the multi-industry need for self-sensing multifunctional materials that also meet the structural demands faced by fiber-reinforced composites during dynamic loading applications. This need is satisfied by multiple materials investigated throughout the course of this work, all of which provide crucial information about the initiation and accumulation of damage throughout a variety of mechanical loading environments. The materials presented here are truly multifunctional as the sensing functions which typically require discrete or external sensors are met by the structural material itself. This dissertation also conclusively responds to questions regarding the scalability and potential for automation of multifunctional materials by using relatively simple, cost-effective, and scalable methodologies. This work thus contributes to a new generation of self-sensing structural composite materials to meet the demands of dynamic high-performing engineering structures. As a result, multiple conference presentations and publications in peer reviewed journals have resulted from this work. Specifically, the investigation of the use of ZnO nanowires for in-situ damage detection via voltage emission was published in *Advanced Functional Materials* [142], and the expansion of the voltage emission methodology using DHF PVDF for in-situ damage detection is currently under review. The primary investigation of LIG to introduce piezoresistivity for integrated sensing in aramid fiber composites is published in *Carbon* [143]. The initial analysis of the transfer printing process to integrate LIG within fiberglass-reinforced composites and the resultant in-situ sensing capabilities is published in *Composites Science and Technology* [144]. Further exploration of the use of LIG in fiberglass composites for damage localization is in print in *Smart Materials and Structures*, and additional publications investigating serpentine-patterned LIG strain gauges and fatigue life prediction of fiberglass composites within integrated LIG are currently under review.

6.3. Recommendations for Future Work

The work published in this dissertation provides a foundation for a variety of additional research in multifunctional materials. In particular, the application of ZnO nanowires for damage detection via voltage emission uses a simple technique which may possess potential to glean additional information from the host composite. For example, an in-situ analysis of the magnitude of the voltage response relative to specific forms of damage confirmed through a conclusive method such as micro-computed tomography (micro-CT) could provide well-defined ranges in the magnitude of the voltage emission in response to varying forms of damage. By measuring the voltage across the sample in-situ while simultaneously monitoring the structural behavior in all three dimensions at the micro-level, greater understanding of the effects of different damage modes on the output voltage could be achieved. Moreover, since the sensing components (electrodes and piezoelectric element) are integrated into the structure, the effects of damage to the sensing materials on the signal amplitude could also be characterized.

In addition to damage classification using multifunctional composites with ZnO, the possibility of localizing damage through voltage measurements has yet to be explored. By taking multiple simultaneous voltage measurements from the same composite while inflicting controlled, localized damage, it is expected that the measurements closest to the damage source would show the largest magnitude response, while those farther away would show a decreased response due to damping of the vibration and attrition. However, it should be noted that this experimental approach faces unique challenges since the conductive electrodes cover the entirety of the composite surfaces, and thus the same voltage emission is expected to be detectable regardless of the measurement location on the electrode. It is therefore suggested that damage be localized by using multiple discrete carbon fiber electrodes separated by electrically insulating perimeters. Local voltage measurements would thus correlate to defined areas within the composite.

Alternatively, since a large extent of composite structures operate in unpredictable dynamic environments, it would also be beneficial to utilize composites with ZnO to detect and track damage during fatigue loading. It is anticipated that by passively measuring the voltage throughout a fatigue test, sudden instances of damage would be detectable by sudden voltage emissions from the sample similar to those seen in Chapter 2, but it is also anticipated that the peak-to-peak voltage would show a change during the fatigue life. It stands to reason that the peak-to-peak voltage would show changes corresponding to changes in strain due to decreasing modulus, however the fact that damage to the composite would also inherently result in damage to the electrodes or piezoelectric sensing element would also need to be considered. Moreover, the development of a model to allow for the prediction of catastrophic failure early in the fatigue life of the composite is also suggested as an additional consideration during the described testing.

In addition to the electric potential method, which was used in Chapter 4, for damage localization in fiberglass composites with LIG, electrical impedance tomography (EIT) has gained research attention as it provides a detailed map of the electrical conductivity within the composite [145]. An investigation of fiberglass with LIG using EIT methodology would be beneficial for determining the ability of the multifunctional composites to detect barely visible damage or micro-damage in two dimensions. It would also be worthwhile in establishing a minimum size of detectable damage. Beyond fiberglass composites, damage localization using EIT methodology would also be of benefit for aramid composites which are commonly used in ballistic applications. The two dimensional localization of ballistic impact in-situ using aramid composites with integrated LIG could have direct use in defense applications such as tanks or armored vests.

Further potential also exists for a more expansive study of the response of LIG in fiberglass composites during fatigue loading. During fatigue loading of the fiberglass composites with LIG in Chapter 5, several sources of data were gathered including the sample strain measured using digital image correlation (DIC), the sample stiffness, the mean value of the electrical resistance of the sample, and the peak-to-peak value of the electrical resistance of the sample. The combined use of this large quantity of data for different combined loading patterns lends itself to machine learning for detailed fatigue damage tracking and fatigue life prediction in unknown loading environments. The work investigated here resolved the estimated fatigue life for samples exposed to a constant sine wave with a set ratio between the minimum and maximum stress and at a constant frequency, however actual composite structures in practice experience a wide range of loading environments. By exposing the samples to a wide variety of loading scenarios or training cases, a more detailed model could be built with application in actual loading environments experienced by aircraft. This use of integrated LIG to both detect damage and predict the service life of these structures in realistic scenarios would be greatly beneficial to the field of multifunctional materials.

To further confirm the potential for scaling up the described research, it is suggested that future research investigate the effects of defects within the functional materials (ZnO, DHF PVDF, and LIG) on the overall sensing abilities of the multifunctional composites. Just as structural defects within fiber-reinforced composites result in decreased mechanical properties, defects within the microstructure of the ZnO nanowires can result in decreased piezoelectric sensing potential. A detailed investigation of these changes on the overall damage sensing capabilities using the voltage emission methodology discussed in Chapter 2 would contribute to the fundamental understanding of the damage detection mechanism in addition to providing crucial information needed for the application of this multifunctional material in large-scale structures. Similarly, defects within the microstructure of the LIG investigated in Chapters 3 through 5 would affect the conductivity, and potentially the overall sensitivity of the resultant piezoresistive composites. Greater understanding of the imperfections within the LIG which occur as a result of the laser printing or transfer-printing processes would again provide information to further understand the feasibility of wide-scale application of the methods and materials used. Additionally, a cost-benefit analysis of the methods used in this research is recommended to further investigate the potential of the multifunctional materials for industrial-scale application. Although emphasis was placed on using low-cost materials and techniques which are conducive to traditional coating and roll-to-roll processing currently used in the manufacturing of composite materials, a more detailed cost breakdown based on the quantity of treated material would improve the likelihood of consideration of these methods for industrial-scale use.

REFERENCES

[1] K.K. Chawla, Composite materials: science and engineering, Springer Science & Business Media2012.

[2] R.F. Gibson, Principles of composite material mechanics, CRC press2016.

[3] R.M. Jones, Mechanics of composite materials, CRC press1998.

[4] M. Balasubramanian, Composite materials and processing, CRC press2013.

[5] R.B. Thompson, NDE simulations: critical tools in the integration of NDE and SHM, Proc.SPIE, 2009.

[6] V.M. Karbhari, 1 - Introduction: the future of non-destructive evaluation (NDE) and structural health monitoring (SHM), in: V.M. Karbhari (Ed.), Non-Destructive Evaluation (NDE) of Polymer Matrix Composites, Woodhead Publishing2013, pp. 3-11.

[7] D. Montalvao, N.M.M. Maia, A.M.R. Ribeiro, A review of vibration-based structural health monitoring with special emphasis on composite materials, Shock and vibration digest 38(4) (2006) 295-324.

[8] H. Sohn, C.R. Farrar, F.M. Hemez, D.D. Shunk, D.W. Stinemates, B.R. Nadler, J.J. Czarnecki, A review of structural health monitoring literature: 1996–2001, Los Alamos National Laboratory, USA 1 (2003).

[9] V. Giurgiutiu, A. Zagrai, J. Bao, Damage Identification in Aging Aircraft Structures with Piezoelectric Wafer Active Sensors, Journal of Intelligent Material Systems and Structures 15(9-10) (2004) 673-687.

[10] X. Zhao, H. Gao, G. Zhang, B. Ayhan, F. Yan, C. Kwan, J.L. Rose, Active health monitoring of an aircraft wing with embedded piezoelectric sensor/actuator network: I. Defect detection, localization and growth monitoring, Smart Materials and Structures 16(4) (2007) 1208-1217.

[11] J. Yang, F.-K. Chang, Detection of bolt loosening in C–C composite thermal protection panels: I. Diagnostic principle, Smart Materials and Structures 15(2) (2006) 581-590.

[12] B. Jaffe, Piezoelectric ceramics, Elsevier2012.

[13] G. Gautschi, Piezoelectric sensors, Piezoelectric Sensorics, Springer2002, pp. 73-91.

[14] A. Cuc, V. Giurgiutiu, S. Joshi, Z. Tidwell, Structural Health Monitoring with Piezoelectric Wafer Active Sensors for Space Applications, AIAA Journal 45(12) (2007) 2838-2850.

[15] A.C. Zaffir, T. Joseph, P.S. Fanping, A.R. Craig, Local-area health monitoring of aircraft via piezoelectric actuator/sensor patches, Proc.SPIE, 1995.

[16] D.L. Mascarenas, M.D. Todd, G. Park, C.R. Farrar, Development of an impedance-based wireless sensor node for structural health monitoring, Smart Materials and Structures 16(6) (2007) 2137.

[17] T.G. Overly, G. Park, K.M. Farinholt, C.R. Farrar, Development of an extremely compact impedance-based wireless sensing device, Smart Materials and Structures 17(6) (2008) 065011.

[18] F.G. Baptista, J. Vieira Filho, A new impedance measurement system for PZT-based structural health monitoring, IEEE Transactions on Instrumentation and Measurement 58(10) (2009) 3602-3608.

[19] G. Victor, M.R. James, P.R. Dennis, R. Kirk, Active sensors for health monitoring of aging aerospace structures, Proc.SPIE, 2000.

[20] M. Mitra, S. Gopalakrishnan, Guided wave based structural health monitoring: A review, Smart Materials and Structures 25(5) (2016) 053001.

[21] S. Huguet, N. Godin, R. Gaertner, L. Salmon, D. Villard, Use of acoustic emission to identify damage modes in glass fibre reinforced polyester, Composites Science and Technology 62(10) (2002) 1433-1444.

[22] M. Giordano, A. Calabro, C. Esposito, A. D'Amore, L. Nicolais, An acoustic-emission characterization of the failure modes in polymer-composite materials, Composites science and technology 58(12) (1998) 1923-1928.

[23] K. Ono, A. Gallego, Research and applications of AE on advanced composites, J. Acoust. Emiss 30 (2012) 180-229.

[24] N. Toyama, J.-H. Koo, R. Oishi, M. Enoki, T. Kishi, Two-dimensional AE source location with two sensors in thin CFRP plates, Journal of Materials science letters 20(19) (2001) 1823-1825.

[25] M.D. Seale, B.T. Smith, W. Prosser, J.N. Zalameda, Lamb wave assessment of fiber volume fraction in composites, The Journal of the Acoustical Society of America 104(3) (1998) 1399-1403.

[26] M. Surgeon, M. Wevers, Modal analysis of acoustic emission signals from CFRP laminates, Ndt & e International 32(6) (1999) 311-322.

[27] S.-E. Mechraoui, A. Laksimi, S. Benmedakhene, Reliability of damage mechanism localisation by acoustic emission on glass/epoxy composite material plate, Composite Structures 94(5) (2012) 1483-1494.

[28] J. Frieden, J. Cugnoni, J. Botsis, T. Gmür, Low energy impact damage monitoring of composites using dynamic strain signals from FBG sensors–Part I: Impact detection and localization, Composite structures 94(2) (2012) 438-445.

[29] H. Bar, M. Bhat, C. Murthy, Parametric analysis of acoustic emission signals for evaluating damage in composites using a PVDF film sensor, Journal of Nondestructive Evaluation 24(4) (2005) 121-134.

[30] I.M. De Rosa, F. Sarasini, Use of PVDF as acoustic emission sensor for in situ monitoring of mechanical behaviour of glass/epoxy laminates, Polymer Testing 29(6) (2010) 749-758.

[31] M. Barbezat, A.J. Brunner, P. Flüeler, C. Huber, X. Kornmann, Acoustic emission sensor properties of active fibre composite elements compared with commercial acoustic emission sensors, Sensors and Actuators A: Physical 114(1) (2004) 13-20.

[32] A.J. Brunner, M. Barbezat, P. Flueler, C. Huber, Composites from piezoelectric fibers as sensors and emitters for acoustic applications, Journal of Acoustic Emission 22 (2004) 127-137.

[33] I. Read, P. Foote, S. Murray, Optical fibre acoustic emission sensor for damage detection in carbon fibre composite structures, Measurement Science and Technology 13(1) (2001) N5-N9.

[34] C. Caneva, I. De Rosa, F. Sarasini, Damage mechanisms in loaded aramid composites by means of embedded PVDF acoustic emission sensors, Advanced Materials Research, Trans Tech Publ, 2006, pp. 337-342.

[35] C. Caneva, I. De Rosa, F. Sarasini, Monitoring of Impacted Aramid - Reinforced Composites by Embedded PVDF Acoustic Emission Sensors, Strain 44(4) (2008) 308-316.

[36] H.-Y. Tang, C. Winkelmann, W. Lestari, V. La Saponara, Composite structural health monitoring through use of embedded PZT sensors, Journal of Intelligent Material Systems and Structures 22(8) (2011) 739-755.

[37] X.P. Qing, S.J. Beard, A. Kumar, T.K. Ooi, F.-K. Chang, Built-in sensor network for structural health monitoring of composite structure, Journal of Intelligent Material Systems and Structures 18(1) (2007) 39-49.

[38] M. Melnykowycz, X. Kornmann, C. Huber, M. Barbezat, A. Brunner, Performance of integrated active fiber composites in fiber reinforced epoxy laminates, Smart materials and structures 15(1) (2006) 204.

[39] G. Zhou, L. Sim, Damage detection and assessment in fibre-reinforced composite structures with embedded fibre optic sensors-review, Smart Materials and Structures 11(6) (2002) 925.

[40] C. Doyle, A. Martin, T. Liu, M. Wu, S. Hayes, P. Crosby, G. Powell, D. Brooks, G. Fernando, In-situ process and condition monitoring of advanced fibre-reinforced composite materials using optical fibre sensors, Smart materials and structures 7(2) (1998) 145.

[41] T. Liu, M. Wu, Y. Rao, D.A. Jackson, G.F. Fernando, A multiplexed optical fibre-based extrinsic Fabry-Perot sensor system for in-situ strain monitoring in composites, Smart materials and structures 7(4) (1998) 550.

[42] Kuang, K. , W. Cantwell Use of conventional optical fibers and fiber Bragg gratings for damage detection in advanced composite structures: A review, Applied Mechanics Reviews 56(5) (2003) 493-513.

[43] I.M. Perez, H. Cui, E. Udd, Acoustic emission detection using fiber Bragg gratings, Smart Structures and Materials 2001: Sensory Phenomena and Measurement Instrumentation for Smart Structures and Materials, International Society for Optics and Photonics, 2001, pp. 209-215.

[44] H. Tsuda, E. Sato, T. Nakajima, H. Nakamura, T. Arakawa, H. Shiono, M. Minato, H. Kurabayashi, A. Sato, Acoustic emission measurement using a strain-insensitive fiber Bragg grating sensor under varying load conditions, Optics letters 34(19) (2009) 2942-2944.

[45] Q. Wu, F. Yu, Y. Okabe, S. Kobayashi, Application of a novel optical fiber sensor to detection of acoustic emissions by various damages in CFRP laminates, Smart Materials and Structures 24(1) (2014) 015011.

[46] R. Hadzic, S. John, I. Herszberg, Structural integrity analysis of embedded optical fibres in composite structures, Composite Structures 47(1) (1999) 759-765.

[47] K. Shivakumar, L. Emmanwori, Mechanics of failure of composite laminates with an embedded fiber optic sensor, Journal of composite materials 38(8) (2004) 669-680.

[48] C. Baron, K. Schulte, Electric resistance measurement for in situ determination of fiber failure in carbon fiber reinforced laminates, 1988.

[49] K. Schulte, C. Baron, Load and failure analyses of CFRP laminates by means of electrical resistivity measurements, Composites Science and Technology 36(1) (1989) 63-76.

[50] X. Wang, X. Fu, D.D.L. Chung, Strain sensing using carbon fiber, Journal of Materials Research 14(3) (2011) 790-802.

[51] J.C. Abry, S. Bochard, A. Chateauminois, M. Salvia, G. Giraud, In situ detection of damage in CFRP laminates by electrical resistance measurements, Composites Science and Technology 59(6) (1999) 925-935.

[52] S. Wang, D. Chung, Self-sensing of flexural strain and damage in carbon fiber polymer-matrix composite by electrical resistance measurement, Carbon 44(13) (2006) 2739-2751.

[53] S. Wang, D.D.L. Chung, J.H. Chung, Impact damage of carbon fiber polymer–matrix composites, studied by electrical resistance measurement, Composites Part A: Applied Science and Manufacturing 36(12) (2005) 1707-1715.

[54] J. Wen, Z. Xia, F. Choy, Damage detection of carbon fiber reinforced polymer composites via electrical resistance measurement, Composites Part B: Engineering 42(1) (2011) 77-86.

[55] A. Todoroki, Y. Tanaka, Y. Shimamura, Delamination monitoring of graphite/epoxy laminated composite plate of electric resistance change method, Composites Science and Technology 62(9) (2002) 1151-1160.

[56] R. Schueler, S.P. Joshi, K. Schulte, Damage detection in CFRP by electrical conductivity mapping, Composites Science and Technology 61(6) (2001) 921-930.

[57] N. Angelidis, N. Khemiri, P.E. Irving, Experimental and finite element study of the electrical potential technique for damage detection in CFRP laminates, Smart Materials and Structures 14(1) (2004) 147-154.

[58] A. Vavouliotis, A. Paipetis, V. Kostopoulos, On the fatigue life prediction of CFRP laminates using the Electrical Resistance Change method, Composites Science and Technology 71(5) (2011) 630-642.

[59] E.T. Thostenson, T.-W. Chou, Real-timein situsensing of damage evolution in advanced fiber composites using carbon nanotube networks, Nanotechnology 19(21) (2008) 215713.

[60] N.D. Alexopoulos, C. Bartholome, P. Poulin, Z. Marioli-Riga, Structural health monitoring of glass fiber reinforced composites using embedded carbon nanotube (CNT) fibers, Composites Science and Technology 70(2) (2010) 260-271.

[61] S.l. Gao, R.C. Zhuang, J. Zhang, J.W. Liu, E. Mäder, Glass fibers with carbon nanotube networks as multifunctional sensors, Advanced Functional Materials 20(12) (2010) 1885-1893.

[62] S.U. Khan, C.Y. Li, N.A. Siddiqui, J.-K. Kim, Vibration damping characteristics of carbon fiber-reinforced composites containing multi-walled carbon nanotubes, Composites Science and Technology 71(12) (2011) 1486-1494.

[63] J.-S. Jang, J. Varischetti, J. Suhr, Strain dependent energy dissipation in multi-scale carbon fiber composites containing carbon nanofibers, Carbon 50(11) (2012) 4277-4283.

[64] E. Thostenson, W. Li, D. Wang, Z. Ren, T. Chou, Carbon nanotube/carbon fiber hybrid multiscale composites, Journal of Applied physics 91(9) (2002) 6034-6037.

[65] A. Godara, L. Gorbatikh, G. Kalinka, A. Warrier, O. Rochez, L. Mezzo, F. Luizi, A.W. van Vuure, S.V. Lomov, I. Verpoest, Interfacial shear strength of a glass fiber/epoxy bonding in composites modified with carbon nanotubes, Composites Science and Technology 70(9) (2010) 1346-1352.

[66] C.S. Grimmer, C.K.H. Dharan, High-cycle fatigue of hybrid carbon nanotube/glass fiber/polymer composites, Journal of Materials Science 43(13) (2008) 4487-4492.

[67] L. Gao, T.-W. Chou, E.T. Thostenson, Z. Zhang, M. Coulaud, In situ sensing of impact damage in epoxy/glass fiber composites using percolating carbon nanotube networks, Carbon 49(10) (2011) 3382-3385.

[68] L. Gao, E.T. Thostenson, Z. Zhang, T.-W. Chou, Sensing of Damage Mechanisms in Fiber-Reinforced Composites under Cyclic Loading using Carbon Nanotubes, Advanced Functional Materials 19(1) (2009) 123-130.

[69] L. Gao, E.T. Thostenson, Z. Zhang, J.-H. Byun, T.-W. Chou, Damage monitoring in fiber-reinforced composites under fatigue loading using carbon nanotube networks, Philosophical Magazine 90(31-32) (2010) 4085-4099.

[70] G.J. Gallo, E.T. Thostenson, Spatial damage detection in electrically anisotropic fiber-reinforced composites using carbon nanotube networks, Composite Structures 141 (2016) 14-23.

[71] A. Baltopoulos, N. Polydorides, L. Pambaguian, A. Vavouliotis, V. Kostopoulos, Exploiting carbon nanotube networks for damage assessment of fiber reinforced composites, Composites Part B: Engineering 76 (2015) 149-158.

[72] H. Dai, G.J. Gallo, T. Schumacher, E.T. Thostenson, A Novel Methodology for Spatial Damage Detection and Imaging Using a Distributed Carbon Nanotube-Based Composite Sensor Combined with Electrical Impedance Tomography, Journal of Nondestructive Evaluation 35(2) (2016) 26.

[73] I. Balberg, D. Azulay, D. Toker, O. Millo, PERCOLATION AND TUNNELING IN COMPOSITE MATERIALS, International Journal of Modern Physics B 18(15) (2004) 2091-2121.

[74] F. Du, R.C. Scogna, W. Zhou, S. Brand, J.E. Fischer, K.I. Winey, Nanotube Networks in Polymer Nanocomposites: Rheology and Electrical Conductivity, Macromolecules 37(24) (2004) 9048-9055.

[75] K. Parmar, M. Mahmoodi, C. Park, S.S. Park, Effect of CNT alignment on the strain sensing capability of carbon nanotube composites, Smart Materials and Structures 22(7) (2013) 075006.

[76] M. Tehrani, A. Boroujeni, T. Hartman, T. Haugh, S. Case, M. Al-Haik, Mechanical characterization and impact damage assessment of a woven carbon fiber reinforced carbon nanotube–epoxy composite, Composites Science and Technology 75 (2013) 42-48.

[77] F. Gojny, M. Wichmann, U. Köpke, B. Fiedler, K. Schulte, Carbon nanotube-reinforced epoxy-composites: enhanced stiffness and fracture toughness at low nanotube content, Composites science and technology 64(15) (2004) 2363-2371.

[78] Q. Zhang, J. Liu, R. Sager, L. Dai, J. Baur, Hierarchical composites of carbon nanotubes on carbon fiber: influence of growth condition on fiber tensile properties, Composites Science and Technology 69(5) (2009) 594-601.

[79] Q. An, A.N. Rider, E.T. Thostenson, Electrophoretic deposition of carbon nanotubes onto carbon-fiber fabric for production of carbon/epoxy composites with improved mechanical properties, Carbon 50(11) (2012) 4130-4143.

[80] E. Bekyarova, E. Thostenson, A. Yu, H. Kim, J. Gao, J. Tang, H. Hahn, T.-W. Chou, M. Itkis, R. Haddon, Multiscale carbon nanotube− carbon fiber reinforcement for advanced epoxy composites, Langmuir 23(7) (2007) 3970-3974.

[81] Y. Zeng, L. Ci, B.J. Carey, R. Vajtai, P.M. Ajayan, Design and Reinforcement: Vertically Aligned Carbon Nanotube-Based Sandwich Composites, ACS Nano 4(11) (2010) 6798-6804.

[82] R. Sadeghian, S. Gangireddy, B. Minaie, K.-T. Hsiao, Manufacturing carbon nanofibers toughened polyester/glass fiber composites using vacuum assisted resin transfer molding for enhancing the mode-I delamination resistance, Composites Part A: Applied Science and Manufacturing 37(10) (2006) 1787-1795.

[83] Z.L. Wang, Zinc oxide nanostructures: growth, properties and applications, Journal of physics: condensed matter 16(25) (2004) R829.

[84] U. Galan, Y. Lin, G.J. Ehlert, H.A. Sodano, Effect of ZnO nanowire morphology on the interfacial strength of nanowire coated carbon fibers, Composites Science and Technology 71(7) (2011) 946-954.

[85] M.H. Malakooti, H.-S. Hwang, H.A. Sodano, Morphology-Controlled ZnO Nanowire Arrays for Tailored Hybrid Composites with High Damping, ACS Applied Materials & Interfaces 7(1) (2015) 332-339.

[86] H.-S. Hwang, M.H. Malakooti, H.A. Sodano, Tailored interyarn friction in aramid fabrics through morphology control of surface grown ZnO nanowires, Composites Part A: Applied Science and Manufacturing 76 (2015) 326-333.

[87] A. Hazarika, B.K. Deka, D. Kim, K. Kong, Y.-B. Park, H.W. Park, Growth of aligned ZnO nanorods on woven Kevlar® fiber and its performance in woven Kevlar® fiber/polyester composites, Composites Part A: Applied Science and Manufacturing 78 (2015) 284-293.

[88] M.H. Malakooti, B.A. Patterson, H.-S. Hwang, H.A. Sodano, ZnO nanowire interfaces for high strength multifunctional composites with embedded energy harvesting, Energy & Environmental Science 9(2) (2016) 634-643.

[89] A. Khan, M. Hussain, O. Nur, M. Willander, E. Broitman, Analysis of direct and converse piezoelectric responses from zinc oxide nanowires grown on a conductive fabric, physica status solidi (a) 212(3) (2015) 579-584.

[90] T. Van den Heever, W. Perold, Comparing three different energy harvesting circuits for a ZnO nanowire based nanogenerator, Smart materials and structures 22(10) (2013) 105029.

[91] Z.L. Wang, J. Song, Piezoelectric Nanogenerators Based on Zinc Oxide Nanowire Arrays, Science 312(5771) (2006) 242.

[92] Y. Zhang, K. Yu, D. Jiang, Z. Zhu, H. Geng, L. Luo, Zinc oxide nanorod and nanowire for humidity sensor, Applied Surface Science 242(1-2) (2005) 212-217.

[93] R.K. Joshi, Q. Hu, F. Alvi, N. Joshi, A. Kumar, Au decorated zinc oxide nanowires for CO sensing, The Journal of Physical Chemistry C 113(36) (2009) 16199-16202.

[94] J. Zang, C.M. Li, X. Cui, J. Wang, X. Sun, H. Dong, C.Q. Sun, Tailoring zinc oxide nanowires for high performance amperometric glucose sensor, Electroanalysis: An International Journal Devoted to Fundamental and Practical Aspects of Electroanalysis 19(9) (2007) 1008-1014.

[95] M. Villani, D. Delmonte, M. Culiolo, D. Calestani, N. Coppedè, M. Solzi, L. Marchini, R. Bercella, A. Zappettini, Turning carbon fiber into a stress-sensitive composite material, Journal of Materials Chemistry A 4(27) (2016) 10486-10492.

[96] P. Ueberschlag, PVDF piezoelectric polymer, Sensor review (2001).

[97] W.-Y. Chang, C.-H. Chu, Y.-C. Lin, A flexible piezoelectric sensor for microfluidic applications using polyvinylidene fluoride, IEEE Sensors Journal 8(5) (2008) 495-500.

[98] J.-H. Bae, S.-H. Chang, Characterization of an electroactive polymer (PVDF-TrFE) film-type sensor for health monitoring of composite structures, Composite Structures 131 (2015) 1090-1098.

[99] H. Tzou, M. Gadre, Theoretical analysis of a multi-layered thin shell coupled with piezoelectric shell actuators for distributed vibration controls, Journal of Sound and Vibration 132(3) (1989) 433-450.

[100] Y. Fu, E.C. Harvey, M.K. Ghantasala, G.M. Spinks, Design, fabrication and testing of piezoelectric polymer PVDF microactuators, Smart materials and structures 15(1) (2005) S141.

[101] R. Hasegawa, Y. Takahashi, Y. Chatani, H. Tadokoro, Crystal structures of three crystalline forms of poly (vinylidene fluoride), Polymer Journal 3(5) (1972) 600-610.

[102] E. Fukada, T. Furukawa, Piezoelectricity and ferroelectricity in polyvinylidene fluoride, Ultrasonics 19(1) (1981) 31-39.

[103] M.G. Broadhurst, G.T. Davis, J.E. McKinney, R.E. Collins, Piezoelectricity and pyroelectricity in polyvinylidene fluoride—A model, Journal of Applied Physics 49(10) (1978) 4992-4997.

[104] R. Gregorio, E. Ueno, Effect of crystalline phase, orientation and temperature on the dielectric properties of poly (vinylidene fluoride)(PVDF), Journal of materials science 34(18) (1999) 4489-4500.

[105] K. Matsushige, K. Nagata, S. Imada, T. Takemura, The II-I crystal transformation of poly(vinylidene fluoride) under tensile and compressional stresses, Polymer 21(12) (1980) 1391-1397.

[106] C.-h. Du, B.-K. Zhu, Y.-Y. Xu, Effects of stretching on crystalline phase structure and morphology of hard elastic PVDF fibers, Journal of Applied Polymer Science 104(4) (2007) 2254-2259.

[107] V. Sencadas, R. Gregorio Jr, S. Lanceros-Méndez, α to β phase transformation and microestructural changes of PVDF films induced by uniaxial stretch, Journal of Macromolecular Science® 48(3) (2009) 514-525.

[108] L.L. Blyler, G.E. Johnson, N.M. Hylton, Characterization of biaxially-oriented polyvinylidene fluoride-film for transducer applications, Ferroelectrics 28(1) (1980) 303-306.

[109] G.E. Johnson, L.L. Blyler, G.R. Crane, C. Gieniewski, Thermal piezoelectric stability of poled uniaxially-and biaxially-oriented poly(vinylidene fluoride, Ferroelectrics 32(1) (1981) 43-47.

[110] J. Lin, M.H. Malakooti, H.A. Sodano, Thermally Stable PVDF for High-Performance Printable Piezoelectric Devices, ACS Applied Materials & Interfaces (2020).

[111] J. Lin, Z. Peng, Y. Liu, F. Ruiz-Zepeda, R. Ye, E.L. Samuel, M.J. Yacaman, B.I. Yakobson, J.M. Tour, Laser-induced porous graphene films from commercial polymers, Nature communications 5 (2014) 5714.

[112] L.-Q. Tao, H. Tian, Y. Liu, Z.-Y. Ju, Y. Pang, Y.-Q. Chen, D.-Y. Wang, X.-G. Tian, J.-C. Yan, N.-Q. Deng, An intelligent artificial throat with sound-sensing ability based on laser induced graphene, Nature communications 8 (2017) 14579.

[113] D.X. Luong, K. Yang, J. Yoon, S.P. Singh, T. Wang, C.J. Arnusch, J.M. Tour, Laser-Induced Graphene Composites as Multifunctional Surfaces, ACS Nano 13(2) (2019) 2579-2586.

[114] Y. Wang, Y. Wang, P. Zhang, F. Liu, S. Luo, Laser-Induced Freestanding Graphene Papers: A New Route of Scalable Fabrication with Tunable Morphologies and Properties for Multifunctional Devices and Structures, Small 14(36) (2018) 1802350.

[115] S. Luo, P.T. Hoang, T. Liu, Direct laser writing for creating porous graphitic structures and their use for flexible and highly sensitive sensor and sensor arrays, Carbon 96 (2016) 522-531.

[116] R. Rahimi, M. Ochoa, W. Yu, B. Ziaie, Highly stretchable and sensitive unidirectional strain sensor via laser carbonization, ACS applied materials & interfaces 7(8) (2015) 4463-4470.

[117] A. Chhetry, M. Sharifuzzaman, H. Yoon, S. Sharma, X. Xuan, J.Y. Park, MoS2-Decorated Laser-Induced Graphene for a Highly Sensitive, Hysteresis-free, and Reliable Piezoresistive Strain Sensor, ACS Applied Materials & Interfaces 11(25) (2019) 22531-22542.

[118] Y. Chyan, R. Ye, Y. Li, S.P. Singh, C.J. Arnusch, J.M. Tour, Laser-induced graphene by multiple lasing: toward electronics on cloth, paper, and food, ACS nano 12(3) (2018) 2176-2183.

[119] J. Nasser, L. Groo, L. Zhang, H. Sodano, Laser induced graphene fibers for multifunctional aramid fiber reinforced composite, Carbon 158 (2020) 146-156.

[120] G.J. Ehlert, H.A. Sodano, Zinc oxide nanowire interphase for enhanced interfacial strength in lightweight polymer fiber composites, ACS applied materials & interfaces 1(8) (2009) 1827-1833.

[121] E.M. Wong, J.E. Bonevich, P.C. Searson, Growth kinetics of nanocrystalline ZnO particles from colloidal suspensions, The Journal of Physical Chemistry B 102(40) (1998) 7770-7775.

[122] L.J. Brillson, Y. Lu, ZnO Schottky barriers and Ohmic contacts, Journal of Applied Physics 109(12) (2011) 8.

[123] X. Cai, T. Lei, D. Sun, L. Lin, A critical analysis of the α, β and γ phases in poly (vinylidene fluoride) using FTIR, RSC Advances 7(25) (2017) 15382-15389.

[124] B. BabuKiran, D.G. Harish, Influence of thickness on shear properties of laminated composites, International Journal of Research in Aeronautical and Mechanical Engineering (2014) 54-60.

[125] W. Cui, M.R. Wisnom, M. Jones, Effect of specimen size on interlaminar shear strength of unidirectional carbon fibre-epoxy, Composites Engineering 4(3) (1994) 299-307.

[126] T. Krause, S. Preihs, J. Ostermann, Acoustic emission damage detection for wind turbine rotor blades using airborne sound, Proceedings of 10th International Workshop on Structural Health Monitoring (IWSHM), 2015.

[127] N. Chandarana, D.M. Sanchez, C. Soutis, M. Gresil, Early damage detection in composites during fabrication and mechanical testing, Materials 10(7) (2017) 685.

[128] M. Assarar, D. Scida, W. Zouari, E.H. Saidane, R. Ayad, Acoustic emission characterization of damage in short hemp ‐ fiber ‐ reinforced polypropylene composites, Polymer composites 37(4) (2016) 1101-1112.

[129] G. Zhu, R. Yang, S. Wang, Z.L. Wang, Flexible high-output nanogenerator based on lateral ZnO nanowire array, Nano letters 10(8) (2010) 3151-3155.

[130] Y. Qiu, H. Zhang, L. Hu, D. Yang, L. Wang, B. Wang, J. Ji, G. Liu, X. Liu, J. Lin, Flexible piezoelectric nanogenerators based on ZnO nanorods grown on common paper substrates, Nanoscale 4(20) (2012) 6568-6573.

[131] R. Beams, L.G. Cançado, L. Novotny, Raman characterization of defects and dopants in graphene, Journal of Physics: Condensed Matter 27(8) (2015) 083002.

[132] R. Chandra, S.P. Singh, K. Gupta, Damping studies in fiber-reinforced composites – a review, Composite Structures 46(1) (1999) 41-51.

[133] X. Zhou, E. Shin, K.W. Wang, C.E. Bakis, Interfacial damping characteristics of carbon nanotube-based composites, Composites Science and Technology 64(15) (2004) 2425-2437.

[134] L. Gao, E.T. Thostenson, Z. Zhang, T.-W. Chou, Coupled carbon nanotube network and acoustic emission monitoring for sensing of damage development in composites, Carbon 47(5) (2009) 1381-1388.

[135] J. Sebastian, N. Schehl, M. Bouchard, M. Boehle, L. Li, A. Lagounov, K. Lafdi, Health monitoring of structural composites with embedded carbon nanotube coated glass fiber sensors, Carbon 66 (2014) 191-200.

[136] G.J. Gallo, E.T. Thostenson, Electrical characterization and modeling of carbon nanotube and carbon fiber self-sensing composites for enhanced sensing of microcracks, Materials Today Communications 3 (2015) 17-26.

[137] S. Nonn, M. Schagerl, Y. Zhao, S. Gschossmann, C. Kralovec, Application of electrical impedance tomography to an anisotropic carbon fiber-reinforced polymer composite laminate for damage localization, Composites Science and Technology 160 (2018) 231-236.

[138] K.L. Reifsnider, Fatigue of composite materials, Elsevier2012.

[139] A.V. Movahedi-Rad, T. Keller, A.P. Vassilopoulos, Fatigue damage in angle-ply GFRP laminates under tension-tension fatigue, International Journal of Fatigue 109 (2018) 60-69.

[140] R. Talreja, Multi-scale modeling in damage mechanics of composite materials, Journal of materials science 41(20) (2006) 6800-6812.

[141] L. Böger, M.H. Wichmann, L.O. Meyer, K. Schulte, Load and health monitoring in glass fibre reinforced composites with an electrically conductive nanocomposite epoxy matrix, Composites Science and Technology 68(7-8) (2008) 1886-1894.

[142] L. Groo, D.J. Inman, H.A. Sodano, In Situ Damage Detection for Fiber‐Reinforced Composites Using Integrated Zinc Oxide Nanowires, Advanced Functional Materials 28(35) (2018) 1802846.

[143] L. Groo, J. Nasser, D. Inman, H. Sodano, Laser induced graphene for in situ damage sensing in aramid fiber reinforced composites, Composites Science and Technology 201 (2021) 108541.

[144] L. Groo, J. Nasser, L. Zhang, K. Steinke, D. Inman, H. Sodano, Laser induced graphene in fiberglass-reinforced composites for strain and damage sensing, Composites Science and Technology (2020) 108367.

[145] D. Holder, Introduction to biomedical electrical impedance tomography Electrical Impedance Tomography Methods, History and Applications ed DS Holder, Bristol: Institute of Physics, 2005.